DEVELOPMENT OF MICROWAVE/MILLIMETER-WAVE ANTENNAS AND PASSIVE COMPONENTS ON MULTILAYER LIQUID CRYSTAL POLYMER (LCP) TECHNOLOGY

A Thesis
Presented to
The Academic Faculty

by

Ramanan Bairavasubramanian

In Partial Fulfillment
of the Requirements for the Degree
Doctor of Philosophy in the
School of Electrical and Computer Engineering

Georgia Institute of Technology
May 2007

DEVELOPMENT OF MICROWAVE/MILLIMETER-WAVE ANTENNAS AND PASSIVE COMPONENTS ON MULTILAYER LIQUID CRYSTAL POLYMER (LCP) TECHNOLOGY

Approved by:

Dr. John Papapolymerou, Advisor
School of Electrical and Computer Engineering
Georgia Institute of Technology

Dr. John Cressler
School of Electrical and Computer Engineering
Georgia Institute of Technology

Dr. Andrew Peterson
School of Electrical and Computer Engineering
Georgia Institute of Technology

Dr. Bernard Kippelen
School of Electrical and Computer Engineering
Georgia Institute of Technology

Dr. George Papaioannou
School of Sciences
University of Athens (Greece)

Date Approved: 30 March 2007

To my parents

ACKNOWLEDGEMENTS

This research would not have been possible without the guidance, help, support, and friendship of many people at different stages, to whom I owe a huge debt of gratitude. I express my sincerest thanks to:

- My parents, *Bairavasubramanian* and *Meenakshi*, and my sister, *Lavanya*, for their unending love, support, patience, and encouragement
- My uncle and aunt, *Viswanathan* and *Vasanthi*, for their love and for helping me to shape my career
- My adviser, *Prof. Papapolymerou*, for his guidance on various research problems, for garnering financial support, and for constantly encouraging to strive for the best
- *Prof. Cressler*, *Prof. Peterson*, *Prof. Kippelen*, and *Prof. Papaioannou*, for serving on my defense committee, and for their evaluations and suggestions that helped improve this work
- *Dr. Ponchak*, for his help with antenna measurements
- *Prof. Tentzeris*, *Prof. Laskar*, *Dr. Pinel* and their research groups for their collaboration on certain sections of this research
- Friends and colleagues for their help, support, fellowship, and for the many stress-relieving hours of pointless discussions
- The staff of ECE, GEDC, and MiRC cleanroom, for their administrative and operational assistance

TABLE OF CONTENTS

LIST OF TABLES

LIST OF FIGURES

LIST OF SYMBOLS AND ABBREVIATIONS

$\sim$	approximately equal to
$>$	greater than
$<$	less than
$\mathring{A}$	angstrom = 10^{-10} meter
AUT	antenna-under-test
C	centigrade
CB-CPW	conductor backed coplanar waveguide
CPW	coplanar waveguide
CMOS	complementary-metal-oxide-semiconductor
CTE	coefficient of thermal expansion
Cu	copper
dB	decibel
DBR	dual-behavior resonator
dpi	dots per inch
E-plane	electric plane
ϵ_r	dielectric constant
ESE	Earth Science Enterprise
$\circ$	degrees
FBW	fractional bandwidth
FET	field-effect transistor
f_o	center frequency or cut-off frequency or resonant frequency
ft	foot
GaAs	gallium-arsenide
GHz	gigahertz = 10^9 cycles per second
GPS	global positioning satellite

H-plane	magnetic plane
HTCC	high-temperature co-fired ceramic
LCP	liquid crystal polymer
LTCC	low-temperature co-fired ceramic
M	coupling matrix
M_{xy}	coupling coefficient between nodes x and y
MCM	multichip module
MEMS	micro-electro-mechanical-system
μm	microns = 10^{-6} meter
MIMO	multiple-input multiple-output
mm	millimeter = 10^{-3} meter
MMIC	monolithic microwave integrated circuit
MOM	method of moments
NASA	National Aeronautics and Space Administration
nH	nano henries = 10^{-9} henries
NRNs	non-resonant nodes
PCS	personal communication services
PECVD	plasma-enhanced chemical vapor deposition
pF	pico farads = 10^{-12} farads
ppm	parts per million
Q_e	external quality factor
Q_L	loaded quality factor
Q_u	unloaded quality factor
RIE	reactive ion etch
RF	radio-frequency
RLL	return loss level
SHS	soft-and-hard surface
Si	silicon
SiGe	silicon germanium

SiP	system-in-a-package
SIR	stepped impedance resonator
SoC	system-on-a-chip
SOLT	short, open, load, and thru
SoP	system-on-a-package
$tan\ \delta$	loss tangent
TM	transverse magnetic
TRL	through-reflect-line
TZ	transmission zero
WLAN	wireless local area network

SUMMARY

This thesis discusses the design and development of various prototype microwave and millimeter-wave components on multilayer liquid crystal polymer (LCP) technology. The fundamental objective of this work is to understand LCP's electrical performance up to millimeter-wave frequencies through the implementation of different prototype components and assess its suitability to function as a low-cost next-generation organic platform for 3-D system-on-a-package (SoP) based radio-frequency (RF) applications.

The first section of research focuses on the development of dual-polarization/dual-frequency patch antenna arrays on multilayer LCP technology. The design and fabrication methodology of the arrays using two different substrate configurations are presented. Measurements of scattering parameters and far-field radiation patterns are included together with efficiency calculations, illustrating the advantages of using LCP for antenna applications. The flexibility and mechanical stability of the multilayer substrate have been demonstrated, making the arrays suitable for space deployment in remote sensing applications. To achieve real-time polarization reconfigurability, micro-electro-mechanical-system (MEMS) swicthes have been integrated with the developed antenna arrays. The performance of these MEMS-integrated arrays are also presented.

Next, we report on the development of several prototype low-pass and band-pass filters on LCP covering a wide range of frequency bands to characterize the electrical performance of LCP in those frequency ranges. Compact, planar, and via-less low-pass filters have been designed using the image parameter method and realized using a semi-lumped approach. The design methodology is described. Full wave simulations validated with measurement results are presented. In addition, band-pass filters, designed using coupled resonator theory, have been implemented on both single and multilayer LCP technology. A wide variety of filters with different physical and functional characteristics have been developed. The developed filters can be classified based on the filter type (low-pass/band-pass), the resonators

used (single-mode/dual-mode), the response characteristics (symmetric/asymmetric), and the structure of the filter (modular/non-modular).

Finally, examples of integrated systems operating in the X-band and V-band are presented. This part of the research involves the design and development of duplexers, radiating elements, and their integration. The duplexers themselves are realized by integrating a set of band-pass filters and matching networks. The synthesis and design techniques established in the earlier chapters were utilized for this purpose. The X-band system involves open-loop resonators, wide-slot antennas, and a 3-D stack-up, with emphasis on compactness. The V-band system involves open-loop resonators, and patch antennas, implemented on a single-layer technology, with emphasis on electrical performance. Characterization of the individual components, and of the integrated system are included.

This research has resulted in a thorough understanding of LCP's electrical performance and its multilayer lamination capabilities pertaining to its functioning as a material platform for integrated microwave systems. Novel prototype filters and radiating elements that can take advantage of such multilayer capabilities have been developed.

CHAPTER I

INTRODUCTION

1.1 Trends in wireless systems

Present day wireless systems find application in a multitude of areas such as mobile communications, radio-frequency (RF) identification, local multipoint distribution systems, wireless local area networks, remote sensing, etc. Regardless of the application, such systems demand increased functionality, better performance, reduced size, and most importantly lower development cost. Furthermore, the emergence of *convergent* systems requires a one-stop integrated solution for all sensing, computing, and communicating functions. Figure 1.1a shows a conceptual example of such a device, which can function as a cell phone, monitor weather, store data, perform basic computations, connect to the internet and can be worn in our hands much like a simple watch. Figure 1.1b shows an example of a smart implant in which leading edge cell phone functionality is integrated with biomedical sensors for use in critical physiological problems.

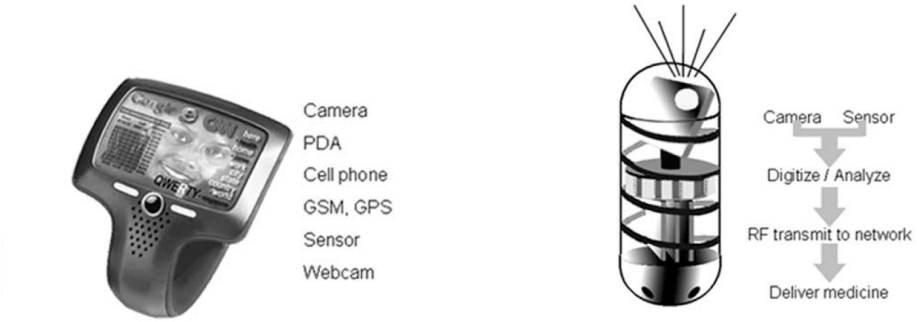

(a) Smart watch. (b) Smart implant.

Figure 1.1: Examples of *convergent* systems.

Although researchers around the world use various approaches like system-on-a-chip (SoC), multichip module (MCM), and system-in-a-package (SiP) to create convergent systems, the system-on-a-package (SoP) approach [98, 99, 65] has been identified as the best solution to assimilate multiple system functions into one compact, low-cost, high-performance

packaged system.

1.2 SoC Vs SoP approach

Researchers piloting the SoC approach envision a fully integrated system on a single wafer [68]. In this approach, anything other than the semiconductor area is dispensable and all the active and passive functions are built on-chip. This approach is attractive from a cost standpoint, because the entire system (or chip) needs to be packaged only once. In addition, the modules that use the SoC approach are invariably more compact than those that employ both *chip* and *package*. However, standard silicon-based processes such as complementary-metal-oxide-semiconductor (CMOS) process are suitable only for low frequency ($f < 10\ GHz$) applications. At high frequencies, they suffer from low quality factor passives [24] and poor RF isolation characteristics. Other SoC technologies such as gallium-arsenide (GaAs) offer low substrate loss, but are more expensive. Using large areas of GaAs for passive analog components is not cost-effective. Silicon germanium (SiGe) on either CMOS/BiCMOS grade silicon (Si) or high resistivity Si is a lower cost replacement for GaAs for some applications, but it is still a relatively lossy substrate for passive RF components.

At high frequencies ($f > 10\ GHz$), it makes sense to reduce the burden on the chip and build passive functions on a separate low-loss RF substrate (the package). The approach that advices this segregation between the chip's responsibilities and the package's responsibilities is the SoP approach.

SoP is similar to the MCM approach, but allocates a greater responsibility to the package. In a MCM-based system, the package just acts as a housing for different chips. It performs the functions of powering, cooling and interconnecting these chips. The chip(s) and the package can be designed independent of each other. In a SoP-based system, the package performs all the above mentioned functions plus it houses passive functionality that are built on and/or embedded inside the package. In contrast with the MCM approach, the package and the chip(s) have to be designed together in a SoP system. Figure 1.2 shows an example of how functionality can be divided between the chip(s) and the package for a

SoP-based RF system.

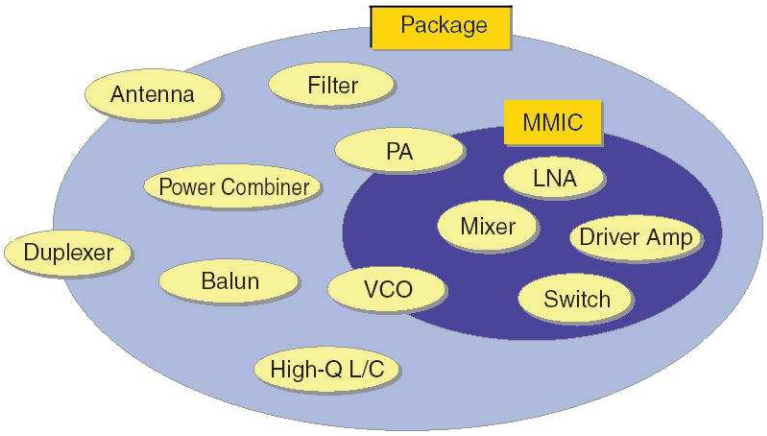

Figure 1.2: Functionality segregation in a SoP-based RF system.

SoP suggests a multilayer dielectric substrate/packaging approach to achieve the integration of diverse passive and active components without compromising cost and size. An exploded conceptual representation of a SoP-based system is shown in Figure 1.3. Figure 1.4 presents a cross section of a typical SoP-based system.

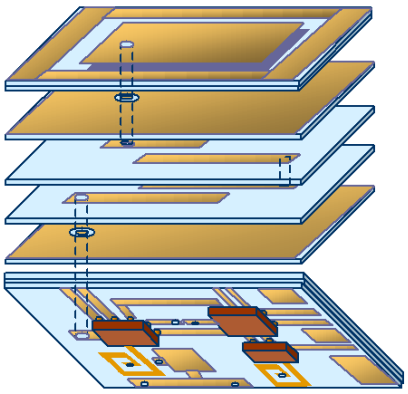

Figure 1.3: Exploded pictorial representation of a typical SoP-based system.

1.3 SoP material technologies

Central to the theme of the SoP approach is the development of smart systems, novel integrating techniques, and the identification of suitable material technology that supports such integration. For example, a viable 3-D SoP technology for wireless communication

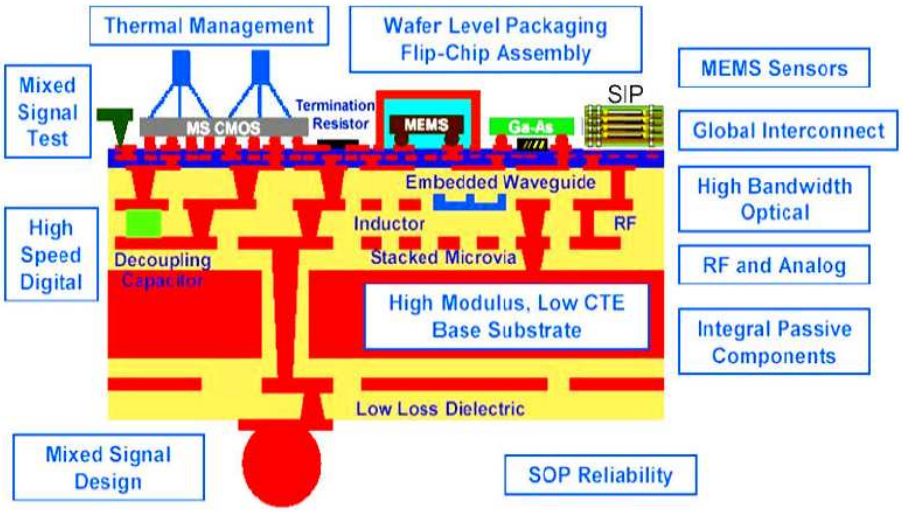

Figure 1.4: Cross section of a typical SoP-based system.

applications would require primary building blocks such as amplifiers, embedded passives, high-performance filters, baluns, integrated antennas, and a suitable platform to integrate the different functional components. The material platform should provide excellent high-frequency electrical properties, mechanical stability, chemical resistance, good barrier properties, multilayer lamination capabilities, and be cost competitive.

Microwave composites and ceramics are the popular materials that have been currently identified as suitable platforms for a SoP system. These have excellent packaging characteristics as well as good electrical properties. Microwave composites such as variations of Rogers Duroid or Taconic RF [1, 2] series materials use proprietary mixes of materials like polytetraflouroethylene (PTFE), glass weave, and ceramic fills. These materials are carefully engineered for excellent performance, but are expensive. Furthermore, because a mix of materials is used, the homogenity is lost. Alumina is another commonly used material for high frequency applications because of its zero water absorption characteristics. The major limitation of these materials (composites and alumina), as far as them functioning as a SoP platform, is that none of these are capable of producing homogenous laminated 3-D modules.

Low-temperature co-fired ceramic (LTCC) is one of the very few substrate technologies that satisfies nearly all the requirements [88, 50]. Recent breakthroughs in the LTCC

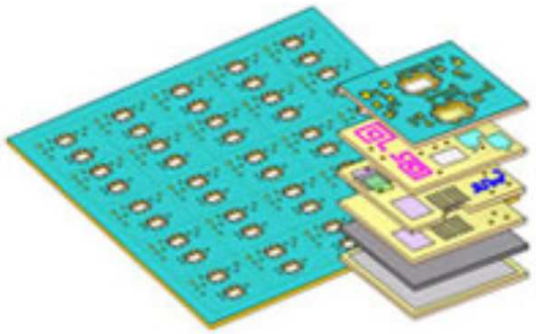

Figure 1.5: LTCC-based multilayer module.

technology have reduced or completely obliterated the "tape shrinkage" problem (in the horizontal dimensions) traditionally associated with ceramic firing. They have the unique ability to be laminated into multilayer homogeneous dielectric substrates and packages. They possess a combination of electrical, thermal, chemical, and mechanical properties that cannot be found in most other material groups. Figure 1.5 shows an example of LTCC-based multilayer module realized by firing together several patterned individual layers. Some of their characteristics beneficial to the applications of our interest are listed below:

- Stable dielectric constant over a wide range of RF/microwave/millimeter-wave frequencies
- Low dielectric loss up to millimeter-wave frequencies
- Engineerable coefficient of thermal expansion (CTE)
- Vertical integration capability with high number of layers (> 50)
- Excellent packaging characteristics - very low water and moisture absorption properties

Despite these advantages, LTCC may not be ideal for all applications. For example, printed antennas on LTCC substrates suffer from reduced efficiency because of their relatively high dielectric constant ($\epsilon_r = 5.4 - 9.1$). Besides, LTCC is not particularly suited for applications that require large amounts of horizontal real estate. The size of LTCC modules is restricted to $8'' \times 8''$ even in the state-of-the-art LTCC manufacturing foundries [58].

Furthermore, LTCC is still expensive compared to conventional laminate materials.

Another disadvantage with the LTCC process is that its process temperature ($800°C - 1000°C$) may not be acceptable for some fully integrated solutions. As an example, MEMS switches are increasingly gaining importance in the design of smart reconfigurable systems. The comparatively high processing temperature of LTCC may act as a bottleneck to incorporate MEMS-based reconfigurability into systems developed on an LTCC platform. Also, many unpackaged chips, which contain the active devices, cannot survive this high processing temperature. As a result, they have to be packaged separately, which will significantly increase the cost. The major advantage of the SoP approach compared to approaches such as SiP or MCM is that it proposes to use a single wafer-scale packaging step after mounting all the required chips onto the multilayer dielectric substrate. A high-temperature LTCC process cannot fully utilize the advanatages of the SoP philosophy.

Other drawbacks include the metallization techniques available with the LTCC process and the brittle nature of the material. To realize the full advantages of an integrated SoP system, alternative material technologies need to be explored.

1.4 Liquid crystal polymer technology

Liquid crystal polymer (LCP) has been identified as a potential candidate because of its excellent packaging characteristics [42]. Although LCP's superior substrate properties have been well known for almost a decade now [54, 32], manufacturing difficulties [57, 30] have prevented it from being considered as a serious candidate for RF applications. Recent advances in LCP processing [37, 3] have changed the scenario, though, and it has gained immense attention among RF researchers [34, 109] since then.

LCP offers a unique combination of properties that makes it a viable technology for SoP-based systems. It is quasi-hermetic and has the potential to act both as a substrate and a package. Being a polymer, it is considerably cheaper compared to ceramics and other composite materials. Its multilayer lamination capabilities make it suitable for the integration of various modules. Its stable electrical properties, low processing temperature, and low cost make it a choice material for developing smart, reconfigurable, and fully

integrated RF systems.

The numerous benefits of using LCP as an organic platform include:

- Excellent electrical properties up to millimeter-wave frequencies (stable ϵ_r and low loss [$tan\ \delta = 0.002$–0.005] for $f < 110\ GHz$) [95]
- Low cost ($\$5/ft^2$ for a 2-mil single-clad low-melt LCP) [4]
- Quasi-hermetic ($water\ absorption < 0.04\%$) [37]
- Low xy CTE, which may be engineered ($6 - 40\ ppm/°C$) to match metals or semiconductors
- Thermally stable electrical characteristics than many other substrates [94]
- Lamination capabilities to generate homogenous multilayer RF architectures
- Relatively low temperature processing ($\sim 285°$)
- Flexible for conformal and flex-circuit applications
- Naturally non-flammable
- Recyclable

1.5 Object of this thesis

The primary goal of this research is to evaluate LCP's electrical performance through the design, implementation, and measurement of passive components and antennas operating up to millimeter-wave frequencies and thereby determine the feasibility to use LCP as a platform for developing low-cost, all-in-one, SoP-based solution for RF applications.

Prior to this research, LCP's electrical properties had been studied only with the help of standard transmission lines and resonators. Although work on developing multilayer LCP architectures was initiated by Thompson [93], research on adding functionality onto LCP technology had not been carried out before. To determine the feasibility of using LCP for SoP-based RF applications, specific passive functions such as antennas, filters, and matching networks need to be realized on LCP and tested. The implementation of the said passive

components on LCP technology and their characterization are the desired contributions of this work.

1.6 Contributions and organization

The contributions of this thesis are related to the design of novel prototype passive components and their implementation on LCP technology.

Chapter 2 focuses on the design, fabrication, and characterization of dual-frequency/dual-polarization patch antenna arrays on multilayer LCP technology. Two different substrate configurations are explored. Homogenous multilayer architectures using LCP have been successfully generated with the help of optimized lamination techniques. Measurements of scattering parameters and principal plane radiation patterns are included along with efficiency measurements, outlining the advantages of using LCP for antenna applications. In addition, micro-electro-mechanical-system (MEMS) switches have been integrated with the developed antenna arrays to enable real-time polarization reconfigurability. This is the first such demonstration of advanced multilayer antenna arrays developed on an organic technology. The research performed on the development of these patch antenna arrays on LCP has led to a number of peer-reviewed conference and journal publications [36, 22, 14, 16].

In Chapter 3, the development of planar low-pass and band-pass filters, operating from C-band to V-band, on single-layer LCP technology is presented. The performance of these filters on LCP has been reported for the first time, enabling an understanding of LCP's electrical characteristics up to millimeter-wave frequencies. The low-pass filters have been designed using image parameter theory and implemented using a semi-lumped component approach. Design techniques to realize compact filters with excellent performance are presented. Scattering parameter measurements of these filters are included along with ideal lumped component simulations and 2.5-D layout simulations. Additionally, band-pass filters, designed using coupled resonator theory and implemented on LCP, have been characterized. Measurements of unloaded quality factor of the resonators employed by these filters are presented.

In Chapter 4, the development of multilayer band-pass filters on LCP technology is

presented for the first time. Two prototype filters have been realized - one using single-mode open-loop resonators and the other using dual-mode slotted patch resonators. The prototype with single-mode resonators employs a modular structure realized using non-resonant nodes (NRNs). Coupling between such NRNs in a multilayer configuration has been proposed and utilized for the first time. The multilayer prototypes provide considerable size savings compared to an uniplanar implementation.

The wide variety of filters reported in this work can be classified based on the filter type (low-pass/band-pass), the resonators used (single-mode/dual-mode), the response characteristics (symmetric/asymmetric), and the structure of the filter (modular/non-modular). The results obtained with these filter implementations have been published in [76, 17, 19]

The integration of various individual passive functions such as antennas, filters, and matching networks has also been pursued. The development of two such integrated modules for use with transceiver systems is presented in Chapter 5. Band-pass filters and matching networks are integrated to realize a duplexer, which is then integrated with a radiating element to realize the final module. A V-band module that employs a single-layer implementation has been developed for short range wireless applications [20]. An X-band module that takes advantage of the multilayer lamination capabilities of LCP has been designed, fabricated and measured. The performance of these modules confirm the potential of LCP to function as an organic platform for SoP-based wireless applications.

Chapter 6 concludes this thesis, summarizing its contributions. Included in the appendices are filter implementations that complement the projects described in the earlier chapters of this report. Appendix A details the implementation of dual-band WLAN filters on LCP technology [21]. Appendix B describes the development of asymmetric modular filters on LCP [18].

CHAPTER II

DUAL-FREQUENCY/DUAL-POLARIZATION PATCH ANTENNA ARRAYS

Many radar and communication systems require antennas equipped with dual-polarization capabilities to facilitate higher capacity. In multiple-input multiple-output (MIMO) mobile communications systems, dual-polarized antennas serve as a means of increasing the number of sub-channels [35], while in automotive radar systems, they can be used to detect potential road hazards, such as black ice [77]. Moreover, dual-frequency antennas have gained interest in wireless communication systems such as wireless local area networks (WLAN), personal communication services (PCS), and global positioning satellite (GPS) systems [80] where different frequency bands can be covered in a single design.

2.1 Objective

Our objective is to develop dual-frequency and dual-polarization antenna arrays operating at 14 and 35 GHz to be used in the National Aeronautics and Space Administration's (NASA) Earth Science Enterprise (ESE) radiometric system. These antenna arrays are required for the remote sensing of global precipitation, evaporation, and cycling of water. Water evaporation, precipitation, and water vapor feedbacks alter the surface and atmospheric heating and cooling rates. A sufficient understanding of such phenomena and processes is a key source for the accurate prediction of the planet's climate. For these reasons, water cycle research is a high-priority area of research. These processes are not adequately taken into account by currently used climate models. NASA seeks to enhance the understanding of these processes through the collection of pertinent data and the development of models that respond to the water cycle's variability.

The foremost requirement of the ESE radiometric system is the development of low-cost, low-mass, deployable antennas with large surface area that can be rolled up or folded for launch and then deployed in space. In addition, the developed antenna array should have

the same radiation pattern characteristics at both the 14 and 35 GHz frequency bands and for both the linear polarizations. Last, electronic scanning and shaping of the beams is required at the two frequencies. This will typically require integration of phase shifters and switches.

2.2 Overview of the existing technology

Parabolic reflectors, because of their high gain, were the preferred antennas for space applications. However, they are bulky, heavy, difficult to deploy, expensive, and have a limited scanning capability. Reflectarray, and inflatable reflectarray antennas were developed as an alternative and are still being actively researched, but they suffer from low antenna efficiency, difficulties in maintaining uniform membrane spacing and surface flatness, increased side-lobe levels, and single-frequency operation [81, 53]. While past efforts have resulted in deployable antenna structures, they have not been dual-frequency and dual-polarization, and past antennas that met those goals have not been deployable or have been based on high-cost and large weight/volume technology.

We propose to use microstrip patch antennas because of their low cost, low profile, light weight, and ease of fabrication [27]. In recent years, there has been much research done in the field of designing dual-frequency and dual-polarization microstrip antenna arrays [89, 85]. When designing these arrays, one has to confront many parameters of interest and the associated complexity both in design and fabrication. There is a need for a complex feeding structure that minimizes interconnect loss, feedline radiation, and cross-coupling [61]. Substrate thickness can affect cross-polarization levels as well as bandwidth and efficiency. The distance of the antenna elements in the array can affect the -3 dB beamwidth, directivity, and side-lobe levels besides impacting the overall size. Careful consideration needs to be given to avoid cross-coupling between the antenna arrays operating at different frequencies, blockage effects, and edge diffraction [48]. It is difficult to achieve all the aforementioned performance requirements with a single-layer structure. A multilayer architecture is required that can also result in very compact implementations. One such design of a dual-frequency, dual-polarized microstrip antenna array incorporating vertical

integration was proposed by Granholm and Skou [40]. This design consists of C-band and L-band patches operating at 1.25 and 5.3 GHz, respectively, on the metal layers separated by the substrate layers of three distinct dielectric media, including foam. Such a hybrid arrangement is used, presumably, to control the effective dielectric constant, as it can have a profound effect on the antenna performance.

Although there have been many reported examples of dual-frequency, dual-polarization microstrip antenna arrays on substrates, such as Duroid, these designs are not always favorable because of various undesirable substrate properties. Materials like Duroid are often used in conjunction with low dielectric constant foam to realize multilayer configurations. Such composite multilayer structures are subjected to greater stress because of CTE mismatches, which can alter the dimensions of the structure. There are many other thermal and mechanical problems inherent in such a multilayer design formed by integrating different materials. To overcome these problems, there is a need for a laminated substrate that has vertical integration capabilities and is suitable for packaging RF passive and active components and embedded devices.

Even though LTCC technology is very suitable for multilayer realization of microwave circuits such as filters and other passives, it is not ideal for antenna implementations. Antennas using high index materials such as LTCC result in pronounced surface wave excitation that can limit the impedance bandwidth, reduce the efficiency, and degrade the radiation pattern [86]. One solution is to use micro-machined or suspended patch antennas [73], albeit with increased fabrication cost and complexity. A soft-and-hard surface (SHS) structure can also be used to improve the radiation pattern [64]. Even then, these technologies are not suitable for the application of concern, because they do not support easy deployment in space.

Because the performance of microstrip antennas depends strongly on the characteristics of the substrate, the suitability of these elements for the described NASA application depends on the underlying material technology. Specifically, the material technology needs to support large area processing, multilayer implementation, and easy deployment in space. LCP, with a unique combination of characteristics and good millimeter-wave performance

as outlined in Chapter 1, offers an excellent solution to the aforementioned problems. Its flexible properties allow for the material to be rolled up, which is ideal for antenna arrays that need to be deployed in space.

The design and fabrication methodology of dual-frequency and dual-polarization antenna arrays on multilayer LCP technology, together with the scattering parameter and radiation pattern measurements, is described in subsequent sections of this chapter. Two different configurations, one in which the patch elements are fed by a direct microstrip feed [52] and the other in which the patch elements are fed through slots on the ground plane [78], are explored. Although many possibilities of substrate and feed configurations exist, these arrangements were particularly chosen to meet three major requirements of this application:

- The return loss and radiation characteristics for both polarizations need to be identical.
- The return loss and radiation characteristics for both frequencies need to be similar.
- Polarization and beam steering require the integration of antenna arrays with electronic or electromechanical switches, reconfigurable phase shifters, and attenuators.

2.3 Microstrip-fed patch antenna arrays

2.3.1 Array design

The generic multilayer architecture of the dual-polarization/dual-frequency patch antenna array with microstrip feed is shown in Figure 2.1.

The metal used in simulation and fabrication for the ground plane and the antenna elements is copper (Cu) and has a thickness of 18 μm. The total substrate thickness (h) for the design is 432 μm, consisting of two LCP layers (each 203 μm thick) and a 26 μm bonding layer. The 35 GHz antenna array is placed on the top surface of the LCP substrate (at the interface of LCP and air), while the 14 GHz antenna array that is physically larger is embedded on a 203 μm layer (h1). The two arrays were designed independently and then fine-tuned before integration to optimize the impedance matching and radiation

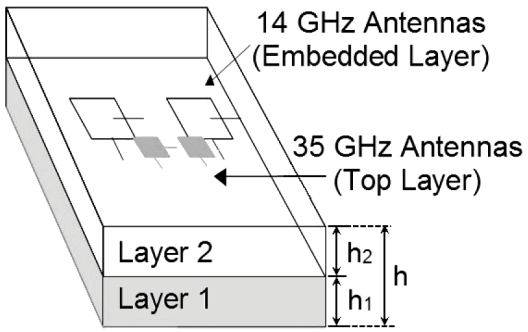

Figure 2.1: Generic multilayer architecture of the microstrip-fed antenna array.

characteristics across both bands. *EM*-Picasso [5], a method of moments (MOM)-based frequency domain 2.5-D solver, was used to design and simulate these antenna arrays. The particular choice of substrate thicknesses stemmed from extensive analysis of their influence on cross-polarization levels, bandwidth, and efficiency at each frequency. The feed network for each array is placed in the same layer as the radiating elements to minimize design and fabrication complexity and to reduce cross-talk between the arrays. This design arrangement is relatively simple, though it must be acknowledged that there will be some unwanted coupling between the feed network and the patch elements that cannot be totally avoided.

The top view of the designed dual-frequency antenna array with diagonal patch elements is shown in Figure 2.2. The patches are rotated by 45° and the polarization directions are at 45° and 135° as opposed to the traditional x-y directions. This arrangement helps in realizing a symmetrical feed network for both polarizations. Currents are always fed in phase to all antenna elements in both polarization directions. This is essential in order to have the main beam pointing as close as possible in the bore-sight direction. The impedance characteristics, such as the -10 dB bandwidth and the radiation pattern characteristics, such as the directivity, the half-power beam-width, the cross-polarization level, and the side-lobe level, are very similar for both polarizations. This is one of the critical requirements of the antenna arrays used in satellite imaging systems. The feeding structure for each array contains 200 μm gaps (see inset in Figure 2.2) to enable excitation of the dominant TM mode

(TM_{10}) corresponding to one linear polarization and to prevent excitation of the other mode (TM_{01}), which corresponds to the orthogonal linear polarization. In this case, the switching of polarizations is controlled by the presence of "hard-wired" perfect "short" (simulated by a continuous feedline) and "open" (simulated by a 200 μm gap) conditions. In a practical implementation, RF MEMS switches are used to switch polarizations and steer the main beam. To minimize the radiation effects of the feed lines, the lines that directly connect to the radiating element are made as narrow as allowed by our fabrication capabilities. The position of the gaps was carefully chosen to minimize the cross-polarization levels. Specifically, the length of the feed network between the patch edges and the gap position was made an integer multiple of $\lambda_g/2$ to transfer perfect open conditions to the edge of the patch, where 'λ_g' is the guided wavelength. The dimensions of the patch were first optimized to make it resonant at the desired frequency. A recessed patch feed and a combination of T-junctions and quarter-wave transformers were then employed to achieve better matching and a symmetric feed structure is used to expand into a 2×1 array.

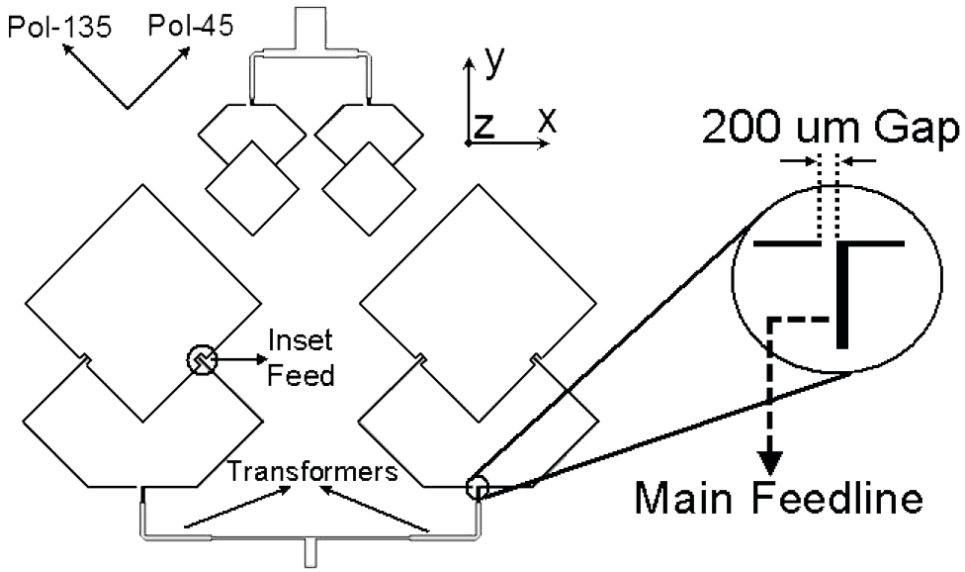

Figure 2.2: Top view (with all layers interlaced) of the microstrip-fed antenna array. The inset shows an enlarged portion of the feedline containing the 200 μm gap (on the left side branch of the main feedline). By moving the gap to the right ride branch, the polarization can be switched. The configuration shown here will result in radiation patterns with E-field polarized along the 135^0 axis.

2.3.2 LCP multilayer fabrication

The antenna arrays were fabricated with two copper-clad 203 μm LCP dielectric sheets and one 26 μm LCP adhesion layer from Rogers Corporation. Although a thick copper layer may restrict the minimum feature size because of undercut problems, it is difficult to sputter/electroplate thin layers of copper on LCP reliably because LCP has a low stiction coefficient to copper. Therefore, a thick copper cladding was used. The etch process was characterized and the patterns were modified beforehand to compensate for the undercut. The undercut, if not compensated, can cause undesirable shifts in the resonant frequency of the array, especially at 35 GHz. An alternative to using a thick copper layer would be to introduce a thin seed layer such as titanium between the copper layer and LCP to improve stiction. Although this was not tried, a thin seed layer (0.3 μm) will have no effect on the array performance because the copper layer (3 μm) will be much thicker in comparison. Such layers are often used in semiconductor circuits with no effect on performance. Shipley 1827 photoresist was used for pattern definition and the arrays were exposed under 16,000 dpi mask transparencies pressed into sample contact with 5" glass mask plates. Photoresist development and a wet chemical etch with ferric chloride were then performed to complete the antenna patterning.

The LCP layers with the 14 GHz and the 35 GHz arrays were then bonded together in a Karl-Suss SB-6 silicon wafer bonder using a 26 μm low-melt LCP bond layer sandwiched between the two 203 μm high-melt LCP core layers. The bond layer melts at a lower temperature than the core layers and its flow, coupled with the tool pressure applied between the core layers, results in the realization of multilayer LCP structures. The idea of using the wafer bonder for fabricating multilayer LCP substrates was proposed by Dane Thompson [93], another research member in the group. This author's contribution was to optimize the bonding process as relevant to the creation of specific antenna architectures. This is the most critical step in the fabrication process and has to be understood thoroughly to create multilayer LCP structures reliably. Several experiments were carried out to optimize the temperature, the tool pressure, and the process times to achieve good bonding while preventing shrinkage, formation of bubbles, and melting of core layers. The bubbles can

result in air gaps that can affect the array performance at millimeter-wave frequencies. A typical LCP bonding process is illustrated in Figure 2.3. Figure 2.4 shows a photo of the Karl-Suss wafer bonder that was used for creating LCP multilayer architectures reported in this work.

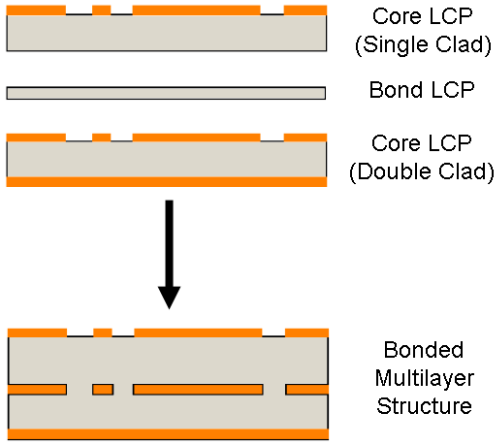

Figure 2.3: Illustration of a typical LCP bonding process.

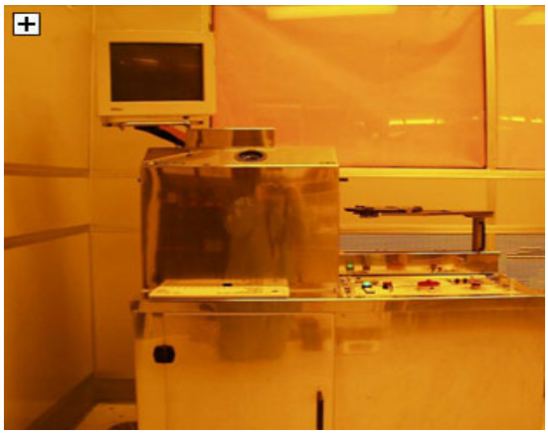

Figure 2.4: Photo of the Karl-Suss wafer bonder.

For the multilayer antenna array structure, accurate alignment between different layers is necessary. This is facilitated by drilling precision alignment holes using a laser system. Three different laser systems, the CO_2 laser, the excimer laser, and the infra-red laser, were used depending on the desired alignment accuracy levels. These holes were drilled before the individual layers were patterned. The alignment marks in the masks, which contain the patterns, were aligned to the laser holes drilled on the substrates during photolithography.

After the individual substrates were patterned, alignment was maintained during bonding using alignment pins in the bonding press plates. This specific alignment procedure is unique and essential in creating multilayer antenna structures operating at millimeter-wave frequencies that require very precise alignment and was developed in conjunction with Dane Thompson. Photographs of 2×1 antenna arrays fabricated on LCP showing the flexibility of the substrate are shown in Figure 2.5.

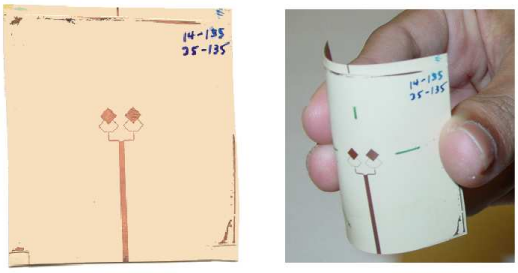

Figure 2.5: Left: Photo of fabricated 2x1 microstrip-fed array. The 14 GHz array is not visible, as it is embedded. Right: Photo demonstrating flexibility.

2.3.3 Measurements

Return loss measurements were carried out by mounting the array on an aluminum fixture that included a 2.4 mm coaxial-to-microstrip connector. A short, open, load, thru (SOLT) calibration was performed on a vector network analyzer with the reference planes at the end of the coaxial cables. When required, the microstrip launcher was adjusted to improve the impedance matching between the antenna under test (AUT) and the coaxial launcher. The antenna pattern measurements were carried out by Dr. George Ponchak at the NASA Glenn Research Center. An anechoic chamber with the AUT as the receive element and a 15 dB gain horn antenna as the transmitting antenna were used for radiation pattern measurements. The AUT was rotated through the measurement plane, and the entire system, including the data recording, was automated. Because the microstrip launcher and the absorbing material placed around it covered a portion of the plane during the scan, there was a slight asymmetry in the radiation patterns. In addition, the absorber affected the radiation pattern at scan angles greater than 70° off boresight.

The simulated and measured return loss plots versus frequency are shown in Figures 2.6

(14 GHz) and 2.7 (35 GHz). The results shown are for the 135° polarization, though they are the same for the 45° polarization also because of the symmetric arrangement. The dual-frequency array was excited at one frequency, while the other array was treated as a parasitic element. The results are summarized in Tables 2.1 and 2.2. The shift in the resonant frequency can be attributed to fabrication tolerances. The discrepancy in return loss at 14 GHz is due to the extension of the feedline of the embedded (14 GHz) antenna to a point where the top laminated layer of the substrate no longer covers the feedline, thus modifying its characteristic impedance. The measured impedance bandwidths at both frequencies are in good agreement with those of the simulated designs.

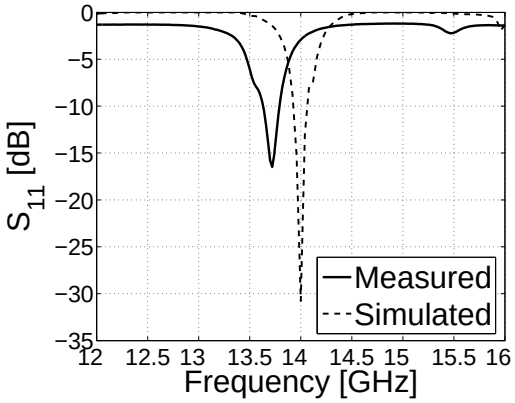

Figure 2.6: Return loss - 14 GHz microstrip-fed array.

Table 2.1: Return loss characteristics of the 14 GHz microstrip-fed array.

Characteristic	**Simulated**	**Measured**
Resonant Frequency	14 GHz	**13.72 GHz**
Return Loss	-30.7 dB	**-16.5 dB**
-10 dB Return Loss Bandwidth	140 MHz	**160 MHz**
Percent Bandwidth	1.00%	**1.17%**

Additionally, the simulated and measured 2-D radiation patterns are shown in Figures 2.8a and 2.8b for the E- and H-plane at 14 GHz, respectively, and Figures 2.9a and 2.9b for the E- and H-plane at 35 GHz, respectively. The results are summarized in Tables 2.3 and 2.4.

The E-plane and H-plane beamwidths and the shapes of the co-polarized patterns are

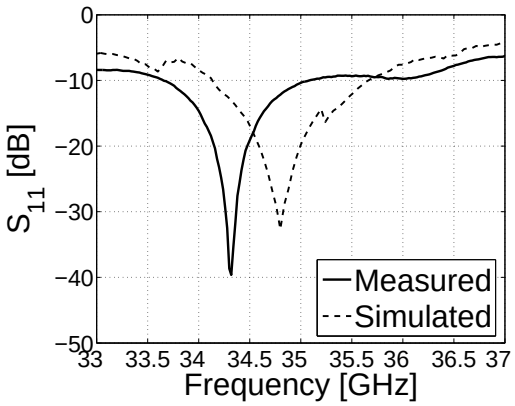

Figure 2.7: Return loss - 35 GHz microstrip-fed array.

Table 2.2: Return loss characteristics of the 35 GHz microstrip-fed array.

Characteristic	**Simulated**	**Measured**
Resonant Frequency	34.87 GHz	**34.32 GHz**
Return Loss	-32.5 dB	**-39.6 dB**
-10 dB Return Loss Bandwidth	1560 MHz	**1530 MHz**
Percent Bandwidth	4.47%	**4.46%**

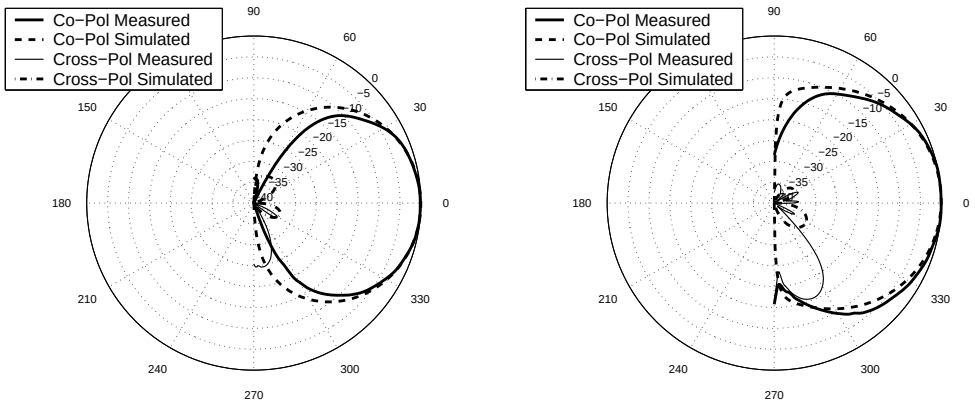

(a) E-plane patterns.

(b) H-plane patterns.

Figure 2.8: 2-D radiation patterns - 14 GHz microstrip-fed array.

consistent for both the simulated and measured patterns of the arrays. The center-to-center distance of the radiating elements can be increased to reduce the E-plane beamwidth to a value close to the H-plane beamwidth, but side-lobes will start to form as a result of this increase. The measured cross-polarization levels also agree well with the predicted values for scan angles less than 70°. The discrepancy at angles above 70° is due to the presence

Table 2.3: Radiation pattern characteristics of the 14 GHz microstrip-fed array.

Characteristic	Simulated	Measured
E-Plane -3 dB Beamwidth	65°	**67°**
H-Plane -3 dB Beamwidth	58°	**58°**
Max. Cross-pol.(E-plane)	-31 dB	**-25 dB**
Max. Cross-pol.(H-plane)	-33 dB	**-30 dB**

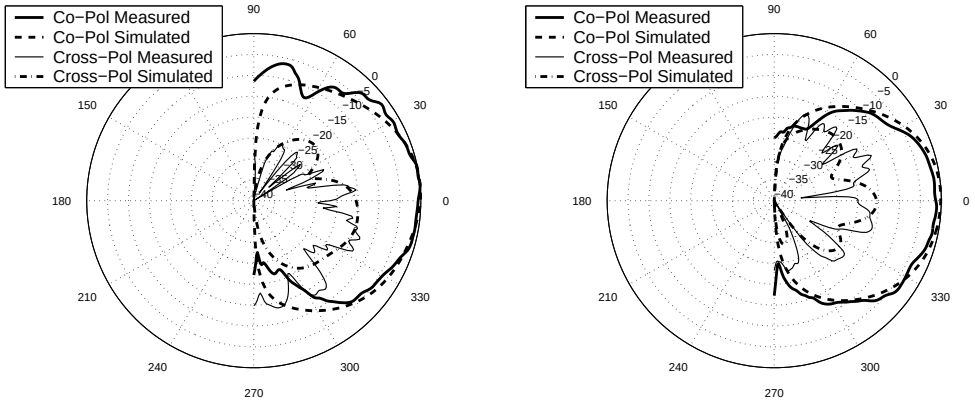

(a) E-plane patterns.

(b) H-plane patterns.

Figure 2.9: 2-D radiation patterns - 35 GHz microstrip-fed array.

Table 2.4: Radiation pattern characteristics of the 35 GHz microstrip-fed array.

Characteristic	Simulated	Measured
E-Plane -3 dB Beamwidth	65°	**66°**
H-Plane -3 dB Beamwidth	59°	**59°**
Max. Cross-pol.(E-plane)	-15 dB	**-14 dB**
Max. Cross-pol.(H-plane)	-16 dB	**-15 dB**

of the absorber, as explained earlier. In addition, it has been noted in [39] that the cross-polarization level tends to increase as the substrate thickness increases. Therefore, the higher-frequency (35 GHz) antenna array on the electrically thicker substrate exhibits a worse cross-polarization level than the lower-frequency (14 GHz) array on the electrically thinner substrate. To demonstrate the flexibility and mechanical stability of the multilayer LCP substrate, which is one of the key requirements for deployable antennas, antenna arrays were flexed several times and recharacterized. The return loss and radiation patterns were unchanged within the repeatability of the measurement equipment.

This was the first demonstration of an antenna array operating at millimeter-wave frequency and implemented on a multilayer organic technology. The measured results for the 2×1 antenna arrays were quite satisfactory. The cross-polarization level at 35 GHz was the only concern, although the measured results were still comparable to the simulated ones. Admittedly, the design arrangement chosen was relatively simple, but it enabled us to demonstrate the applicability of LCP for the development of light-weight and conformal antenna arrays. Once these basic credentials were established, a more complicated architecture was developed to address the shortcomings of the current structure. Specifically, when we tried to expand the 2×1 array to a 2×2 array that could form a basis for a more general planar array, the cross-coupling between the feed network and the patch elements within an array increased significantly and created disturbances in the radiation pattern. In addition, parasitic resonances were identified and it was quite impossible to minimize cross-talk between the feed network of one array and the patch elements of the other array. Several design arrangements were tried, but at least a couple of performance characteristics needed to be sacrificed when the simple microstrip-fed structure is kept unchanged. To overcome these issues, a new layer was introduced that incorporated just the feed networks for both the 14 and 35 GHz arrays. The development of this aperture-coupled array architecture is described in the next section.

2.4 Aperture-coupled patch antenna arrays

The developed microstrip-fed patch antenna arrays, when expanded into a 2×2 array (the results are not shown here), had two primary shortcomings - unwanted parasitic coupling between the feed network and the patch elements that led to radiation pattern distortion and the high cross-polarization level for the 35 GHz array. To overcome these problems, two improvements were introduced. First, a separate layer was introduced to place the feed networks beneath the ground plane, thereby alleviating the parasitic radiation problem. Coupling between the feed and the radiating elements is achieved using apertures in the ground plane - hence the name 'aperture-coupled array.' Second, the substrate configuration was changed to place the 35 GHz antennas in the middle layer on a thinner substrate while

placing the 14 GHz antennas on the top layer. The configuration used with the microstrip-fed array was chosen to minimize blockage effects on the 35 GHz antennas. However, the cross-polarization at 35 GHz is fundamentally dependent on the substrate thickness [51], and improvement is quite difficult using other means, specifically for this dual-polarization application. The blockage effects on the 35 GHz antennas, on the other hand, could be reduced by careful placement of antenna elements of both the arrays. The generic multilayer architecture of the aperture-coupled array is shown in Figure 2.10.

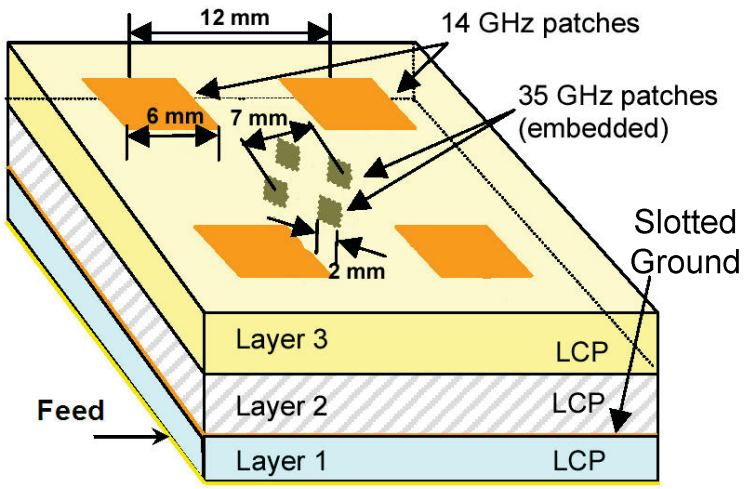

Figure 2.10: Generic multilayer architecture of the aperture-coupled antenna array.

2.4.1 Array design

The top view (with all the layers interlaced) and the side view of the aperture-coupled antenna array are shown in Figure 2.11. The metal used in simulation and fabrication for the ground plane, the antenna elements, and the feed network is Cu and has a thickness of 18 μm. The total substrate thickness for this configuration is 457 μm. The radiating elements for both arrays are placed on one side of the ground plane, while the feed network for both arrays is placed on the other side. The ground plane contains slots through which energy is electromagnetically coupled from the feed network to the radiating patches. With the ground plane taken as the reference, the 35 GHz patches are placed on a 127-μm thick LCP substrate, while the 14 GHz patches are placed on a 355-μm thick LCP substrate. The feed networks for both patches are placed on a 102-μm thick LCP substrate on the other

side of the ground plane. These substrate choices are again a result of an extensive analysis of their influence on antenna performance and were chosen to provide similar radiation patterns for both arrays while keeping a compact profile.

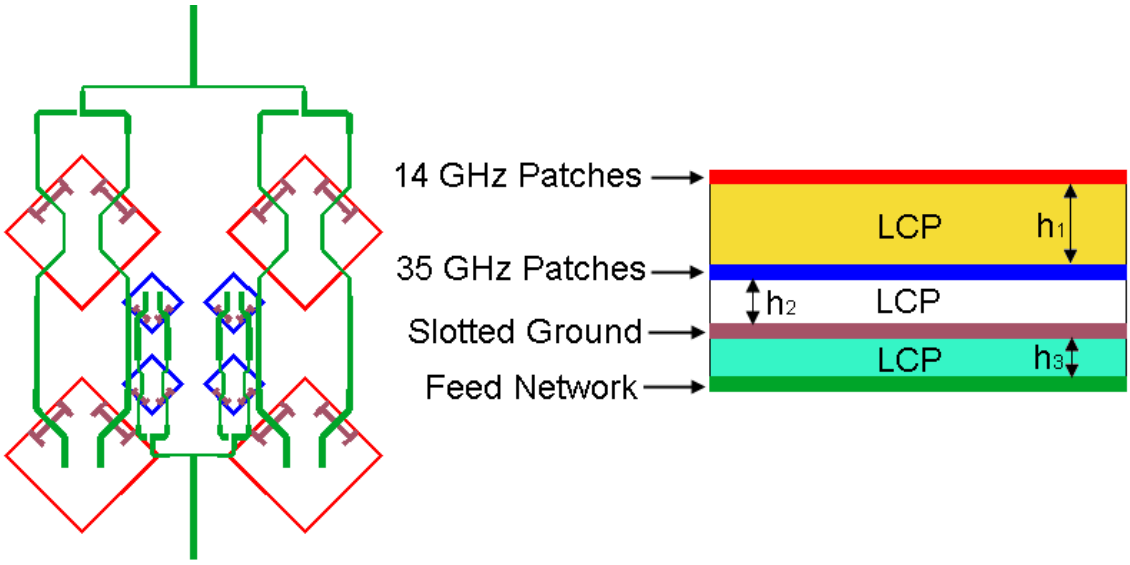

Figure 2.11: Aperture-coupled antenna array. Left: Top view with all the layers interlaced. Right: Side view. The thickness of the LCP substrates used are $h_1 = 228$ μm; $h_2 = 127$ μm; $h_3 = 102$ μm.

As shown in Figure 2.11, a combination of series and parallel feed was employed to form the 2×2 array. Each 2×2 array consists of two linear 2×1 arrays, which are formed by combining two basic elements that we define as 'End element' and 'Any element.' The development of the 2×2 array from these basic elements is explained in Figure 2.12. The most popularly used feed network for the formation of large arrays is the corporate feed network. In a corporate feed, all radiating elements are interconnected in a parallel feed configuration, so that uniform amplitude and phase distribution can be easily achieved. On the other hand, a series feed can result in a reduction of the overall length of the feed network and hence can reduce the associated feedline losses. The disadvantages of the series feed are beam-drifting and difficulties in achieving the desired amplitude distribution across the array. To take advantage of the characteristic features of both types of feed network, a combination of series and parallel feeds was used in this design. In the past, series feed networks have been employed with resistor terminations. Although this is an effective

method to design a series feed, it reduces the overall efficiency. In our work, we used a radiating element itself as a terminating element, thereby improving the overall efficiency of the array.

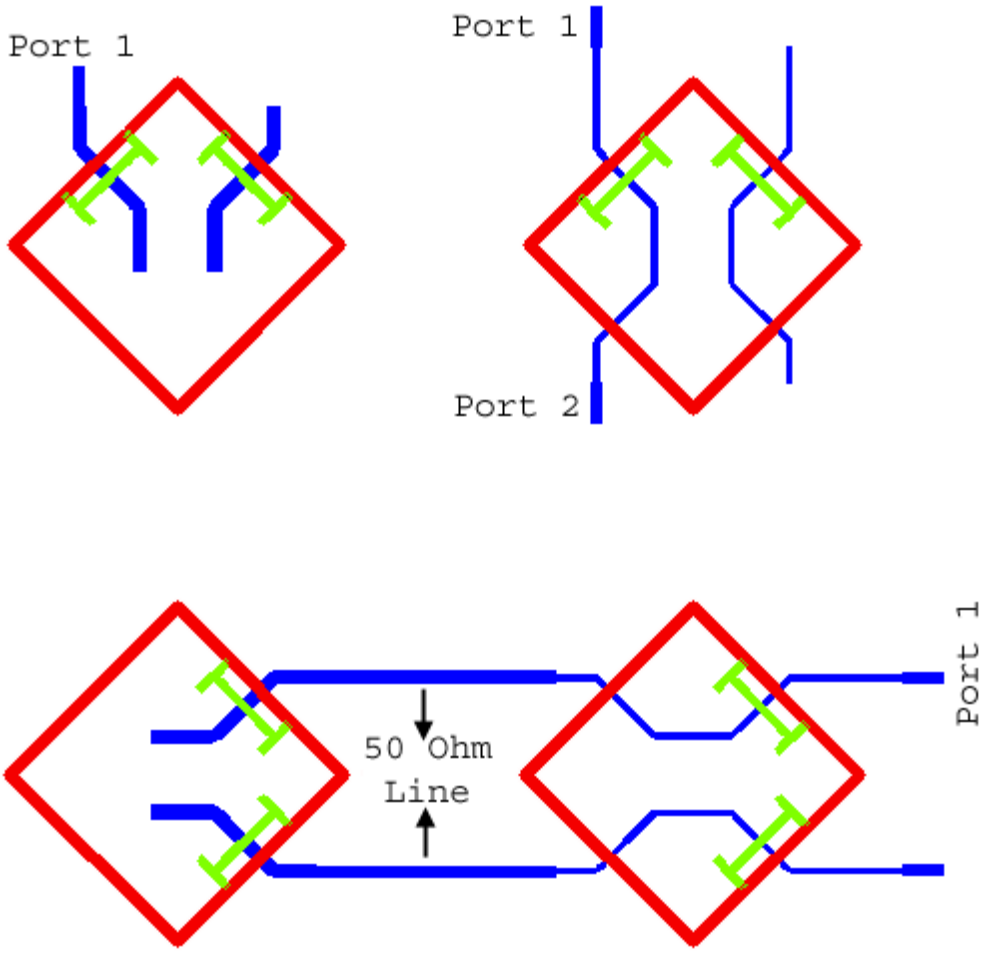

Figure 2.12: Development of the aperture-coupled array. Top Left: one-port 'End Element'. Top Right: two-port 'Any Element'. Bottom: Linear Array with one 'End Element' and one 'Any Element'. Several such linear arrays can be combined using a corporate feed to form a planar array [Refer Fig. 2.11]. The parallel feed line without ports in each case is for exciting the orthogonal polarization making this a dual-polarization system.

The 'End element,' as the name suggests, is the last element in the linear array (from the feed direction). It is a one-port device, with its patch and feed dimensions optimized to resonate at the desired frequency. The simulated return loss of the 'End element' resonating at 14 GHz is shown in Figure 2.13. The 'Any element' is a two-port device designed to provide a matched load at the resonant frequency at Port 1 when Port 2 is terminated with

a matched load. The simulated S-parameter characteristics of the 'Any element' for the 14 GHz array are shown in Figure 2.14. The linear array is then formed by connecting Port 1 of the 'End element' to Port 2 of the 'Any element.' Since the 'End element' is designed to resonate at the desired frequency, it presents a matched load at Port 2 of the 'Any element' at the resonant frequency, which in turn makes the linear array resonate at the desired frequency. It can be seen in Figure 2.14b that the insertion loss is close to -3 dB at the resonant frequency. The feed network and the slots for the 'Any element' are optimized in this case to provide equal amplitude split between antenna elements in a 2×1 linear array. A 50 Ω constant impedance transmission line is connected between the elements to maintain an appropriate distance between them in an array configuration. Since both the elements are matched to 50 Ω, the length of the transmission line can be used to control important radiation characteristics such as directivity, beamwidth, and broadside angle of the array. The 2×2 array is formed by combining two linear arrays using a corporate feed network. It is also possible to realize a general $N \times 1$ linear array by adding (N-1) 'Any elements' to an 'End element.' An $N \times N$ array could then be realized by combining N '$N \times 1$' arrays.

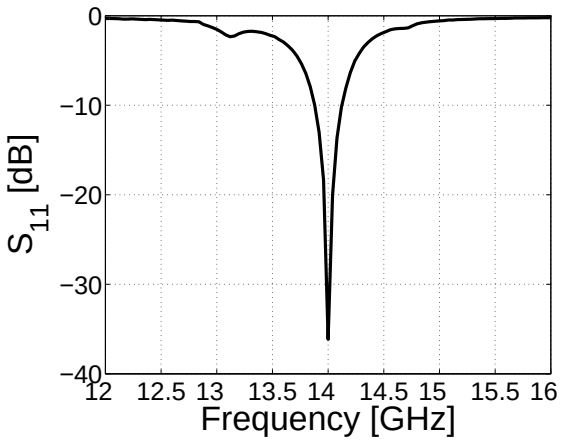

Figure 2.13: Simulated return loss of the 'end element' - 14 GHz array.

These aperture-coupled arrays offer some advantages over the previously developed microstrip-fed arrays. These include:

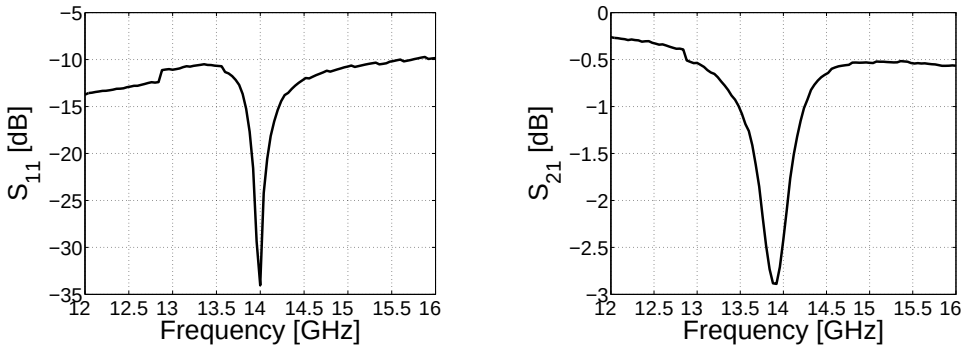

(a) Return loss (b) Insertion loss

Figure 2.14: Simulated S-parameter characteristics of the 'any element' - 14 GHz.

- No or minimum parasitic radiation from feed lines. This is expected to reduce distortion in the radiation pattern.
- For polarization reconfigurability, all switches can be placed in the same layer. This may significantly reduce the overall fabrication cost and complexity
- For an $N \times M$ array, the number of switches required is only $2N$. This is because of the use of series feed along one dimension of the array.

These benefits are offset by disadvantages, including:

- Design is relatively complicated. A corporate feed is much easier to design than a series/parallel combination feed.
- Four layers need to be patterned. This is a direct result of employing an aperture-coupled feed. This should be considered more as an additional cost rather than a disadvantage.
- Backside alignment is required. This arises from the particular substrate configuration chosen for the aperture-coupled array.
- Backside radiation is greater compared to the microstrip-fed design. Although both designs use finite ground planes, the slots in the aperture-coupled array tend to increase radiation on the backside.

These disadvantages notwithstanding, the aperture-coupled array is likely to fulfill all the requirements of the ESE system.

2.4.2 Measurements

The fabrication and measurement procedures are similar to the ones explained in Sections 2.4.2 and Sections 2.4.3, respectively. Figure 2.15a shows the individual patterned layers of the aperture-coupled array before bonding and Figure 2.15b shows the array after bonding.

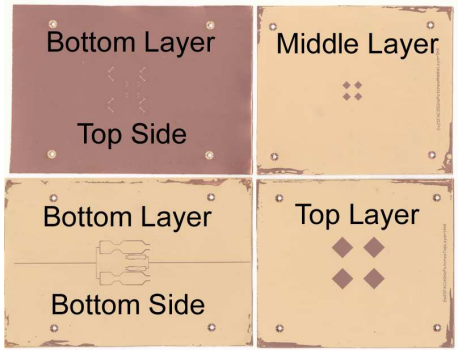

(a) Photo of the individual patterned layers of the aperture-coupled array.

(b) Photo of the bonded aperture-coupled array. Only the 14 GHz patches on the top layer are visible.

Figure 2.15: Images of the fabricated aperture-coupled array.

The simulated and measured return loss results of the 14 GHz array are shown in Figure 2.16. The impedance characteristics are summarized in Table 2.5. There is a slight shift in resonant frequency, probably because of fabrication tolerances. Figure 2.17 shows the return loss results for the 35 GHz array and Table 2.6 summarizes the impedance characteristics. Again, a shift in resonant frequency can be observed. The margin for error is very little at millimeter-wave frequencies (such as 35 GHz), especially for this multilayer design where precise alignment of the feed network, the electromagnetic slots, and the radiating patches is crucial. Additionally, the return loss levels could have been affected by the measurement setup. To achieve stable and repeatable measurements, the fabricated sample was mounted on a fixture and placed on a metal base. A foam spacer, with a dielectric constant close to that of free space ($\epsilon_r = 1$) and negligible loss tangent, was used to reduce reflections from the metal base. Although the arrangement did not significantly

alter the results, any reflection from the metal base would have reduced the return loss level. This might explain the discrepancy observed for the 14 GHz array that is electrically closer to the metal base because of its longer wavelength. The foam spacer setup had minimum impact on the 35 GHz array. For both arrays, the measured impedance bandwidths are in good agreement with the predicted values.

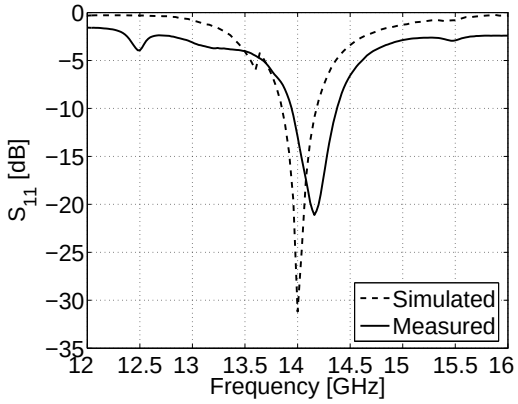

Figure 2.16: Return loss - 14 GHz aperture-coupled array.

Table 2.5: Return loss characteristics of the 14 GHz aperture-coupled array.

Characteristic	**Simulated**	**Measured**
Resonant Frequency	14 GHz	**14.16 GHz**
Return Loss	-31 dB	**-21 dB**
-10 dB Return Loss Bandwidth	280 MHz	**320 MHz**
Percent Bandwidth	2%	**2.28%**

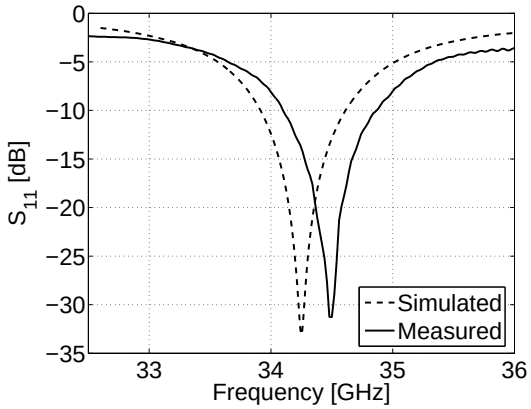

Figure 2.17: Return loss - 35 GHz aperture-coupled array.

Table 2.6: Return loss characteristics of the 35 GHz aperture-coupled array.

Characteristic	**Simulated**	**Measured**
Resonant Frequency	34.25 GHz	**34.5 GHz**
Return Loss	-33 dB	**-32 dB**
-10 dB Return Loss Bandwidth	710 MHz	**720 MHz**
Percent Bandwidth	2%	**2%**

The 2-D radiation pattern results for the 14 GHz are shown in Figures 2.18a and 2.18b. The radiation characteristics of the 14 GHz array are summarized in Table 2.7. The 2-D radiation pattern results for the 35 GHz are shown in Figures 2.19a and 2.19b. The radiation characteristics of the 35 GHz array are summarized in Table 2.8. The simulation and measured results agree very well. The shapes of the co-polarized beams and the beamwidths are in good agreement. The measured cross-polarization levels for the 35 GHz array are worse than the simulated levels. Furthermore, the measurement results show plenty of ripples in the cross-polarization beam not predicted in the simulations. In general, accurate measurement of a cross-polarized beam is far more difficult [84] than the measurement of a co-polarized beam. We are more interested in the average value of cross-polarization, which is approximately -18 dB in both the E and H planes. This, in our opinion, is a very good result for a 2×2 array with dual-polarization capabilities.

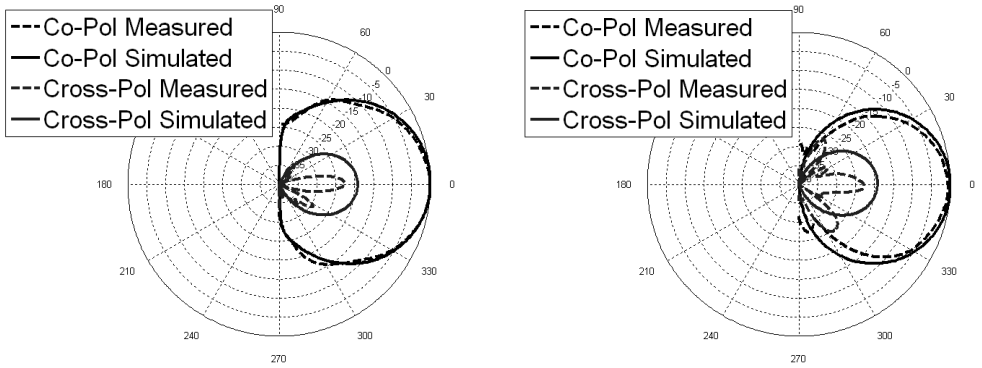

(a) E-plane patterns.

(b) H-plane patterns.

Figure 2.18: 2-D radiation patterns - 14 GHz aperture-coupled array.

Table 2.7: Radiation pattern characteristics of the 14 GHz aperture-coupled array.

Characteristic	Simulated	Measured
E-Plane -3 dB Beamwidth	49°	**48°**
H-Plane -3 dB Beamwidth	46°	**45°**
Max. Cross-pol.(E-plane)	-19 dB	**-21 dB**
Max. Cross-pol.(H-plane)	-19 dB	**-21 dB**

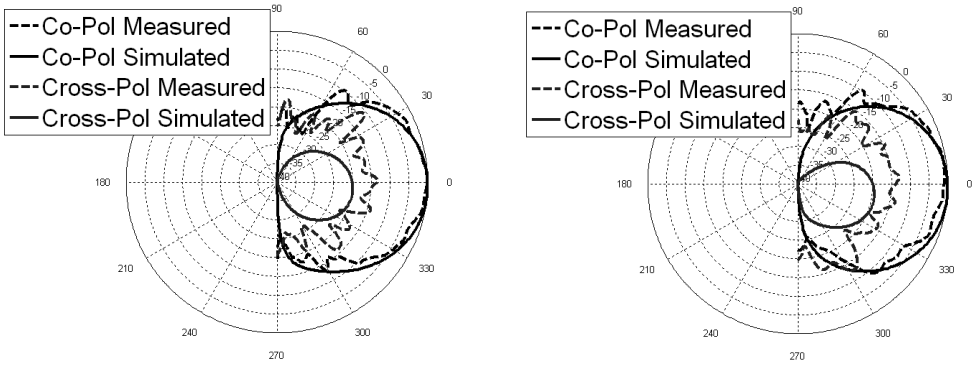

(a) E-plane patterns.

(b) H-plane patterns.

Figure 2.19: 2-D radiation patterns - 35 GHz aperture-coupled array.

Table 2.8: Radiation pattern characteristics of the 35 GHz aperture-coupled array.

Characteristic	Simulated	Measured
E-Plane -3 dB Beamwidth	51°	**49°**
H-Plane -3 dB Beamwidth	52°	**55°**
Max. Cross-pol.(E-plane)	-18 dB	**-14 dB**
Max. Cross-pol.(H-plane)	-18 dB	**-14 dB**

2.4.3 Efficiency calculations

Apart from the return loss and the radiation pattern measurements, efficiency measurements were also carried out. The efficiency of the 2×2 14 GHz aperture-coupled array was measured using the Wheeler Cap method [100], with cap dimensions of $10.8\ mm \times 34\ mm \times 65\ mm$. The efficiency is calculated based on input resistance measurements. Two sets of resistance measurements were made - one with the cap and one without. When a cap with proper dimensions is used to enclose the sample, it is possible to reduce the radiation levels to a negligible amount so that the measured input resistance is a measure of various losses only. The measurement without the cap is a measure of the total input resistance (i.e., the

radiation resistance and the loss resistance). From the two measurements, the radiation efficiency can be calculated. The radiation efficiency of the antenna is given by

$$\eta_{rad} = \frac{R_{rad}}{R_{rad} + R_{loss}} \tag{2.1}$$

where η_{rad} is the radiation efficiency, R_{rad} is the radiation resistance and R_{loss} is the loss resistance.

The measured efficiency of the entire setup that includes the array, the feed network, and the connector was 58.6%. To determine the efficiency of the antenna array only, it is necessary to de-embed the mismatch loss, the loss of the feed lines, and the connector. The return loss plot of the array shows that the mismatch loss is negligible. In Figure 2.15a, it can be seen that the input feed line has been extended to facilitate scattering parameter and radiation pattern measurements. The losses of the extended feed line and the corporate feed network were determined based on the attenuation measurements reported in [95]. The typical connector loss at 14 GHz is 0.15 dB. After de-embedding these losses, the efficiency of the antenna array is found to be 76.4%. Table 2.9 shows a summary of the measured efficiency, specific losses, and the de-embedded efficiency.

Table 2.9: Efficiency calculations of the 14 GHz aperture-coupled array.

Measured Efficiency *(Wheeler Cap Method)*	**58.6%**
Mismatch Loss (dB)	0.00 (100%)
Connector Loss (dB)	0.15 (96.6%)
Feedline Loss (dB)	1 (79.5%)
Total Loss (dB)	1.15 (76.7%)
De-embedded Efficiency	**76.4%**

It should be noted that the feed line loss used in calculating the de-embedded efficiency included only the loss of the extended input feed and the main corporate branch. As a result, the calculated efficiency is only a conservative estimate. Despite this, the result compares favorably to the reported efficiencies of similar antenna arrays realized on other substrate technologies.

All the results shown are for one polarization, but they are the same for the other orthogonal polarization also because of the symmetric arrangement of radiating elements and the feed network. Thus the designs can function as a dual-frequency and dual-polarization antenna array system.

Table 2.10 compares and contrasts this research work with other contemporary research on multilayer antenna arrays.

Table 2.10: Comparison between this work and other contemporary research on multilayer antenna arrays.

Source	**Technology**	**Attributes**
Kamagowa, *et. al* [56]	Polyimide/Ceramic	high-temperature, expensive
Granholm, *et. al* [40]	Duroid/FR-4/Foam	structural stability
Navarro, *et. al* [71]	Synthetic substrates	mechanical weakness
This work	**Multilayer LCP**	**Conformal, homogeneous, low-temperature, low-cost**

To realize a polarization reconfigurable system (i.e., to switch between polarizations in real time), switches need to be integrated with the current arrays. To achieve this, the feed networks for the arrays were modified to include bias pads for the switches. The integration of switches with the aperture-coupled antenna array is described in the next section.

2.5 Polarization-reconfigurable antenna arrays using RF MEMS switches

Real-time polarization reconfigurability can be achieved by integrating switches and the associated control circuitry with the designed antenna arrays. Although the polarization of an antenna array can be changed by mechanically rotating the antenna structure, it is not suitable for large-sized arrays proposed for the application of concern. Electronic switches not only reduce the overall cost, but also are more reliable compared to a mechanical rotating system. In the past, solid state switching elements such as p-i-n diodes, field-effect transistors (FETs), and other monolithic microwave integrated circuits (MMICs) have been employed for such applications. These devices have several disadvantages, such as high insertion loss, high power consumption, and non-linear characteristics. The losses could degrade the system sensitivity, and the power consumption is a concern for the proposed

space-borne application.

MEMS switches, which allow mass production, can be a viable alternative. Because they are compatible with the fabrication process of the proposed antenna arrays, the overall cost of the system can be reduced.

2.5.1 MEMS characteristic features

Some desirable features of the MEMS switches are outlined below:

- Low insertion loss
- Negligible power consumption
- Linear characteristics
- Low cost

Of course, like any other technology, MEMS switches have their share of disadvantages:

- Switching speed in the microsecond to millisecond range
- Low power-handling capability, typically less than 100 mW
- High voltage drive requirement
- Less reliable compared to solid state switches

2.5.2 MEMS-integrated array design

The top view of the designed aperture-coupled array, showing the switch locations and bias pads, is depicted in Figure 2.20. The location and the orientation of the bias pads and radial stubs are slightly modified for the 35 GHz array to efficiently utilize the available space. This configuration also minimizes the interaction between various stubs and the feed network. The total length of each radial stub is adjusted to produce an open at the operating frequency. The transformers and the combiners of the corporate feed network were optimized to minimize the effects of the bias stubs on the resonant frequency of the arrays. The polarization of both 14 and 35 GHz arrays is controlled by the configuration

of the MEMS switches. Because dedicated feed network and MEMS switches are provided for the two antenna arrays, the polarization of one array can be chosen independent of the other. Table 2.11 shows the different configuration of switches that can be used to enforce the desired linear polarization for a particular array.

Table 2.11: Switch configurations for the polarization-reconfigurable antenna array.

State	**Switches that are 'ON'**	**Switches that are 'OFF'**	**14 GHz**	**35 GHz**
a_0	none	all	not excited	not excited
a_1	S_1, S_3	S_2, S_4, S_5, S_6, S_7, S_8	Pol-I	not excited
a_2	S_2, S_4	S_1, S_3, S_5, S_6, S_7, S_8	Pol-II	not excited
a_3	S_5, S_7	S_1, S_2, S_3, S_4, S_6, S_8	not excited	Pol-I
a_4	S_6, S_8	S_1, S_2, S_3, S_4, S_5, S_7	not excited	Pol-II
a_5	S_1, S_3, S_5, S_7	S_2, S_4, S_6, S_8	Pol-I	Pol-I
a_6	S_2, S_4, S_6, S_8	S_1, S_3, S_5, S_7	Pol-II	Pol-II

Other switch configurations are also possible. The listed configurations are the most useful for the proposed application. Measurements were not made for the last two states outlined in the table (a_5, and a_6), because of setup constraints. These two states require simultaneous excitation of the array at two frequencies.

2.5.3 MEMS fabrication

The fabrication procedure is similar to the one detailed in Section 2.3.2, except for the integration of MEMS switches. The whole fabrication process can be thought of as containing three steps:

- Fabrication of the designed antenna array except the feed layer containing the MEMS switches.
- Preparation of the fabricated sample for MEMS integration.
- MEMS fabrication.

Of these three steps, this author carried out the first two, while MEMS fabrication was performed by Guoan Wang, another member in our research group. For the sake of completeness, a brief description of the MEMS fabrication procedure is included in this thesis.

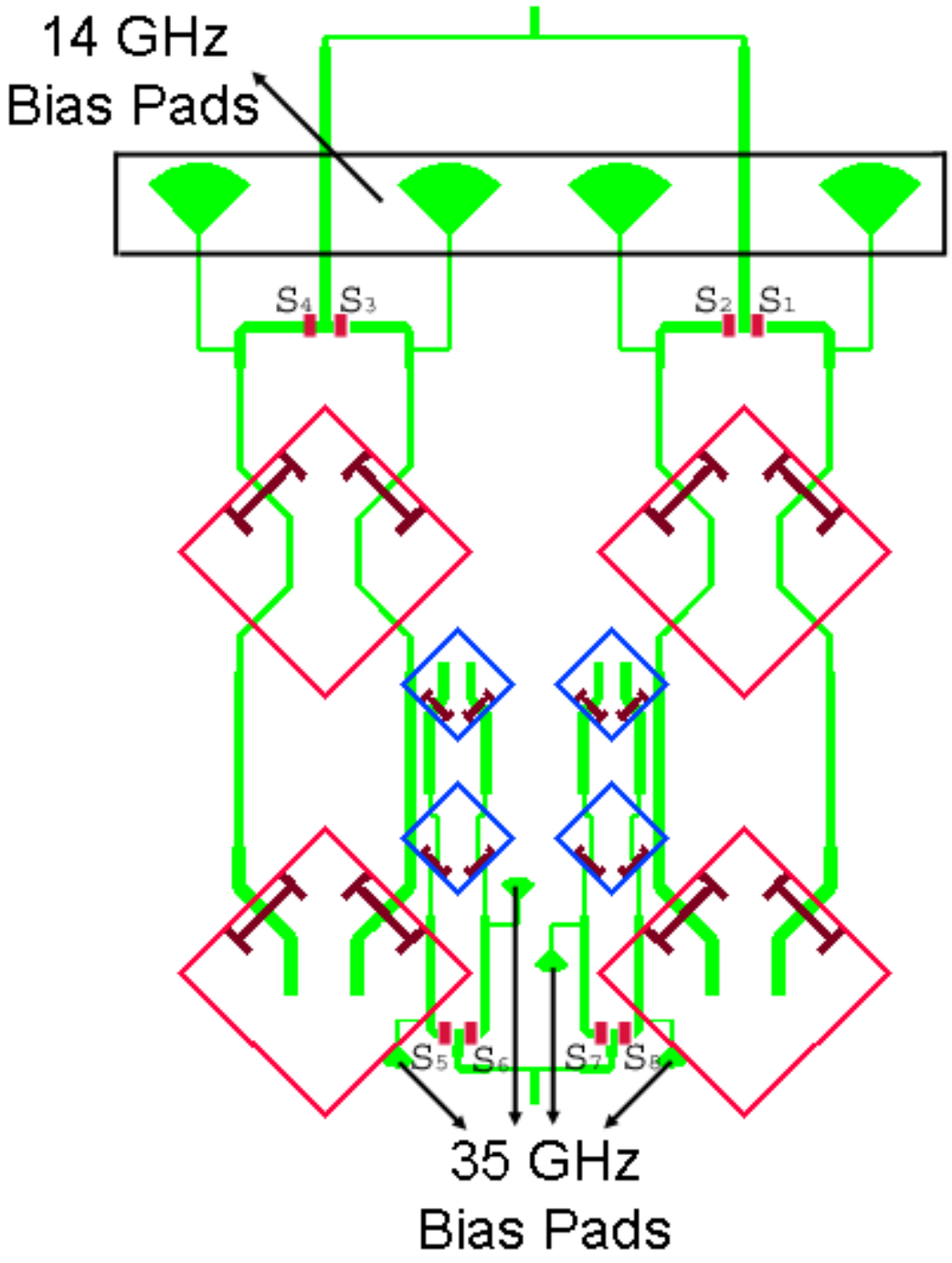

Figure 2.20: Polarization-reconfigurable aperture-coupled antenna array showing switch locations and bias pads.

Fabricating MEMS switches on a flexible, organic substrate like LCP is not a straightforward process. Being a flexible material, LCP is prone to curling. This effect becomes

more pronounced throughout processing because of the fluctuation of temperature from the various baking, deposition, and etching steps. Since optical lithography with a 3–5 μm resolution cannot be performed on a curled substrate, it is necessary to mount the sample on a flat, cleanroom-grade material before processing. Temporary mounting can be done using a spin-on or roll-on adhesive. Permanent mounting can be done using a thermal bonding technique. Alternatively, if a mask aligner with a vacuum chuck is available, then no mounting is necessary. Since the substrate is also an organic polymer, surface roughness is an issue. The surface roughness of bare LCP is usually on the order of 2–5 μm. Given that the switch membrane is generally suspended 2–3 μm above the substrate, the surface roughness can be large enough to prevent the switch from deflecting. To solve this problem, each sample was mechanically polished using a commercially available alumina slurry. The approximate time to polish a four-inch circular sample is 60 minutes. After polishing, the surface roughness of the sample was measured to be between 10 and 50 nm, smooth enough for MEMS switch operation.

After the substrate was polished and mounted on a flat material, the following procedure was followed to fabricate the MEMS switches:

Step 1 A 300$\mathring{A}$-titanium/2500$\mathring{A}$-gold layer was electron beam evaporated, patterned, and etched using chemical etchants. This is to provide the transmission line metal for the feed layer.

Step 2 A 2000$\mathring{A}$ silicon nitride layer was deposited using low-temperature plasma-enhanced chemical vapor deposition (PECVD).

Step 3 The deposited silicon nitride layer was patterned and etched using a reactive ion etch (RIE) process everywhere except for the MEMS switch contact areas.

Step 4 A 2–3 μm micron thick photoresist layer was patterned to provide a sacrificial layer for the membrane.

Step 5 Gold was evaporated, patterned, electroplated to a thickness of 2 μm, and etched to create the membrane.

Step 6 The sacrificial layer was dissolved using photoresist stripper leaving the membrane suspended above the signal lines.

Step 7 The switches were dried using carbon dioxide at the supercritical point to prevent membrane collapse due to water surface tension.

Figure 2.21 shows a picture of the feed layer of the fabricated antenna array that includes MEMS switches. Figure 2.22 shows a close-up view of the fabricated MEMS switches.

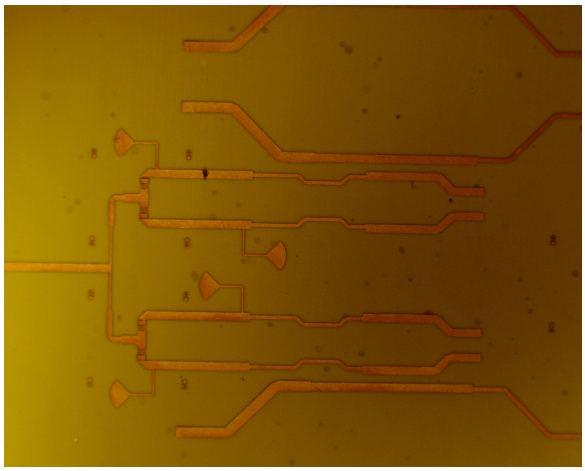

Figure 2.21: Photo of the fabricated antenna array showing the feed layer with MEMS switches.

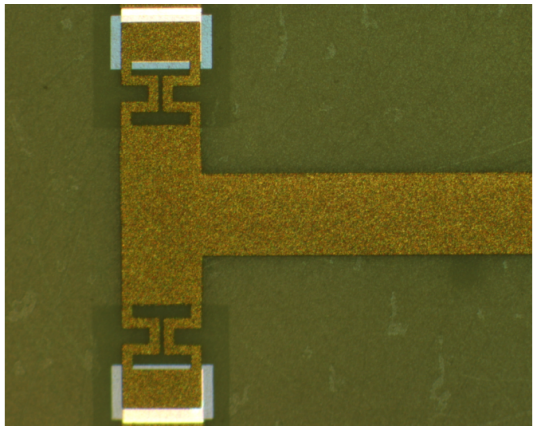

Figure 2.22: Close-up view of a fabricated MEMS switch.

2.5.4 Results and discussions

Scattering parameter measurements were made for both the 14 and 35 GHz arrays. The measurement setup is identical to the one described in Section 2.3.3, except for the additional DC probes required to actuate the MEMS switches. When the 14 GHz array was excited, the 35 GHz array was treated as a parasitic element and vice versa. Figure 2.23 shows the measurement setup with the DC bias probes.

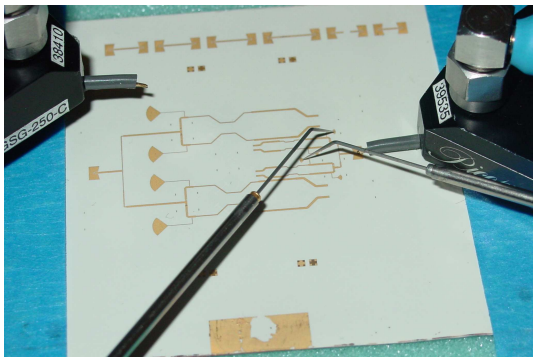

Figure 2.23: Measurement setup for the MEMS-integrated array showing the DC bias probes.

Figures 2.24 and 2.25 show the scattering parameter performance of the arrays for different switch configurations. For the 14 GHz array, when polarization-I is excited, the resonant frequency is 14.7 GHz and the return loss level is -34 dB and when polarization-II is excited, the resonant frequency is 14.8 GHz and the corresponding return loss level is -43 dB. For the 35 GHz array, when polarization-I is excited, the resonant frequency is 36.9 GHz and the return loss level is -16 dB and when polarization II is excited, the resonant frequency is 36.4 GHz and the corresponding return loss level is -23 dB. When all the switches are in the 'OFF' state, the radiating patches are not excited and the expected return loss level is 0 dB. This value is -0.8 dB for the 14 GHz array and -0.6 dB for the 35 GHz array. These figures represent the feed line losses and are satisfactory compared to the return loss levels when the patches are excited in one of the two polarizations. Apart from the losses, a negligible amount of energy might have coupled to the radiating patches because of the 'OFF' state capacitance of the MEMS switches.

A considerable shift in the operating frequency can be noted in each case. We believe

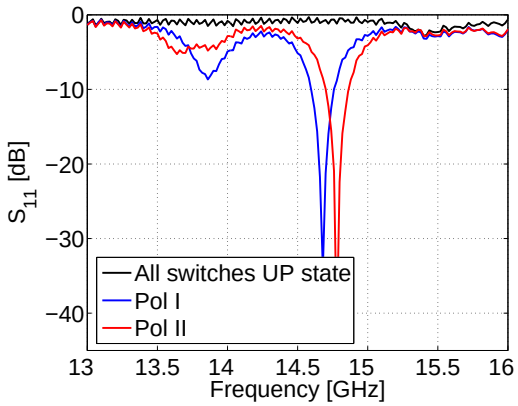

Figure 2.24: Return loss - 14 GHz aperture-coupled array with MEMS.

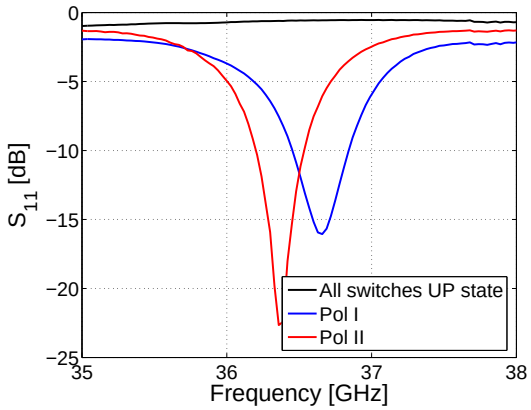

Figure 2.25: Return loss - 35 GHz aperture-coupled array with MEMS.

that the shift is due to the dispersion of dielectric constant of the substrate. This assessment is based on the study on the sensitivity of the resonant frequency of this type of antenna to the dielectric constant [93]. The LCP material used for fabrication of these MEMS arrays belonged to a new batch obtained from Rogers Corporation and could have had a lower dielectric constant compared to the older batches, whose characterization formed the basis for designing these arrays. Another reason for the resonance shift could be the capacitive MEMS switches whose effect was not simulated. However, the resonant shift between the two polarizations is very small for both the arrays, confirming the applicability of these designs for the proposed dual-polarization remote-sensing application.

Table 2.12 compares this work with the state-of-the-art research on reconfigurable antenna systems.

Table 2.12: Comparison between this work and other contemporary research on reconfigurable antenna systems.

Source	Technology	Attributes
Peroulis, *et. al* [74]	p-i-n diodes on Duroid	high-loss, not monolithic
Anagnostou, *et. al* [15]	MEMS on silicon	non-ideal antenna substrate
Cetiner, *et. al* [28]	MEMS on FR-4	only for $f \leq 10\ GHz$
Jung, *et. al* [55]	MEMS on Rogers TMM3	rigid, non-conformal
This work	**MEMS on multilayer LCP**	**conformal, low-loss, low-cost mm-wave, integrated**

2.6 Chapter summary

In this chapter, we presented the development of dual-frequency/dual-polarization antenna arrays on multilayer LCP technology. A simple microstrip-fed array and a complex aperture-coupled array have been developed. The design methodologies were described and the performance characteristics of the two arrays were compared. The lamination capabilities of LCP for developing complex multilayer architectures have been explored. An efficiency of 77% has been measured for the 14 GHz aperture-coupled array, confirming the advantages of LCP for use in antenna applications. In addition, MEMS switches have been integrated with the aperture-coupled array at both 14 and 35 GHz to achieve real-time polarization reconfigurability. This is the first time a MEMS-integrated reconfigurable array has been developed on a multilayer organic technology.

The results shown here demonstrate the applicability of LCP for the development of low-cost, light-weight, and conformal antennas for future communication and remote sensing systems operating up to millimeter-wave frequency ranges.

CHAPTER III

SINGLE LAYER MICROSTRIP LOW-PASS AND BAND-PASS FILTERS

3.1 Introduction

Filters are essential components in many communication systems as they perform the important tasks of channel selection (or rejection) and signal separation. The evaluation of LCP's electrical performance cannot be complete without implementing and characterizing these crucial devices.

Filters can be classified based on the media used for their implementation. These media include waveguides, coaxial lines, dielectric resonators, evanescent-mode designs, acoustic filters, and printed circuit designs [62]. Each medium has advantages and some may be more suitable than others, depending on the filter requirements. For example, waveguide filters are superior as far as electrical characteristics such as insertion loss and quality factor are concerned, but are hard to implement at sub-millimeter-wave frequencies. Dielectric resonator filters can give size advantages over conventional waveguide filters, but are relatively expensive. Printed circuit designs provide many benefits, especially in realizing a low-profile, low-cost, and fully integrated system.

LCP, as discussed in Chapter 1, is a favorable technology for implementing printed circuit type filters. Although the low dielectric constant property of LCP provides it with specific gains over competing technologies as far as antenna implementation is concerned, it is not ideal for implementing filters or other devices whose size scales with the operating wavelength. Hence, one needs to be creative with designing and implementing filters on LCP to keep it on par with other material technologies with high dielectric constant. Therefore, the objective of this section of the research is twofold. First is to design and implement filters of different kinds that operate at a wide range of frequencies so as to assess the electrical performance of LCP over those frequency ranges. Second is to focus on novel

design and implementation methods to realize filters on LCP with performances comparable to or better than those implemented on alternate technologies. Of course, the multilayer capability of LCP allows placing different sections of a filter on different layers, thereby minimizing its lateral area and keeping an overall compact size. In this chapter, the design and implementation of several filters, operating in a wide range of frequencies, on single-layer LCP technology is presented. The next chapter presents examples of filters utilizing multilayer lamination capabilities of LCP.

Filter design in itself is a broad research topic. Within the classification of printed circuit type filters, several subclassifications such as microstrip, coplanar waveguide, and stripline implementations exist. Our focus is on microstrip low-pass and band-pass filters. Although the fundamental goal here is to develop prototype circuits operating in a wide range of frequencies, novel design techniques are explored to provide added value. To meet the stringent requirements of modern wireless systems, filters are required to have low insertion loss, high return loss, and high slope selectivity simultaneously. Pseudo-elliptic filters with finite frequency transmission zeros are known to provide optimal results [69]. Most of the filters developed in this work belong to this category of filters.

3.2 Low-pass filters using stepped impedance resonators

3.2.1 Lumped element design

Compact low-pass filter designs with a sharp attenuation response are challenging. Most conventional approaches are Butterworth or Chebyshev type, but they require a high-order design (at least 5th order) to ensure a good selectivity near the pass-band since they have no attenuation poles [79]. Elliptic-function filters have attenuation poles near their pass-bands, making them very attractive for high-selectivity applications. But a high-order design is also required to ensure simultaneously a flat response in the pass-band (because attenuation zeros) and a good out-of-band attenuation (because attenuation poles)[67]. In all cases, a compact planar design is practically hard to achieve because of the number and the size of components to be implemented (i.e., long high-impedance lines, wide low-impedance lines, long open stubs) using the semi-lumped component approach.

To address these issues, this composite design combines four filter sections: a constant-k, an m-derived sharp cutoff, and two m-derived matching sections, as described in Figure 3.1. Each section is designed by the image parameter method to obtain the lumped element schematic [69].

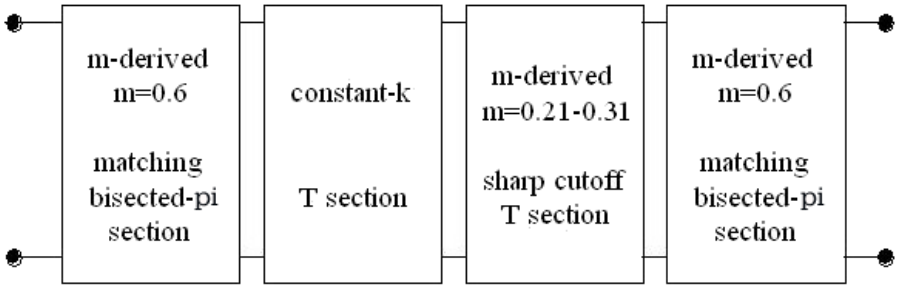

Figure 3.1: Composite design concept combining four filter sections

The design starts with the calculation of the constant-k section and the m-derived section in T form with respect to the desired characteristic impedance R_o, cutoff frequency f_o (of the constant-k T section), and the parameter m. The parameter m sets the placement of an attenuation pole near the cutoff frequency for a sharp attenuation response. A filter of lower order is then required for a fast attenuation rate past the cutoff frequency and the attenuation pole can be easily tuned to suppress an arbitrary unwanted frequency. This leads to a reduction in the number of components and therefore a reduction of the area and the cost of the filter. In this work, m values of 0.21 and 0.308 have been implemented and have resulted in good measured performance. The last step of the design is the addition of two bisected-p m-derived sections at the ends of the filter. The image impedance of an m-derived p section depends on m. A value of m= 0.6 is used to minimize the variation of the image impedance over the pass-band of the filter and optimize the matching properties to the nominal source and load impedance.

The four sections are then cascaded and the series pairs of inductors are combined, leading to the complete filter schematic described in Figure 3.2. The theoretical expression and the values of the lumped elements for various filters designed in this work are presented in Table 3.1. The characteristic impedance R_o has been fixed to 50 Ω in all cases.

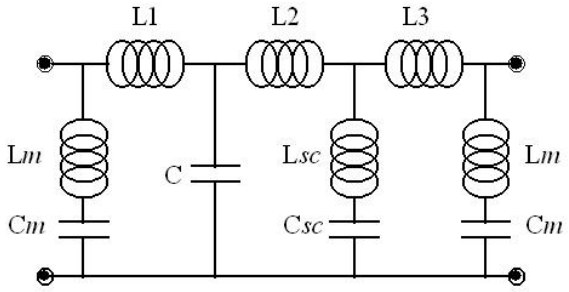

Figure 3.2: Complete composite low-pass filter schematic

Table 3.1: Theoretical expression and value of the lumped elements

	Expression	**Design 1** $\mathbf{f_o = 5.1}$ **GHz** m = 0.308	**Design 2** $\mathbf{f_o = 7.6}$ **GHz** m = 0.21	**Design 3** $\mathbf{f_o = 27}$ **GHz** m = 0.26	**Design 4** $\mathbf{f_o = 59}$ **GHz** m = 0.3
C	$2/(R_o.2.\pi.f_o)$	1.19 pF	0.79 pF	0.2274 pF	0.1026 pF
L	$2.R_o/(2.\pi.f_o)$	2.98 nH	1.99 nH	0.5686 nH	0.2567 nH
L1	$0.8L$	2.38 nH	1.59 nH	0.4548 nH	0.2053 nH
L2	$L(1+m)/2$	1.95 nH	1.20 nH	0.3582 nH	0.1668 nH
L3	$L(0.6+m)/2$	1.35 nH	0.80 nH	0.2440 nH	0.1155 nH
Lsc	$L(1-m^2)/(4m)$	2.19 nH	2.27 nH	0.5097 nH	0.1946 nH
Csc	$m.C$	0.36 pF	0.16 pF	0.0591 pF	0.0309 pF
Lm	$0.53L$	1.58 nH	1.06 nH	0.3013 nH	0.1369 nH
Cm	$0.3C$	0.36 pF	0.24 pF	0.0682 pF	0.0309 pF

3.2.2 Lumped element-microstrip transformation

The LCP substrate chosen for microstrip implementation of the designed filters is characterized by $\epsilon_r = 2.9 - 3.15$, $tan\delta = 0.002 - 0.004$, a substrate thickness of 100 μm, and a conductor thickness of 9 μm. In this configuration, the lowest and highest practical impedance lines are, respectively, around 10 Ω for a line width of 2000 μm and 90 Ω for a line width of 75 μm.

The middle section of the filter, composed of L1, C, and L2 (Fig. 3.2), was implemented using the conventional stepped impedance technique. The implementation of L3 can be deduced the same way. A folded structure was chosen and optimized using full wave simulations to avoid the impact of stub excessive length on the overall filter size. Figure 3.3a shows an example of a fabricated folded filter, and its simulated and measured performances are shown in Figure 3.3b.

The m-derived sections are made of series LC resonators that can be approximated by

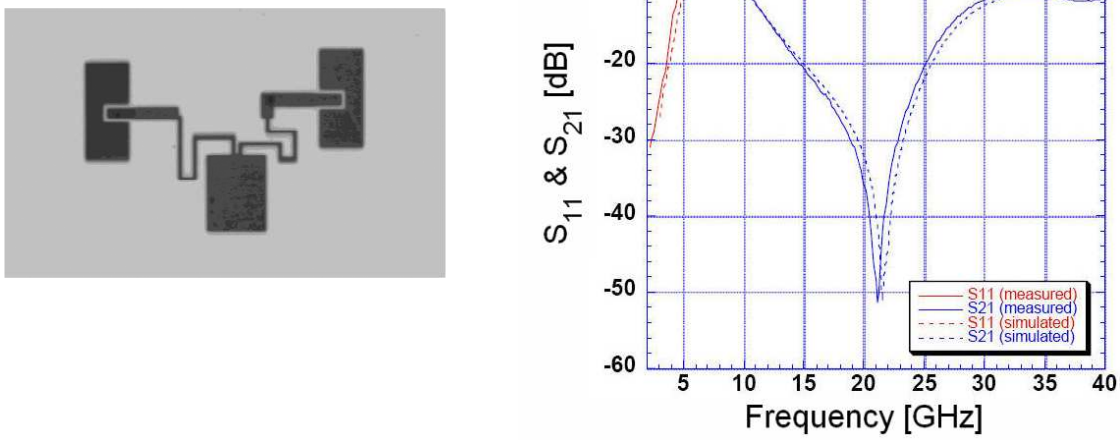

(a) Photo of a folded stepped impedance low-pass filter

(b) Measured and simulated S-parameter results

Figure 3.3: Stepped impedance low-pass filter

a quarter-wavelength open-circuited micro-strip stub. Stub resonators are very popular, but occupy a large area and often require characteristic impedances that are difficult to realize. In past research efforts, stepped impedance resonators (SIR), with a compact size and strong resonance, have been used as a replacement for conventional stubs. In this work, we used a folded SIR to get simultaneously a strong attenuation pole and a very compact size. The layout of these resonators has been optimized using IE3D [6], a full-wave MOM solver, to get the strongest rejection properties at the attenuation pole frequencies defined by the LC resonators in the m-derived sections while maintaining a flat response in the pass-band. Figure 3.4a shows an example of a fabricated folded SIR and its simulated, and measured performances are shown in Figure 3.4b.

These resonators were then combined with the stepped impedance filter and L3 to construct the complete composite filter. A final layout optimization is performed to fine tune the structure and get the minimal size.

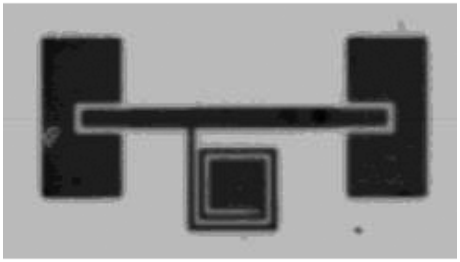

(a) Photo of a fabricated folded SIR

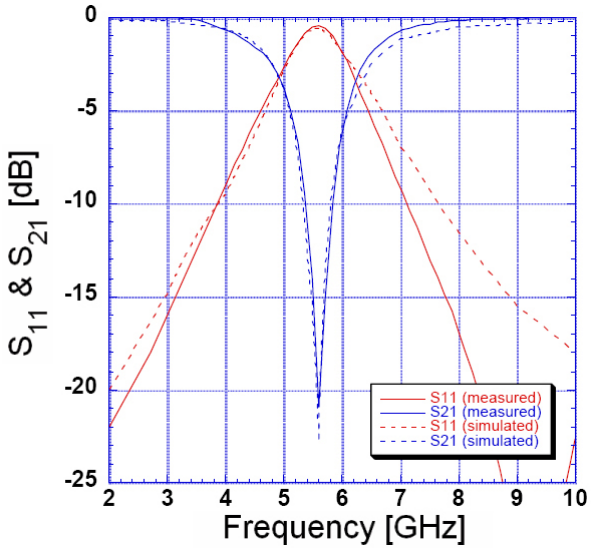

(b) Measured and simulated S-parameter results

Figure 3.4: Stepped impedance resonator (SIR)

3.2.3 Measurements and discussions

Figure 3.5a shows a photo of the fabricated folded filter with $f_o = 5.1$ GHz (Design 1). The filter layout exhibits a very compact area of $4.6 \times 3.8\ mm^2$. The layout has been optimized to get the strongest rejection properties at 5.6 GHz and 6.7 GHz. Figure 3.6a shows a photo of the fabricated folded filter with $f_o = 7.6$ GHz (Design 2). The filter layout exhibits a very compact area of $3 \times 4\ mm^2$. The layout has been optimized to get the strongest rejection properties at 8.2 GHz and 10 GHz.

Figures 3.5b and 3.6b show the simulated and measured results of the RF filters shown in Figures 3.5a and 3.6a, respectively. A comparison of the performances achieved from the ideal lumped component simulations, the full wave simulations, and the measured prototypes is presented in Tables 3.2 and 3.3. The measurement of these filters, and of all the filters and resonators presented in this section were performed using coplanar waveguide probes. To facilitate such measurements, conductor-backed coplanar waveguide (CB-CPW)-microstrip transitions have been used. Although the vialess transition makes the ground plane floating, it is known to work well for measuring microstrip circuits [106]. These transitions were optimized to minimize the impedance mismatch between the probes and the 50

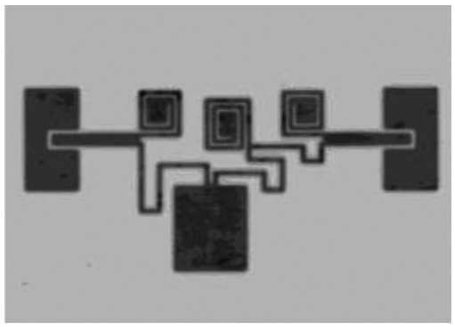

(a) Photo of the fabricated filter

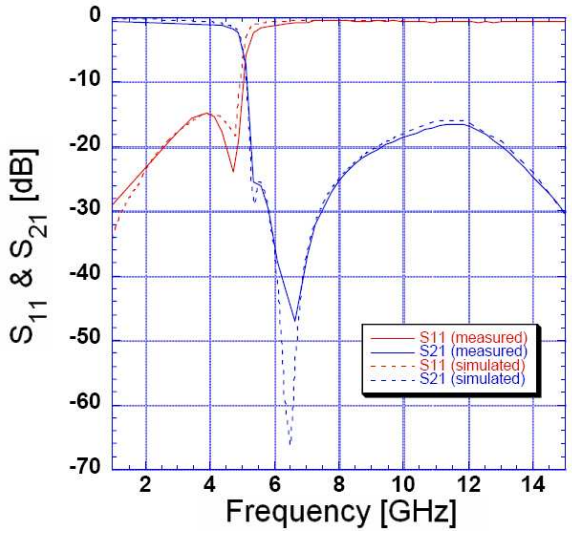

(b) Simulated and Measured S-parameter results

Figure 3.5: LPF with $f_0 = 5.1$ GHz (Design 1)

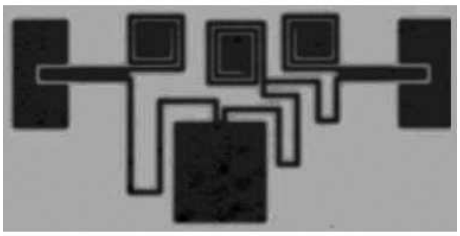

(a) Photo of the fabricated filter

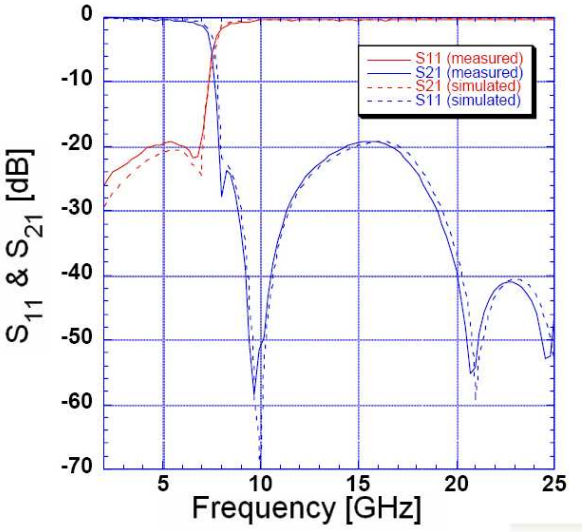

(b) Simulated and measured S-paramrter results

Figure 3.6: LPF with $f_0 = 7.6$ GHz (Design 2)

Ω input/ output feed lines. The loss effects were calibrated out using a through-reflect-line (TRL) calibration.

An excellent agreement with full wave simulation results has been achieved at RF frequencies. Rejection of the attenuated pole as high as 58 dB, good matching properties in

Table 3.2: Comparison of performances achieved from ideal lumped components, full wave simulations and measurements − C-band (Design 1)

Design 1	Loss (2 GHz) dB	f_c (3 dB) GHz	f I-pole GHz	Attenuation I-pole dB	f II-pole GHz	Attenuation II-pole dB
Lumped	0.2	5.1	5.6	-36	6.7	-79
Simulation	0.2	4.9	5.4	-29	6.5	-66
Measurement	**0.7**	**4.95**	**5.35**	**-28**	**6.5**	**-47**

Table 3.3: Comparison of performances achieved from ideal lumped components, full wave simulations and measurements − X-band (Design 2)

Design 2	Loss (3 GHz) dB	f_c (3 dB) GHz	f I-pole GHz	Attenuation I-pole dB	f II-pole GHz	Attenuation II-pole dB
Lumped	0.16	7.6	8.2	-25	10	-75
Simulation	0.17	7.55	8.1	-22	10	-69
Measurement	**0.2**	**7.4**	**8**	**-27**	**9.7**	**-58**

the pass band (< -20 dB), flat response (no ripples) in the pass-band, and low insertion loss in the pass band (0.2 dB at 3 GHz) have been measured for the second design. The first design exhibits similar performances but an additional 0.5 dB of insertion loss in the pass-band. This is due to series resistive losses occurring in the long high impedance lines used in this design.

Figure 3.7a shows a photo of the fabricated folded filter with $f_o = 27$ GHz (Design 3). The filter layout exhibits a very compact area of $1.5 \times 1.8\ mm^2$. The layout has been optimized to get the strongest rejection properties at 29.5 GHz and 35.1 GHz. Figure 3.8a shows a photo of the fabricated folded filter with $f_o = 59$ GHz (Design 4). The filter layout exhibits a very compact area of $1 \times 2\ mm^2$. The layout has been optimized to get the strongest rejection properties at 65.5 GHz and 77.5 GHz.

Figures 3.7b and 3.8b show the simulated and measured results of the millimeter-wave filters. A comparison of the performances achieved from the ideal lumped component simulations, the full wave simulations, and the measured devices is presented in Tables 3.4 and 3.5.

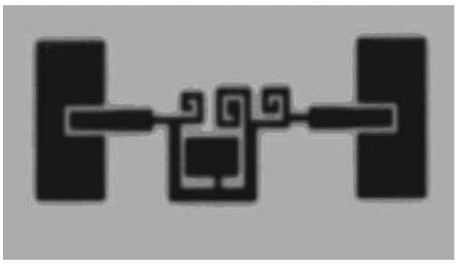

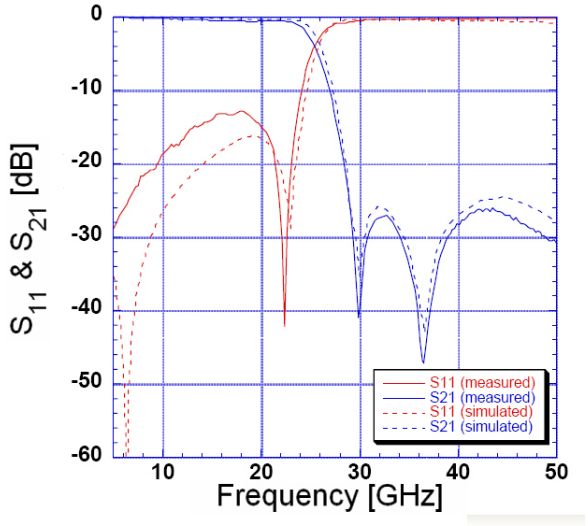

(a) Photo of the fabricated filter

(b) Simulated and measured S-parameter results

Figure 3.7: LPF with $f_0 = 27$ GHz (Design 3)

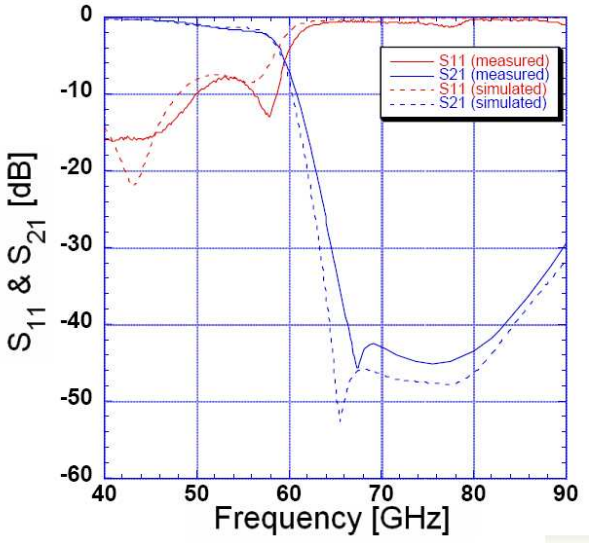

(a) Photo of the fabricated filter

(b) Simulated and measured S-parameter results

Figure 3.8: LPF with $f_0 = 59$ GHz (Design 4)

An excellent agreement with full wave simulation results has been achieved at millimeter-wave frequencies. Rejection of the attenuated pole as high as 47 dB, good matching properties in the pass band (< -13 dB), and low insertion loss in the pass band (0.2 dB at 10 GHz) have been measured for Design 3. Design 4 exhibits a similar performance but the layout has not been folded, because of its inherent compact size. The electrical performance

Table 3.4: Comparison of performances achieved from ideal lumped components, full wave simulations and measurements − Ka-band (Design 3)

Design 3	Loss (10 GHz) dB	f_c (3 dB) GHz	f I-pole GHz	Attenuation I-pole dB	f II-pole GHz	Attenuation II-pole dB
Lumped	0.15	27	29.5	-32	35.1	-77
Simulation	0.15	25.7	29.4	-35	36.5	-43
Measurement	**0.2**	**25**	**29.9**	**-41**	**36.5**	**-47**

Table 3.5: Comparison of performances achieved from ideal lumped components, full wave simulations and measurements − V-band (Design 4).

Design 4	Loss (20 GHz) dB	f_c (3 dB) GHz	f I-pole GHz	Attenuation I-pole dB	f II-pole GHz	Attenuation II-pole dB
Lumped	0.15	59	65.5	-35	77.5	-78
Simulation	0.15	58.2	65.5	-52	77	-47
Measurement	**0.2**	**58.3**	**67**	**-45**	**75**	**-45**

of the filters reported here confirms the low-loss characteristics of LCP at microwave and millimeter-wave frequencies. The measured attenuation characteristic of these filters can be compared to the one of maximally flat or 0.01 dB ripple filter design for an order of $n \geq 13$ [69]. It has been also demonstrated that compact designs can be achieved across a wide range of frequencies despite the low dielectric constant of the substrate.

Table 3.6 compares the C-band implementation achieved in this work to other implementations available in the literature. Because the comparison was made between implementations with different cut-off frequencies using different dielectric substrates, the size of the filters are expressed in terms of guided wavelength for a fair comparison of the design approaches. As can be seen from the figure, the results achieved in this work provide a good balance between size, loss, rejection, cost, and ease of implementation.

Table 3.6: Comparison of C-band filter performance reported in this work with other printed low-pass filter implementations available in the literature.

Source	**Design philosophy**	**Insertion loss**	**Rejection rate**	**Size**
Hsieh, *et. al* [47]	Hair-pin resonators	0.6 dB	54 dB/GHz	$0.62\lambda_g \times 0.17\lambda_g$
Li, *et .al* [63]	Coupled line, stubs,	0.5 dB	42 dB/GHz	$0.11\lambda_g \times 0.17\lambda_g$
Sheen [90]	Semi-lumped approach	N/A	36 dB/GHz	$0.09\lambda_g \times 0.07\lambda_g$
Mandal, *et. al* [66]	Defected ground	0.5 dB	130 dB/GHz	$0.23\lambda_g \times 0.09\lambda_g$
This work	**Folded SIR**	**0.7 dB**	**63 dB/GHz**	$\mathbf{0.13\lambda_g \times 0.11\lambda_g}$

3.3 Band-pass filters using folded open-loop resonators

The band-pass filters presented in this section and in the subsequent chapters were designed based on the theory of coupled resonators [46]. The advantage of this technique is that it is applicable to the design of any coupled resonator filter topology irrespective of the physical structure of the resonator. Starting with the filter specifications, a coupling matrix is generated. The elements of the coupling matrix represent the coupling coefficients of the inter-coupled resonators and the external quality factors of the input and output resonators. Once the coupling matrix is obtained and a resonator topology is chosen, numerical simulations can be performed to extract the physical parameters of the circuit that would yield the coupling coefficients and external quality factors specified by the synthesized coupling matrix. The concept of using a coupling matrix model for filter design is illustrated in Figure 3.9. This direct design approach is very useful in realizing advanced filtering circuits both in the sense of functional characteristics (symmetric/asymmetric response, real/imaginary finite transmission zeros) and in the sense of implementation characteristics (i.e. multilayer architectures.)

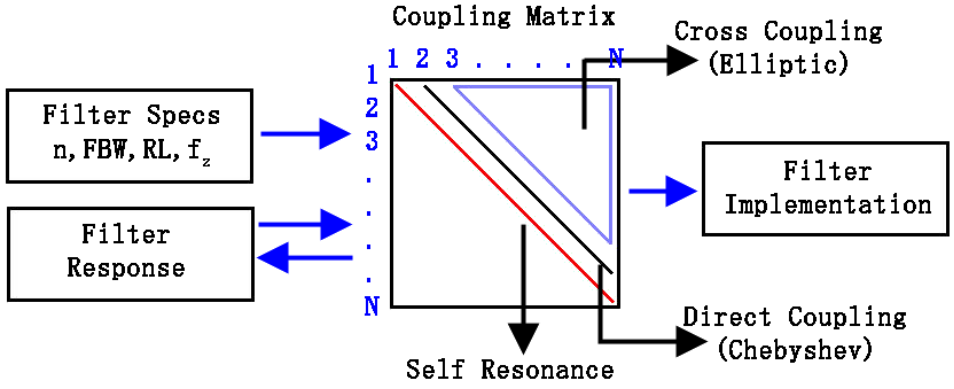

Figure 3.9: Filter design using coupling matrix synthesis.

3.3.1 Coupling matrix synthesis

The synthesis techniques reported in [26, 9] were used to generate the coupling matrices for any given filter specification. While the synthesis technique developed by Cameron does not involve any optimization procedure, it is restricted to few coupling topologies

and tedious similarity transformations are required, in general, to adapt this method to an arbitrary topology. Amari's optimization method provides an alternative to Cameron's direct synthesis technique and can be employed to synthesize coupling matrix of any coupling topology. We implemented both these algorithms in Matlab. These scripts were heavily used in the design of band-pass filters reported in this work.

To demonstrate the usefulness of this technique, two examples are provided here. The first example is a fourth order filter with center frequency at $f_0 = 10\ GHz$, a fractional bandwidth (FBW) of 8%, a return loss level (RLL) of 20 dB and transmission zeros at $f_{z1} = 9.2\ GHz$ and $f_{z2} = 10.8\ GHz$. The coupling topology proposed to realize this filter is shown in Figure 3.10. The synthesized coupling matrix is

$$M = \begin{bmatrix} 0 & 0.0697 & 0 & -0.0136 \\ 0.0697 & 0 & 0.0614 & 0 \\ 0 & 0.0614 & 0 & 0.0697 \\ -0.0136 & 0 & 0.0697 & 0 \end{bmatrix} \quad Q_e = 12.19 \tag{3.1}$$

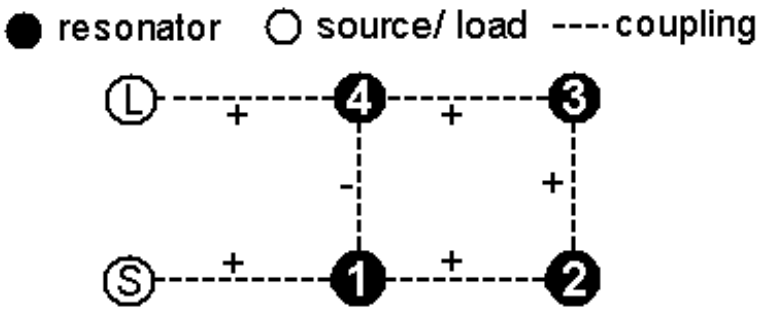

Figure 3.10: Coupling topology of example I with coupling coefficient signs.

Figure 3.11 shows the performance of the filter as described by the synthesized coupling matrix.

The second example is a fourth order filter with center frequency at $f_0 = 10\ GHz$, a FBW of 8%, a RLL of 20 dB and transmission zeros at $f_{z1} = 8.9\ GHz$ and $f_{z2} = 9.4\ GHz$. The coupling topology proposed to realize this filter is shown in Figure 3.12. The synthesized coupling matrix is

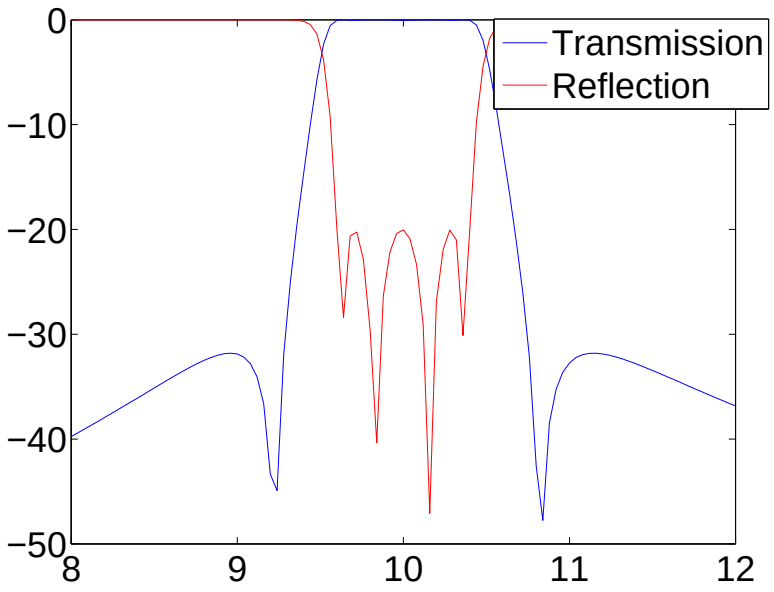

Figure 3.11: Performance obtained from coupling matrix in 3.1.

$$M = \begin{bmatrix} -0.0076 & 0.0738 & 0 & 0.0121 \\ 0.0738 & -0.0016 & 0.0351 & -0.0492 \\ 0 & 0.0351 & 0.0612 & 0.0550 \\ 0.0121 & -0.0492 & 0.0550 & -0.0076 \end{bmatrix} \quad Q_e = 12 \tag{3.2}$$

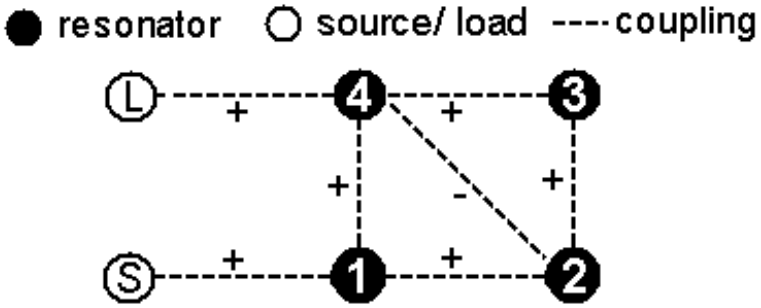

Figure 3.12: Coupling topology of example II with coupling coefficient signs.

Figure 3.13 shows the performance of the filter as described by the synthesized coupling matrix. Certain observations can be made from the synthesized coupling matrices and their performance characteristics. Coupling coefficients of both signs are, in general, required to realize finite frequency transmission zeros. For a symmetric filter, with transmission zeros at symmetrical locations on either side of the passband, the elements in the

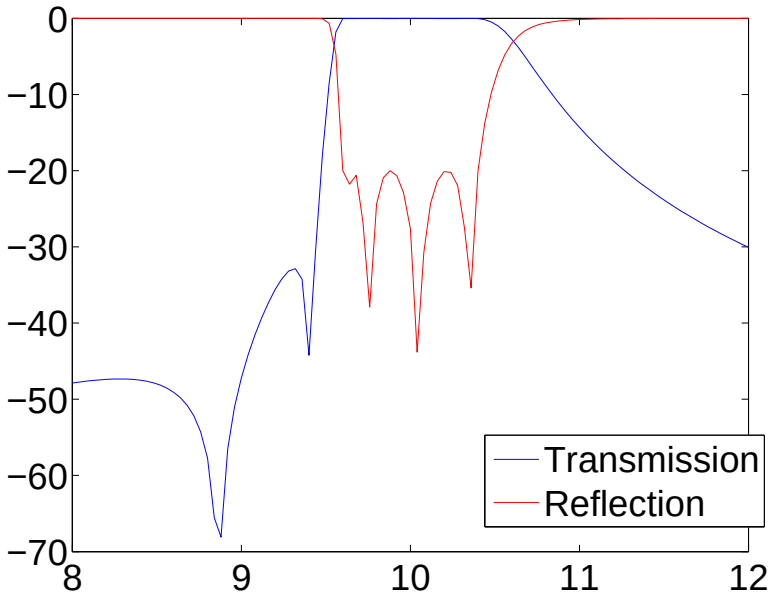

Figure 3.13: Performance obtained from coupling matrix in 3.2.

main diagonal of the coupling matrix are zero. This will require a synchronous tuning of the resonators. Two resonators are considered to be synchronously coupled, if they have an identical self-resonant frequency and identical response characteristics in the frequency band of interest. The elements in the main diagonal are non-zero for the filter with asymmetric characteristics. Resonators for implementation of such filters need to be asynchronously tuned. Asynchronously coupled resonators have different self-resonant frequencies. These requirements generally have an impact on the choice of resonators. Furthermore, in synthesizing the coupling matrices, it has been assumed that the resonators are lossless elements. In a practical case, this is not valid and, hence, further optimizations, though minimal, are often required.

3.3.2 Filter specifications and design

As mentioned before, the objective here is to develop band-pass prototype filters, operating in a wide range of frequencies, on LCP technology, so as to assess the electrical performance of LCP in those frequency ranges. The design, implementation, and measurement of prototype filters operating in the X-band, Ka-band, and V-band are presented here. All these

filters use the coupling topology shown in Figure 3.10 to meet the performance specifications outlined in Table 3.7. The elements of the coupling matrix synthesized to satisfy these specifications are summarized in Table 3.8.

Table 3.7: Performance specifications for the single-layer band-pass filter prototypes.

Prototype	$\mathbf{f_0}$ **GHz**	**FBW** %	**RLL dB**	$\mathbf{f_{z1}}$ **GHz**	$\mathbf{f_{z2}}$ **GHz**
X-band	10	8	20	9.2	10.8
Ka-band	35	8	20	32.3	37.9
V-band	61.5	8	20	56.7	66.6

Table 3.8: Coupling elements for the prototypes with topology as in figure 3.10.

Attribute	**Value**
Q_e	11.92
M_{12}	0.0697
M_{23}	0.0614
M_{34}	0.0697
M_{14}	-0.0136

Once the elements of the coupling matrix were determined, an appropriate resonator topology needs to be identified to implement the filter prototypes. Many choices are available. We used half-wavelength, folded, open-loop resonators and the canonical configuration proposed by Hong [44]. A folded resonator was used to achieve a compact size, which is critical for LCP technology because of its low dielectric constant. In addition, coupling coefficients of both signs are required as evident from Table 3.8. In a physical sense, this means that the resonators should have the capability of being both capacitively and inductively coupled with one another. Figure 3.14 shows the top and side view of a microstrip, folded, open-loop resonator.

Figure 3.15 shows some coupling structures arising from different orientations of a pair of the proposed resonators and the associated coupling type. If the edges with the gap are coupled, it results in electric (capacitive) coupling, because the electric fields are maximum along these edges. If the edges opposite to the aforesaid edges are coupled, then magnetic

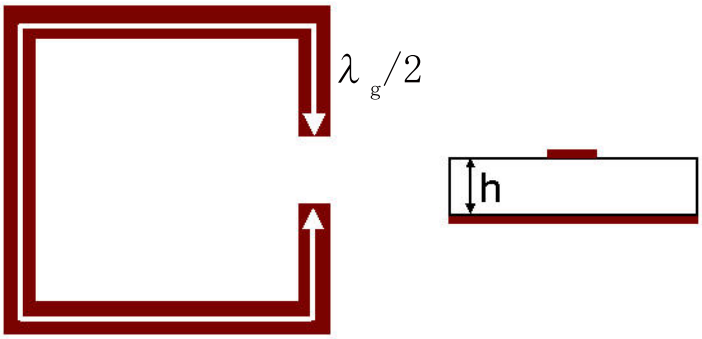

Figure 3.14: Top and side view of a microstrip, folded, open-loop resonator

(inductive) coupling can be achieved. The type of coupling is predetermined in these two configurations, independent of the substrate characteristics. Coupling along the other two edges typically results in a mixed coupling. The type of coupling in these cases is determined based on the strength of electric and magnetic fields along these edges. A mixed coupling can result either in a dominant electric coupling or in a dominant magnetic coupling depending on the physical characteristics of the substrate (such as 'h') and of the resonators (such as 's').

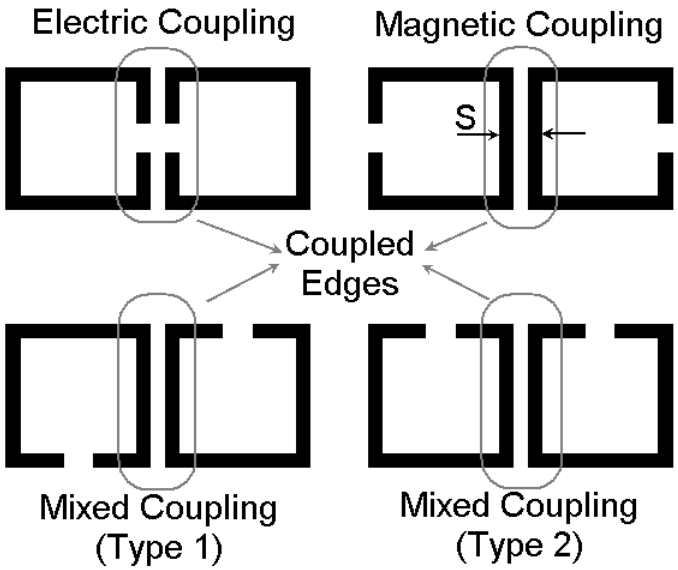

Figure 3.15: Different coupling mechanisms with the folded open-loop resonator.

Figure 3.16 shows the filter configuration, composed of these resonators, with appropriate couplings required to realize the coupling coefficients summarized in Table 3.8. The sign used for a particular type of coupling is relative and can be interchanged. In this case, the negative coupling is realized using an electric coupling configuration while the positive couplings are realized using magnetic and mixed coupling (type 1) configurations.

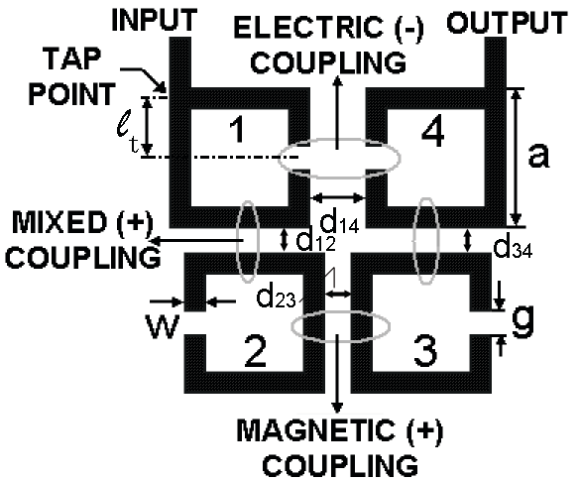

Figure 3.16: Filter configuration to implement the topology in Figure 3.10.

Formulations to establish the relationship between coupling coefficients and the physical structure of coupled resonators can be found in [43].

For synchronously coupled resonators, the coupling coefficient is given by

$$K = \frac{f_1^2 - f_2^2}{f_1^2 + f_2^2} \tag{3.3}$$

where 'K' is the value of the coupling coefficient, and 'f_1' and 'f_2' are the two split frequencies that can be obtained from numerical simulations for a given coupling configuration of a pair of coupled resonators.

For asynchronously coupled resonators, the coupling coefficient is given by

$$K = \frac{1}{2}\left(\frac{f_{02}}{f_{01}} + \frac{f_{01}}{f_{02}}\right)\sqrt{\left(\frac{f_2^2 - f_1^2}{f_2^2 + f_1^2}\right)^2 + \left(\frac{f_{02}^2 - f_{01}^2}{f_{02}^2 + f_{01}^2}\right)^2} \tag{3.4}$$

where 'K' is the value of the coupling coefficient, 'f_{01}' and 'f_{02}' are self-resonant frequencies of the two coupled resonators, and 'f_1' and 'f_2' are the two split frequencies.

Tapped inputs and outputs were used as opposed to parallel coupling at end sections. The relationship between the external quality factor and the tapping location is given by [102]

$$Q_e = \frac{R}{Z_0} \frac{\pi}{2sin^2(\frac{\pi l_t}{2L})} \tag{3.5}$$

where 'R' is the reference impedance, 'Z_0' is the filter internal impedance, 'L' is half the length of each resonator and 'l_t' relates to the tapping location and is defined as shown in Figure 3.16. A general formula for calculating the external quality factor irrespective of the resonator type is also available:

$$Q_e = \frac{f_0}{\triangle f_{\pm 90^\circ}} \tag{3.6}$$

where 'f_0' is the resonant frequency of the resonator and '$\triangle f_{\pm 90^\circ}$' represent the frequencies at which the reflection phase shift of a singly loaded resonator differs by $\pm 90^\circ$ with respect to the absolute phase at f_0.

Numerical simulations along with the relationships provided by the above mentioned equations were used to generate appropriate design curves. These design curves were used to determine the physical parameters of the filter circuit shown in Figure 3.16. ADS-Momentum [7], a 2.5-D MOM solver, was used to perform the necessary simulations.

The LCP substrate chosen for the design and fabrication of the filter prototypes is characterized by $\epsilon_r = 2.95 - 3.15$ (across the range of design frequencies), $tan\delta = 0.002 - 0.004$, a conductor thickness of 18 μm, and a substrate thickness of 203 μm (X-band, Ka-band) and 152 μm (V-band). Table 3.9 shows the physical dimensions of the filters in μm, determined from numerical simulations.

Table 3.9: Physical dimensions of the single-layer band-pass filter prototypes.

Prototype	**a**	**w**	**g**	$\mathbf{d_{12}}$ & $\mathbf{d_{34}}$	$\mathbf{d_{23}}$	$\mathbf{d_{14}}$	$\mathbf{l_t}$
X-band	2840	230	440	165	220	400	1305
Ka-band	1045	230	255	155	156	320	523
V-band [a]	538	90	90	90	98	218	358

[a] The reference impedance for this prototype is 100 Ω

Although the filter configuration in Figure 3.16 is particularly suitable for a symmetric filter, simulated results showed an asymmetric characteristic with different cut-off slopes on either side of the passband. This effect was more pronounced at high frequencies and could have resulted because of the semi-open microstrip environment. Figure 3.17 shows the same filter configuration with the possibility of small unwanted parasitic couplings between resonators 1 & 3 and resonators 2 & 4. Based on numerical simulations, we conceived that the response characteristics in the vicinity of the passband edges can be modified by changing the input and output tapping locations. From Figure 3.17 and equation (3.5), it is clear that there are two symmetric tap locations corresponding to a particular external quality factor (Q_e) and it was found that by using different combinations of input and output tap locations, the skirt properties on either side of the passband can be altered. Figure 3.18 shows the resonators with different tap combinations available with the proposed filter configuration.

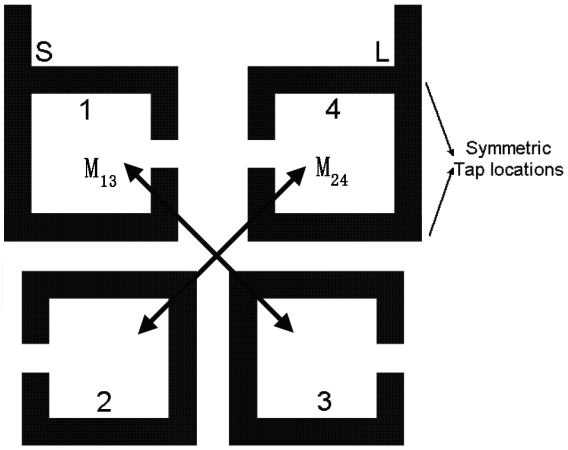

Figure 3.17: Filter configuration showing the parasitic couplings and symmetric tap locations.

The X-band filter was designed with the tap combination 'a' and 'd', the Ka-band filter with the combination 'a' and 'b', and the V-band filter with the combination 'c' and 'd'. Although the designed filter prototypes are essentially single-layer designs, bonding was required to fabricate them, because LCP is available only in discrete thickness (51 μm and 102 μm).

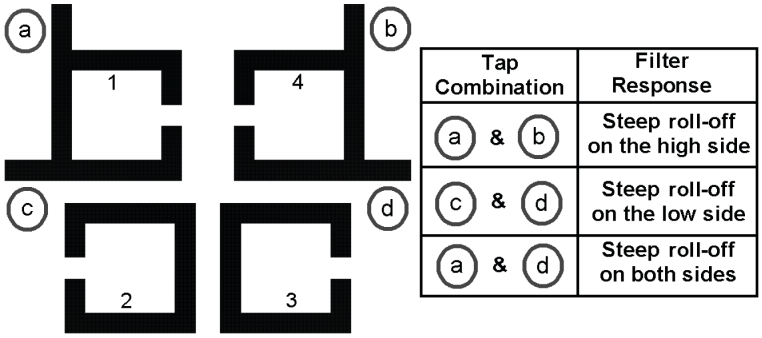

Figure 3.18: Filter configuration showing different input/output tap combinations and the corresponding effect on the skirt characteristics of the filter.

3.3.3 Experimental results

Figure 3.19a shows a photo of the fabricated filter for $f_0 = 10$ GHz. The filter layout occupies a compact area of $8.9 \times 5.9\ mm^2$. The layout has been optimized to get the strongest rejection properties at 8.3 GHz, 9.3 GHz and 10.9 GHz. The extra transmission zero is created by the input/output tap combination. Apart from resulting in a symmetric roll-off on both sides of the pass-band, the feed structure creates an additional attenuation pole because of the parallel-stub effect in this tap combination. As a result, the rejection in the low side of the passband is further enhanced.

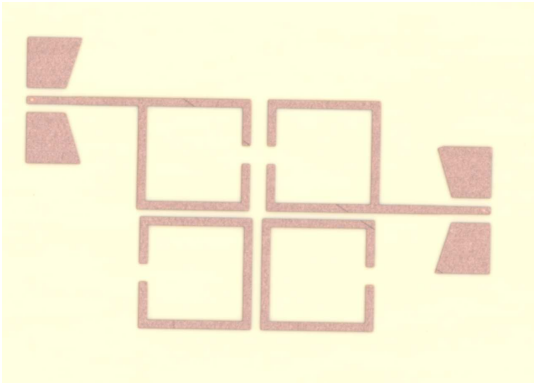

(a) Photo of the X-band filter

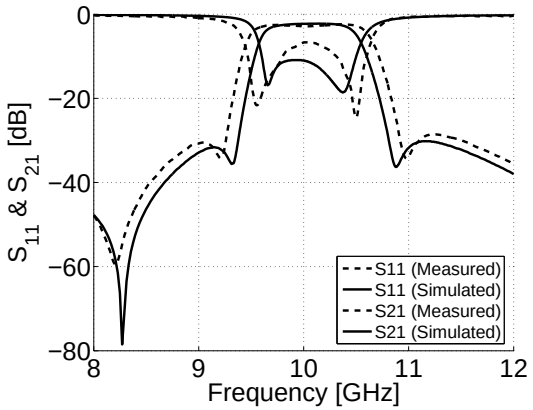

(b) Measured and simulated S-parameter results

Figure 3.19: X-band Filter.

The simulated and measured scattering parameter characteristics for the X-band filter are summarized in Table 3.10. A good agreement between the simulated and measured results can be observed. The insertion loss in the passband and the rejection levels at the

frequencies of transmission zeros are accurately predicted. A slight discrepancy exists as far as the bandwidth is concerned. This may be attributed to fabrication tolerances. Because of the discrepancy in the bandwidth, the measured location of the transmission zeros are also different from those of the predicted ones.

Table 3.10: Simulated and measured S-parameter characteristics of the X-band prototype.

Attribute	**f_0 GHz**	**-3 dB BW GHz**	**IL dB**	**f_{z1} GHz**	**Rejection at f_{z1} dB**	**f_{z2} GHz**	**Rejection at f_{z2} dB**
Simulated	10	0.91	2.25	9.33	35.4	10.88	36.3
Measured	**10**	**1.15**	**2.45**	**9.2**	**34.2**	**10.98**	**34.3**

Figure 3.20a shows a photo of the fabricated filter for $f_0 = 35$ GHz. The filter layout occupies a compact area of 2.4×2.4 mm^2. The layout has been optimized to get the strongest rejection properties at 31.6 GHz and 37.3 GHz. The transmission zero in the high side of the passband is closer to the center frequency, when compared to the transmission zero in the low side of the passband, and this results in a steeper rejection on the high side.

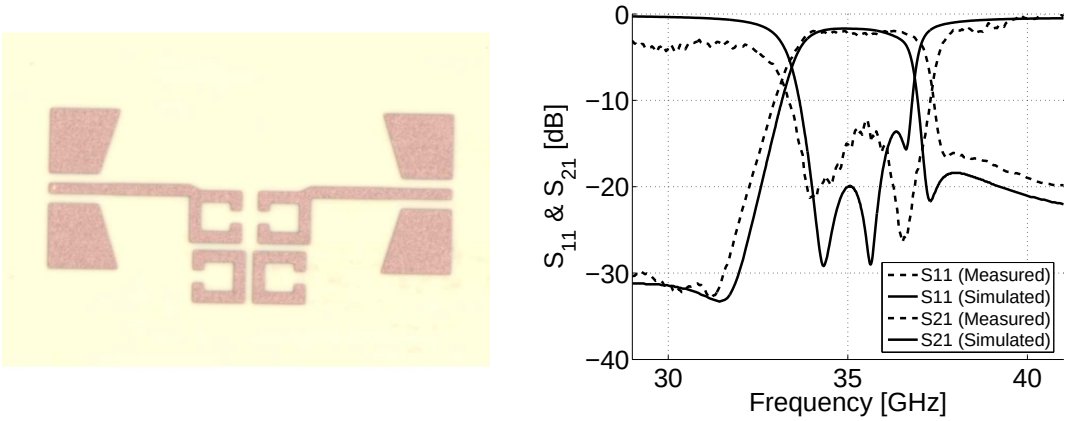

(a) Photo of the Ka-band filter

(b) Measured and simulated S-parameter results

Figure 3.20: Ka-band Filter.

Table 3.11 shows the comparison between the simulated and measured scattering parameter characteristics for the Ka-band prototype. Calibration issues resulted in the ripples that are noticeable in the measurements. Despite this, the performance of this prototype is satisfactory and the measured characteristics agree well with the simulated ones. A low insertion loss of 2.1 dB has been measured at 34.92 GHz.

Figure 3.21a shows a photo of the fabricated filter for $f_0 = 61.5$ GHz. The filter layout

Table 3.11: Simulated and measured S-parameter characteristics of the Ka-band prototype.

Attribute	f_0 GHz	-3 dB BW GHz	IL dB	f_{z1} GHz	Rejection at f_{z1} dB	f_{z2} GHz	Rejection at f_{z2} dB
Simulated	35.1	3.15	1.71	31.6	33.1	37.3	21.7
Measured	**35.2**	**3.65**	**2.1**	**31.2**	**32.9**	**37.7**	**16.7**

occupies a compact area of $1.4 \times 1.2\ mm^2$. The layout has been optimized to get the strongest rejection properties at 56 GHz and 72 GHz. In this case, the transmission zero in the low side of the passband is closer to the center frequency, when compared to the transmission zero in the high side of the passband, and this results in a steeper rejection on the low side. Thus, although all the filters share the same coupling topology, different tap combinations together with the semi-open environment of the microstrip resonators can result in different skirt properties around the passband edges.

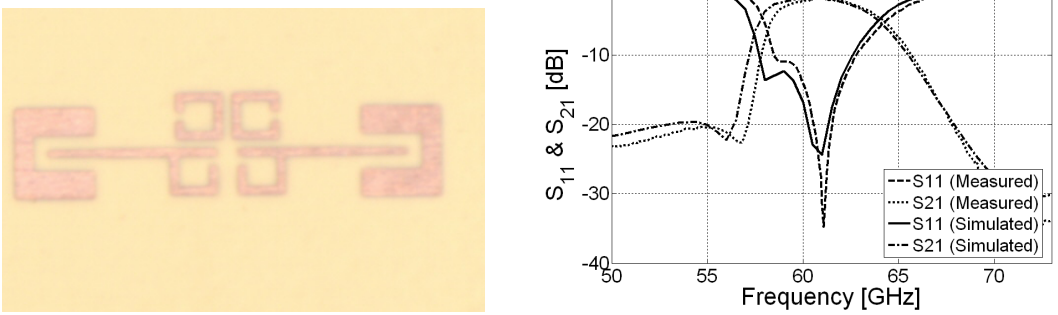

(a) Photo of the V-band filter

(b) Measured and simulated S-parameter results

Figure 3.21: V-band Filter.

The simulated and measured scattering parameter characteristics for the V-band filter are summarized in Table 3.12. A very low insertion loss of 1.96 dB has been measured at 60.9 GHz.

Table 3.12: Simulated and measured S-parameter characteristics of the V-band prototype.

Attribute	f_0 GHz	-3 dB BW GHz	IL dB	f_{z1} GHz	Rejection at f_{z1} dB	f_{z2} GHz	Rejection at f_{z2} dB
Simulated	61	5.8	1.84	56	22.2	72	-31
Measured	**61.4**	**5.5**	**1.96**	**56.8**	**22.6**	**72**	**-35**

The performance of these prototype filters confirm the excellent electrical characteristics of LCP across a wide range of frequencies from X-band to V-band. The reported

measurements also validate the synthesis and design techniques outlined in Section 3.3.2. In addition, reasonable compactness has been achieved in spite of the low dielectric constant of the substrate. Further size reductions are possible, if a multilayer implementation is considered. The development of such filters utilizing the multilayer lamination capabilities of LCP are presented in Chapter 4.

3.3.4 Unloaded quality factor calculations

Thus far, we have observed slight discrepancies between the simulated and measured results for both the developed antenna arrays and filters. Many factors may have contributed to these discrepancies and depending on a particular implementation, one factor may dominate the others. For example, fabrication errors may be the dominant factor for designs that employ multilayer architectures. Other factors include material tolerances, modeling errors and/or measurement inaccuracies. These inaccuracies may contribute to discrepancies in the resonant frequency, may lead to degradation of the insertion loss or may alter the bandwidth of a device.

The bandwidth and the insertion loss of a filter are related to the unloaded quality factor (Q_u) of the filter resonators. Hence, in order to understand the discrepancies in the filter implementations, Q_u was calculated based on both simulations and measurements of input return loss of a singly loaded open-loop resonator.

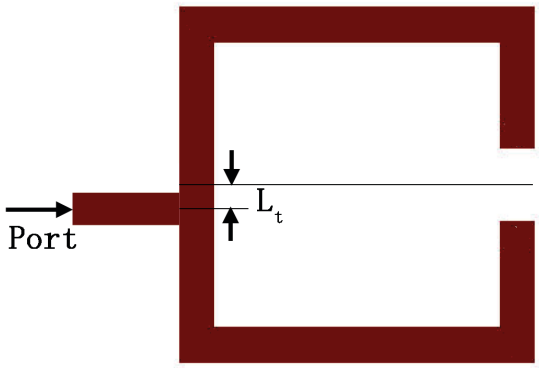

Figure 3.22: Setup to calculate the Q_u of a folded open-loop resonator based on return loss simulations and measurements.

The one-port reflection technique outlined in [59] was used for Q_u calculations. Figure 3.22 shows the arrangement employed for the calculation of Q_u of a folded open-loop resonator. The feed arrangement is identical to the one used in the input and output of the prototype filters. In the filter designs, the tapping position (related to 'L_t' in Figure 3.22) was adjusted to achieve specific input/output coupling. Here, we used a tapping position that will result in a very low coupling (or a high loaded quality factor (Q_L)) so that the feeding arrangement will not have an impact on the measurements and the subsequent calculations. The equations [59] employed for the calculation of Q_u are:

$$RL_0 = -20 \log \left| \frac{1-\beta}{1+\beta} \right| \tag{3.7}$$

$$F(x,\beta) = \sqrt{\frac{(1+\beta)^2 |\rho|_x^2 - (1-\beta)^2}{1-|\rho|_x^2}} \tag{3.8}$$

$$x = -20 \log |\rho_x| \tag{3.9}$$

$$Q_L(x,\beta) = \frac{\omega_0}{(\Delta\omega)_x} \tag{3.10}$$

$$Q_u = Q_L(x,\beta) F(x,\beta) \tag{3.11}$$

In the above equations, 'RL_0' is the return loss in dB at the resonant frequency, 'β' is the coupling parameter, 'Q_L' is the loaded quality factor, which is a function of 'x' and 'β', 'ω_0' is the angular resonant frequency, '$(\Delta\omega)_x$' is the bandwidth measured at the -x dB points of the input return loss, and 'Q_u' is the unloaded quality factor of the resonator, which, in principle, is independent of 'x' and 'β'.

Figure 3.23 shows a plot of the simulated and measured input return loss of a X-band folded open-loop resonator. Table 3.13 and 3.14 summarizes the results for the X-band folded open-loop resonator tested for a fixed value of β. The value of β is controlled by the tapping position (related to 'L_t').

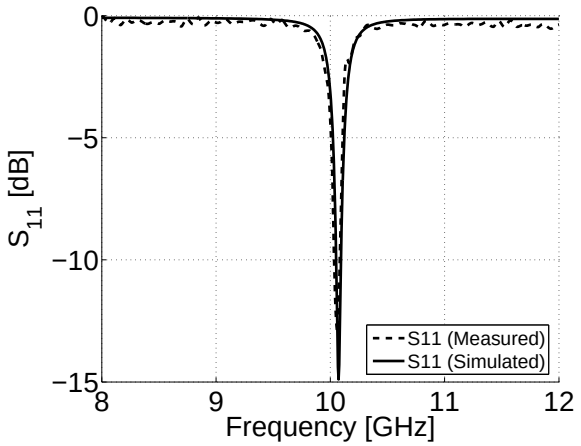

Figure 3.23: Simulated and measured input return loss of a X-band folded open-loop resonator.

Table 3.13: Q_u calculations for the X-band folded open-loop resonator based on simulations with $f_0 = 10.07\ GHz$ and $\beta = 0.6951$.

$\mathbf{x}$	$(\mathbf{\Delta f})_{\mathbf{x}}$	$\mathbf{Q_L}(\mathbf{x}, \beta)$	$\rho_{\mathbf{x}}$	$\mathbf{F}(\mathbf{x}, \beta)$	$\mathbf{Q_u}$
1	0.314	32.07	0.89	2.93	93.96
2	0.197	51.12	0.79	1.87	95.79
3	0.155	64.97	0.71	1.36	88.38

Table 3.14: Q_u calculations for the X-band folded open-loop resonator based on measurements with $f_0 = 10.07\ GHz$ and $\beta = 0.6321$.

$\mathbf{x}$	$(\mathbf{\Delta f})_{\mathbf{x}}$	$\mathbf{Q_L}(\mathbf{x}, \beta)$	$\rho_{\mathbf{x}}$	$\mathbf{F}(\mathbf{x}, \beta)$	$\mathbf{Q_u}$
1	0.33	30.52	0.89	2.71	82.83
2	0.197	51.12	0.79	1.71	87.45
3	0.139	72.44	0.71	1.21	87.91

For the X-band case, the Q_u values calculated based on both simulated and measured results remain fairly constant for different values of 'x'. The Q_u calculated from measured Q_L is lower compared to the simulated Q_u, although a reasonable agreement has been achieved. Compared to the filter implementations, we may contend that simulation/modeling error may be the dominant factor here, because the resonator circuit proposed to measure the Q_L did not require any accurate gap to be fabricated. As a result, fabrication errors can be expected to be minimal and the discrepancies in evidence could have resulted mainly from inaccurate modeling of different loss mechanisms during simulations. In a microstrip circuit, there are three sources of losses:

- Conductor losses
- Dielectric losses
- Radiation losses

The dielectric losses were modeled by the loss tangent of the substrate. The loss tangent values reported in [95] were used. The MOM solver [7] employed for devices reported in this section uses an in-built model to calculate the radiation losses. The conductor losses were modeled by the metal conductivity. It is known that the metal's surface roughness and quality will affect the quality factor associated with the conductor losses [41]. The simulator did not have any provision of modeling this surface roughness. The surface roughness of copper in the double-clad LCP sheets available from Rogers corporate is measured to be between 0.4 and 0.6 μm. The upper limit of 0.6 μm corresponds to one skin depth at 12 GHz. As a result, one can expect to measure more conductor losses than the simulated results for frequencies nearing and above 12 GHz, which will introduce discrepancies between measured and simulated Q_u.

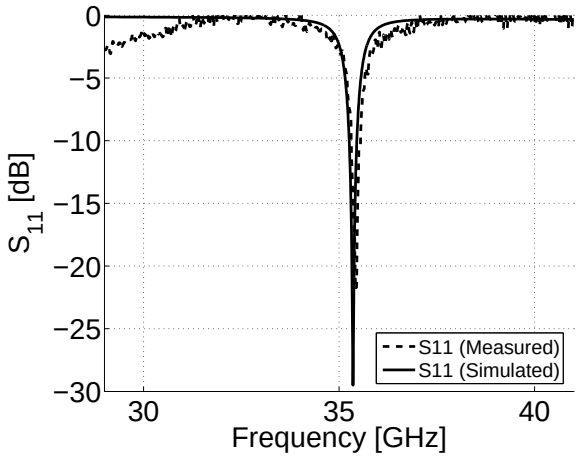

Figure 3.24: Simulated and measured input return loss of a Ka-band folded open-loop resonator.

Figure 3.24 shows a plot of the measured input return loss of a Ka-band folded open-loop resonator. Table 3.16 summarizes the results for the Ka-band folded open-loop resonator tested for a fixed value of β.

Table 3.15: Q_u calculations for the Ka-band folded open-loop resonator based on simulations with $f_0 = 35.35\ GHz$ and $\beta = 0.9361$.

$\mathbf{x}$	$(\mathbf{\Delta f})_{\mathbf{x}}$	$\mathbf{Q_L}(\mathbf{x}, \beta)$	$\rho_{\mathbf{x}}$	$\mathbf{F}(\mathbf{x}, \beta)$	$\mathbf{Q_u}$
3	0.6	58.92	0.71	1.875	110.51
5	0.4	88.38	0.56	1.246	110.12

Table 3.16: Q_u calculations for the Ka-band folded open-loop resonator based on measurements with $f_0 = 35.44\ GHz$ and $\beta = 0.8485$.

$\mathbf{x}$	$(\mathbf{\Delta f})_{\mathbf{x}}$	$\mathbf{Q_L}(\mathbf{x}, \beta)$	$\rho_{\mathbf{x}}$	$\mathbf{F}(\mathbf{x}, \beta)$	$\mathbf{Q_u}$
3	0.7	50.63	0.71	1.69	85.80
5	0.45	78.76	0.56	1.08	85.22

For the Ka-band case also, Q_u values calculated based on both simulated and measured results remain fairly constant for different values of 'x'. Again, discrepancies exist between the measured Q_u and the simulated Q_u. The disparity in the Ka-band case is bigger compared to the disparity in the X-band case. This result further confirms our speculations about incorrect modeling of conductor losses, because the surface roughness effects become more pronounced as we go higher in frequency.

The resonator chosen is only a representative element and a different resonator might have a different Q_u. It must be mentioned here that higher Q_u values might be realized even without modifying the resonator. The key is to identify the optimal substrate thickness, which will vary with frequency. A thick substrate will have a lower conductor loss while a thin substrate will have a lower radiation loss.

3.4 Chapter summary

This chapter focused on the development of compact low-pass and band-pass filters on single-layer LCP technology. Filter prototypes operating in a wide range of frequencies have been developed to understand the electrical performance of LCP in those frequency ranges. Pseudo-elliptic filters with sharp attenuation response have been explored to meet the stringent requirements of the modern communication systems.

The design methodology of the low-pass filters starting from the calculation of lumped

element values to the transformation of these components into microstrip circuits was described. Excellent measurement results and a compact size have been achieved for prototypes operating from C-band to V-band. The sharp roll-off characteristics of these filters in the attenuation band give insight about the quality factor of the resonators realized on LCP.

Band-pass filters operating in the X-band, Ka-band, and V-band have been designed, fabricated, and measured. These filters were designed based on the theory of coupled resonators. A simple method to alter the skirt properties of these filters based on the feeding arrangement has been presented. Q_u calculations were made based on both simulations and measurements. To our best knowledge, this was the first report on the measurement of quality factor of resonators realized on LCP.

Overall, this work demonstrates the potential of LCP to function as a low-cost solution for excellent performance and ultra-compact RF, microwave and millimeter-wave planar low-pass and band-pass filter designs.

CHAPTER IV

MULTILAYER MICROSTRIP BAND-PASS FILTERS

In Chapter 3, the focus was on designing and implementing compact filters on single-layer LCP technology. Synthesis and design techniques were provided together with measurements of prototypes operating in a wide range of frequencies. In this chapter, we extend those development principles to realize multilayer filters. Modern wireless systems demand light-weight, miniaturized, low-cost solutions besides requiring excellent electrical performance and reliability. Filters, which are integral components of such systems, should not only be designed to meet these stringent requirements but also should provide flexibility for integration with other components, circuits and subsystems. For these reasons, there has been increasing interest in the design and implementation of multilayer filters. The design flexibility is greatly increased by allowing placement of filter elements on more than a single layer. Multilayer filter structures can be broadly divided into two categories. In the first category, the filter is composed of resonators that are located at different layers without any ground plane inserted between the adjacent layers [87, 75, 31]. The single ground plane in these filters is usually at the bottom of the multilayer stack-up. In the second category, there can be multiple ground layers [45, 105, 29]. The resonator layers and ground layers are interspersed and coupling between resonators on different layers is achieved through slots in the ground plane. Figure 4.1 shows an illustration of the said multilayer filter categories. The filters developed in this work belong to the second category. Two filter prototypes have been developed - one achieving a modular fully canonical response and the other utilizing dual-mode resonators. These particular choices were made to demonstrate the advantages of multilayer implementations for filtering applications in reducing the size and in improving the design flexibility.

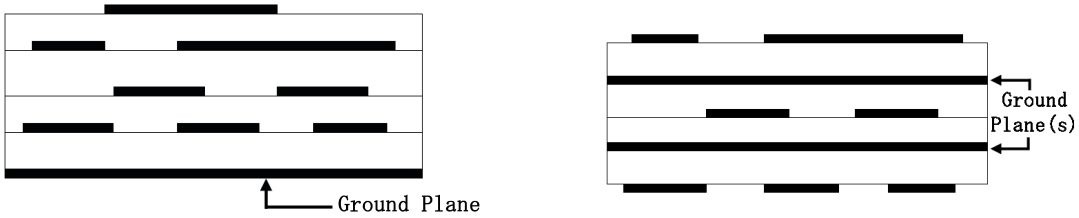

(a) Single ground layer at the bottom of the stack-up.

(b) Interspersed ground and resonator layers.

Figure 4.1: Typical multilayer filter structures.

4.1 Modular filters using non-resonant nodes

In this section, the design and implementation of a fully canonical pseudo-elliptic band-pass filter on multilayer LCP technology is presented. Folded open-loop resonators described in Secion 3.3.2 are employed in this filter. In the previous approaches, open-loop resonators with only one type of coupling have been considered. Those approaches used slots in the ground plane to achieve coupling only between resonating nodes. The multilayer design discussed here includes coupling between both resonating and non-resonating nodes, so that fully canonical filtering can be achieved. A fully canonical filter [13] is capable of realizing 'N' finite frequency transmission zeros for an Nth order filter. This, in turn, helps to achieve a high level of rejection over a wider stop band. Either direct source-load coupling or coupling through internal NRNs [12] is required to achieve maximum finite frequency transmission zeros for a given filter order. In this work, internal NRNs are utilized to make the filter modular. A modular filter is less sensitive to manufacturing tolerances and can compensate for fabrication errors associated with a multilayer implementation. To the author's knowledge, this is the first multilayer implementation of fully canonical modular filters on organic LCP technology.

4.1.1 Modular coupling scheme

The coupling scheme employed to realize the fourth order filter is shown in Figure 4.2. The filter is realized by cascading two 2-pole filters (S-1-2-X and Y-3-4-L), each contributing a pair of transmission zeros. The multilayer filter configuration, proposed to implement this

scheme, consists of stacked dielectric substrates with ground plane sandwiched between the layers and resonators printed on outer surfaces.

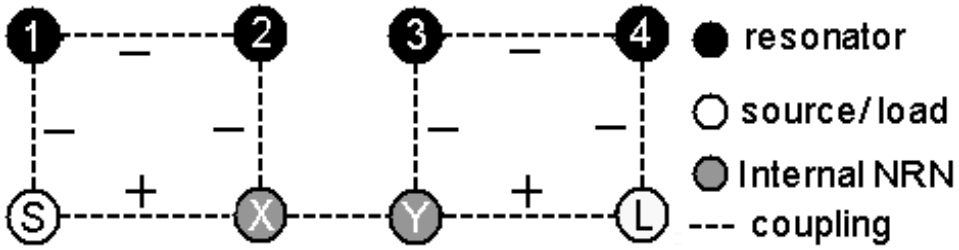

Figure 4.2: Coupling scheme of the four-pole modular filter.

4.1.2 Multilayer design

To illustrate this approach, a filter was designed to operate in the X-Band with a center frequency of 10 GHz, a fractional bandwidth of 5% and a stop band rejection better than 30 dB. Figure 4.11 shows the geometric configuration of the proposed multilayer filter. The configuration consists of two LCP substrates ($\epsilon_r = 3.1$, $\tan\delta = 0.003$), each 102 μm thick, stacked together. Resonators 1 & 4 and source & load nodes are printed on the top surface. Resonators 2 & 3, internal NRNs 'X' & 'Y' and a transmission line connecting the NRNs are printed on the bottom surface. Four slots are etched in the ground plane that is sandwiched between the two layers. These slots provide the necessary coupling and are named with reference to the coupling scheme shown in Figure 4.2. Slots S[1,2] and S[3,4] are etched so that the corresponding resonators are coupled along their open edges. The electric fields are maximum along these edges and this results in the negative coupling desired between these resonators. Couplings S-1, 2-X, Y-3 and 4-L are realized by tapping the resonators. Slots S[S,X] and S[L,Y] provide the cross-coupling between non-resonating nodes. Vialess CB-CPW–microstrip transitions, printed on the top layer, were used to facilitate measurements using coplanar waveguide (CPW) probes.

The synthesis technique employed here is slightly different from the ones detailed in Section 3.3.2, because of the fully canonical feature of the filters considered in this section. The algorithm should take into account the possibility of direct source-load coupling or multiple

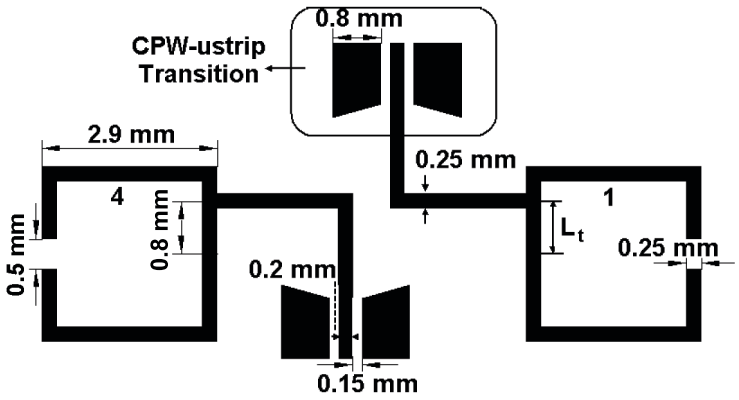

(a) Top Surface

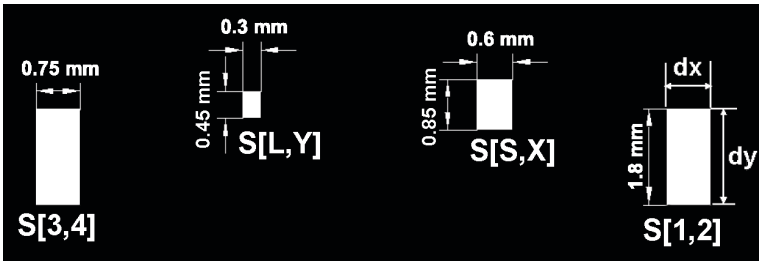

(b) Slotted Ground

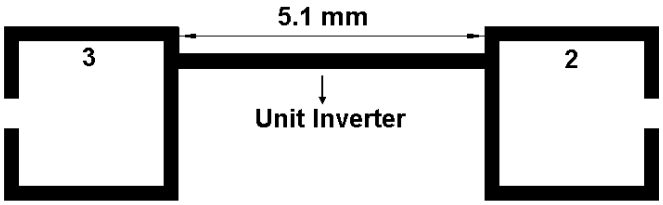

(c) Bottom Surface

Figure 4.3: Layout of the designed four-pole multilayer filter.

couplings between the source/load nodes and the resonating nodes. The algorithms described in [13, 25] are employed here. The 2-pole filters were designed individually and were then cascaded to realize the 4-pole filter. The filtering section (S-1-2-X) creates transmission zeros at 9.2 and 10.7 GHz, whereas section (Y-3-4-L) creates zeros at 8.4 and 12 GHz. Table 4.1 shows the synthesized coupling matrix elements for the two filters. Couplings S-1, 2-X, Y-3 and 4-L are characterized by Q_e.

Once the elements of the coupling matrix were obtained, the tapping location and the

Table 4.1: Elements of the coupling matrix.

M(1,2) & M(3,4)	-0.083
M(S,X)	0.008
M(L,Y)	0.002
Q_e	16.24

size of the coupling slots were determined using numerical simulations to achieve the necessary external quality factor and the coupling coefficients. ADS-Momentum [7] was used to conduct these simulations. The methodology to extract external quality factor from the frequency response of singly loaded resonators and to determine coupling coefficients from the characteristic frequencies of coupled resonators were already presented in Section 3.3.2. Design curves obtained using simulations are provided in Figure 4.4 and Figure 4.5 for quick reference. From the figures, it is clear that the external quality factor decreases when the tapping location is moved away from the center of the resonator and the coupling coefficient increases when the slot size is increased. Once the tapping location and the dimensions of the slots that couple the resonators were obtained, the dimensions of the slots, which couple the non-resonating nodes, were optimized to control the location of transmission zeros. In fact, the only difference between the two filter sections is the size of the slots (S[S,X] & S[L,Y]) that couple the non-resonating nodes.

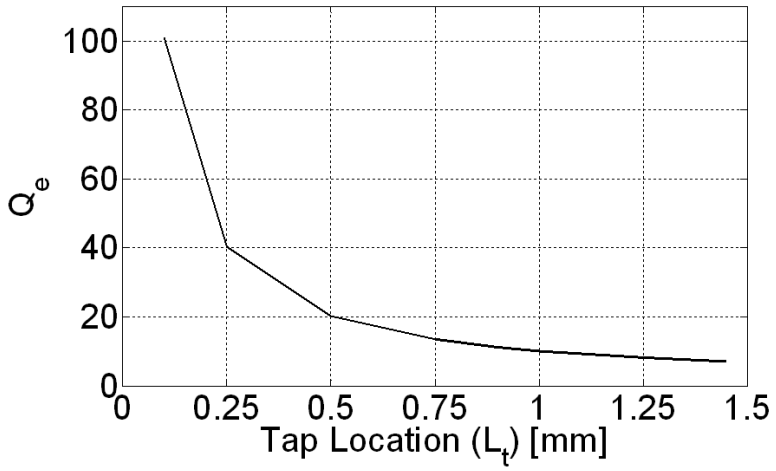

Figure 4.4: External quality factor as a function of tapping location.

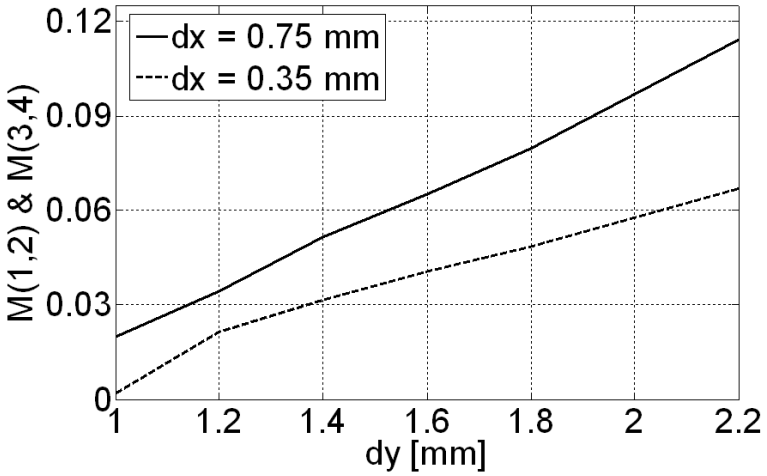

Figure 4.5: Coupling coefficient as a function of slot size.

The susceptance of the internal NRNs and the coupling between them can be adjusted, when implementing the fourth order filter. Many solutions are possible. In this work, we used the simplest solution, wherein the susceptances are made zero and a unit inverter is used as a link. A quarter wave transformer was used to implement this unit inverter.

4.1.3 Fabrication and measurements

The fabrication procedure is similar to the one described in Section 2.3.2. The resonators and feeding lines, shown in Figure 4.3a were printed on one side of a 51 μm core LCP layer while the other side is left bare. The slotted ground was printed on one side of a 102 μm core LCP layer and the rest of the filter circuit was printed on the back side of the same layer. These two core layers were then bonded together using a 51 μm bond LCP layer resulting in the final multilayer architecture. Throughout the fabrication process, alignment between different layers was maintained using laser-drilled alignment holes.

Figure 4.6 shows the setup used to measure the multilayer filter fabricated on LCP. The simulated and measured scattering parameters of the fully canonical filter with all four transmission zeros is shown in Figure 4.7a. A very good agreement is achieved between simulations and measurements. The measured filter exhibits a low insertion loss of 3.2 dB at 9.9 GHz. The loss is mainly due to the conductor loss. To show the modular characteristics of the proposed design, additional filters without some coupling slots were fabricated and

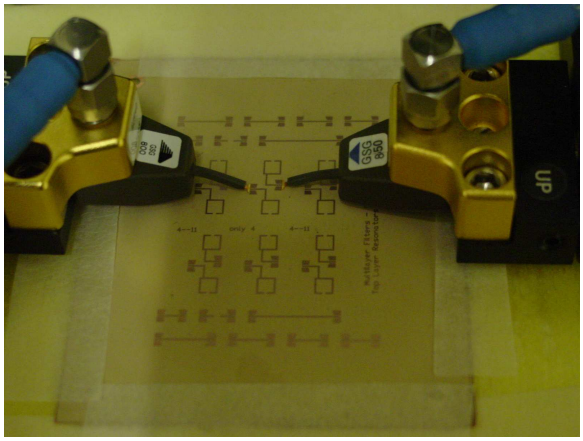

Figure 4.6: Measurement setup showing the fabricated multilayer filters (Only the top layer is visible)

measured. Figure 4.7b shows the filter response when slot S[L,Y] is absent and Figure 4.7c shows the response when slot S[S,X] is absent. In both cases, the corresponding transmission zeros disappear without significantly degrading other characteristics of the filter. This clearly shows that the creation of respective transmission zeros is controlled independently by the two filtering sections. The overall size of the filter is 10.9 X 2.9 mm^2. Although the introduction of NRNs made the filter less compact, the multilayer realization still offers size reduction over a 2-D implementation.

4.2 Filters using dual-mode resonators

In this section, we present a multilayer filter design that involves dual mode slotted patch resonators implemented on LCP technology. Dual mode resonators have generated considerable interest [101] - [104] for filter applications due to their simple design and implementation characteristics. However, mostly second order filters utilizing one dual mode resonator have been presented before. Higher order filters with complex cross coupling schemes often require NRNs to couple adjacent dual mode resonators [33]. A multilayer implementation will alleviate the need for such NRNs and can also increase compactness. Slotted patch resonators have been chosen in this work, because of their small size and high Q characteristics [108]. Two different resonator arrangements, implementing the same coupling scheme, showing different out-of-band characteristics are presented. To the author's

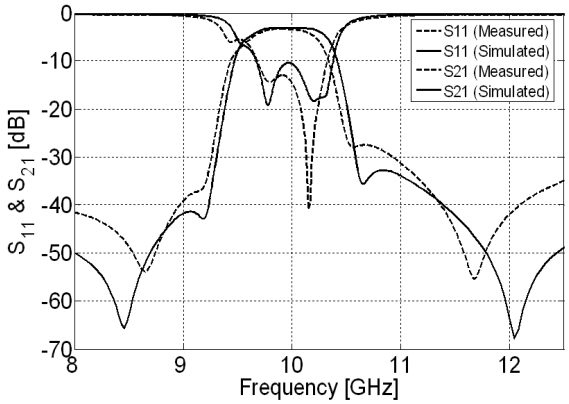

(a) Fully canonical response

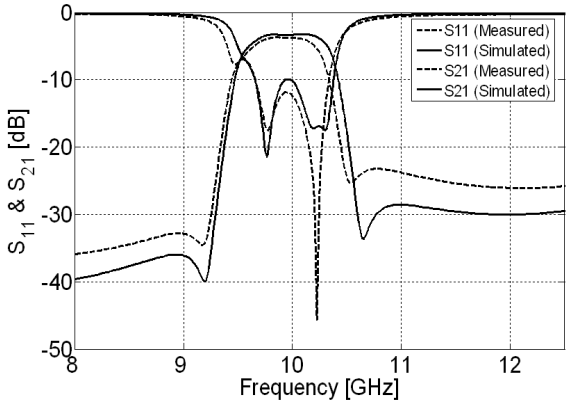

(b) Response when M(L,Y) is made zero

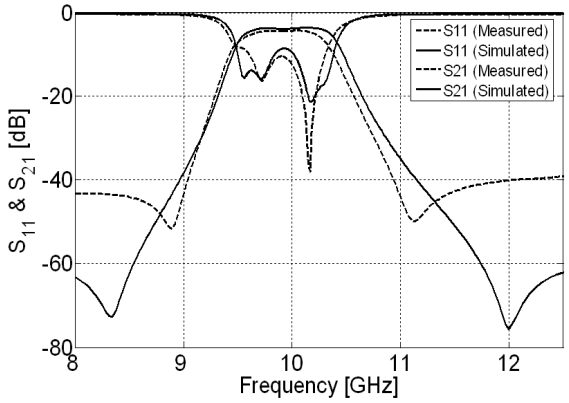

(c) Response when M(S,X) is made zero

Figure 4.7: Simulated and measured S-parameters of the four-pole modular filter.

knowledge, this is the first multilayer implementation, utilizing dual mode resonators, on an organic technology.

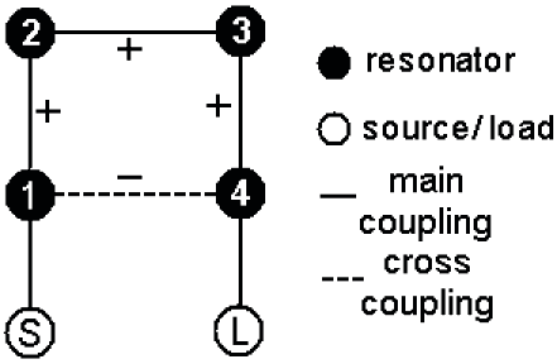

Figure 4.8: Coupling scheme for the proposed four-pole filter that uses dual-mode resonators.

4.2.1 Coupling scheme and coupling matrix

Figure 4.8 shows the coupling scheme used to realize the quasi-elliptic filters presented in this section. Filter prototypes were designed to operate in the X-band with a center frequency of 10 GHz, a frequency bandwidth of 6%, a return loss level of 20 dB and a steep out-of-band rejection achieved with the help of two finite frequency transmission zeros at 9.4 GHz and 10.6 GHz. The coupling matrix and the external quality factor satisfying these specifications are provided in (4.1).

$$M = \begin{bmatrix} 0 & 0.0511 & 0 & -0.0141 \\ 0.0511 & 0 & 0.0435 & 0 \\ 0 & 0.0435 & 0 & 0.0511 \\ -0.0141 & 0 & 0.0511 & 0 \end{bmatrix} \quad Q_e = 16.02 \tag{4.1}$$

These were determined using the synthesis technique outlined in Section 3.3.2.

4.2.2 Slotted patch resonator

Many resonator choices are available for a microstrip implementation of the synthesized coupling matrix. Folded half wavelength open-loop resonators are popular for their compact size and flexibility. Dual mode resonators that combine two resonators into a single physical structure can also be used. Perturbations along the symmetry plane are normally introduced to couple the two orthogonal modes of such a resonator. Within dual mode resonators, several disc and ring based resonators of different shapes are possible. In this work, slotted

patch resonators proposed in [108] are utilized. These resonators provide simultaneous size and loss reduction owing to the pair of slots etched on the surface of the patch.

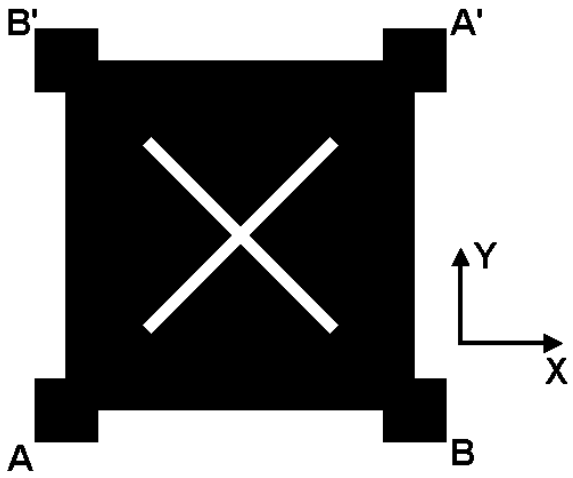

Figure 4.9: Slotted patch resonator with perturbation patches in the corners.

Figure 4.9 shows the top view of the slotted patch resonator employed in this work. A pair of slots are etched in a square patch and four small patches, which we will call "perturbation patches," are added to the corners along the planes AA' and BB'. As long as the slots are of equal length and the perturbation patches are of same size, there will be no coupling between the two orthogonal modes of the resonator. The authors in [108] did not use the perturbation patches, but proposed different slot lengths to couple the degenerate modes. In this work, we kept the slot lengths same and coupling was achieved by changing the size of all perturbation patches. The reasons behind this will be explained in the next section. Since the physical behavior of the slotted patch resonator has been described before, we focus on the multilayer configuration and the perturbation arrangement utilized to implement the proposed scheme.

4.2.3 Multilayer configuration

The proposed multilayer configuration consists of stacked dielectric substrates with a ground plane sandwiched between the layers and dual mode resonators printed on outer surfaces. It is depicted in Figure. 4.10 and Figure. 4.11. The dielectric material used is LCP ($\epsilon_r = 3.1$, $\tan\delta = 0.003$). The thickness of each dielectric layer is 100 μm. Two slots are etched

in the ground plane that is sandwiched between the two layers. These slots provide the necessary coupling between resonators on different surfaces and are named with reference to the resonant modes that are coupled. Let T_x, T_y be the two orthogonal modes associated with the dual mode resonator on the top surface and B_x, B_y be the corresponding modes on the bottom surface. Then slot S(T_x, B_x) couples modes T_x and B_x. In a single layer implementation, the dual mode resonators have to be placed side by side. Because of the physical structure of the resonator, additional non-resonating nodes and admittance inverters will be required to implement the coupling scheme shown in Figure. 4.8. In this multilayer implementation, the resonators are stacked vertically and coupling between different dual mode resonators is easily achieved with the help of coupling slots etched in the common ground plane. Filters of higher order can be realized by stacking further dielectric layers. Coupling between resonators on different surfaces occurs only through the coupling slots and the ground plane isolates the resonators otherwise. The orthogonal modes within a dual mode resonator (for example, B_x, B_y) are coupled by changing the size of perturbation patches along symmetry planes (see Figure. 4.11c).

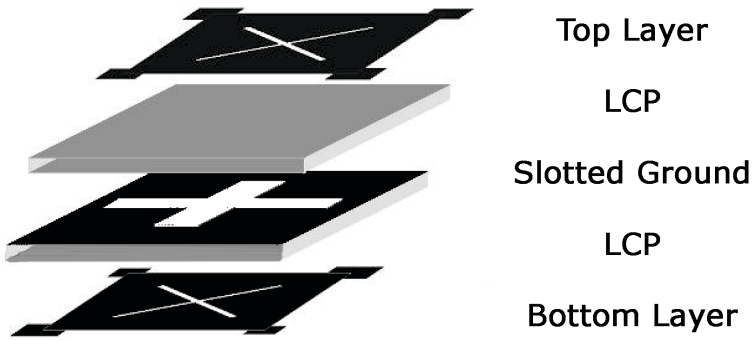

Figure 4.10: 3-D view of the proposed prototype.

Numerical simulations were performed to determine the physical parameters that will achieve the necessary external quality factor and the coupling coefficients. ADS-Momentum [7] was used to conduct these simulations. This extraction procedure is explained in Section 3.3.2.

As mentioned before, the coupling between modes within a dual-mode resonator was achieved by introducing perturbations along both planes AA' and BB'. The conventional

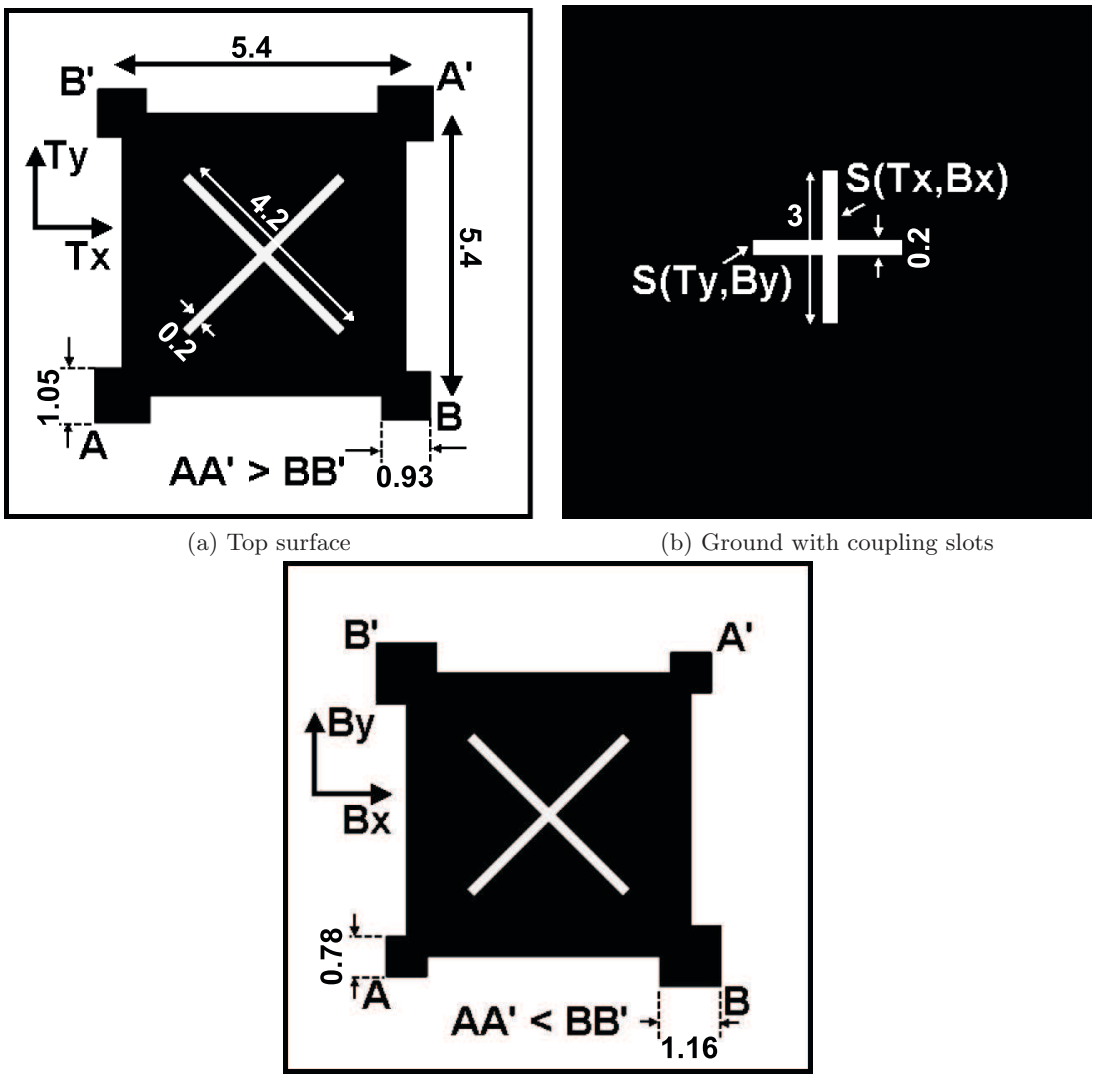

(a) Top surface

(b) Ground with coupling slots

(c) Bottom surface

Figure 4.11: Layout of the designed four-pole multilayer band pass filter. The dimensions are in mm and are for filter prototype I.

method is to introduce perturbation along one plane (typically in one corner) and the coupling mechanism is determined by the type of perturbation (decrease/ increase in patch size). Although this has been employed successfully in two-pole designs, it is not ideal for higher order filters. This is because of the mode splitting characteristics of the dual mode resonator. Let f_0 be the resonant frequency of the unperturbed dual mode resonator. Let f_1 and f_2 be the two split frequencies, when the orthogonal modes are coupled. One of the split frequencies, when perturbation is introduced in only one corner, is always f_0 and the location of the other split frequency depends on the type and amount of perturbation.

Hence, when the type of coupling is changed, the location of the split frequency changes from one side of f_0 to the other side. Figure. 4.12 shows the mode splitting characteristics. When a filter design involves many such dual mode resonators with different coupling mechanisms, it is desirable to have independent control over the split frequencies and to have the location of the split frequencies on either side of f_0, to maintain a constant center frequency for each dual mode resonator. This can be achieved by introducing perturbations along both planes. It should be noted that the perturbation arrangement for the resonator on bottom surface is different from that on top surface. This is necessary to realize coupling coefficients of different signs, required in general, to create transmission zeros at real finite frequencies.

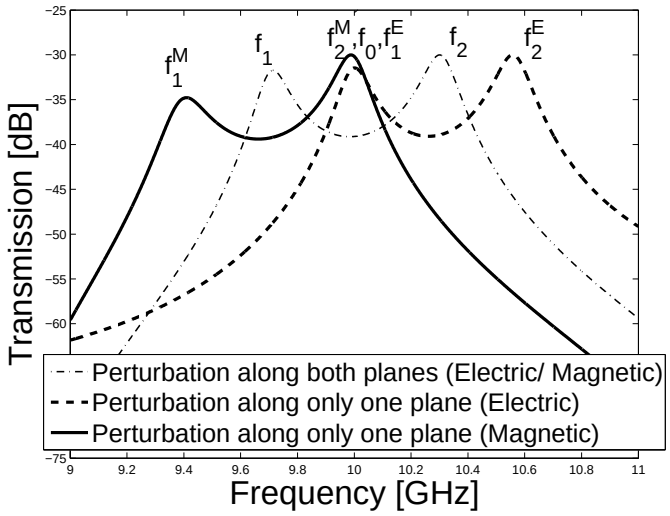

Figure 4.12: Mode splitting characteristics of a slotted patch resonator with perturbation patches.

Two filter prototypes were designed, implementing the same coupling matrix described in (1). The difference between the filters lies in the arrangement of resonators. This is detailed in Table 4.2. In filter I, the input and output ports are located at the same physical cavity (the dual mode resonator on the top surface). This presents an isolation problem as the parasitic coupling between the source and load node cannot be eliminated. Although this feature can be exploited in certain designs, it is not desired in our case (Figure 4.8), since it cannot be controlled or adjusted. In filter II, the resonators 1 and 4, to which the input and output ports are coupled, are placed on different surfaces, thereby eliminating the isolation problem.

Table 4.2: Resonator Arrangement for the prototypes.

Resonator (Fig. 4.8)	**Filter I**	**Filter II**
1	T_x	T_x
2	B_x	T_y
3	B_y	B_y
4	T_y	B_x

4.2.4 Fabrication and measurements

The fabrication procedure is identical to the one used to realize the modular filters presented in Section 4.1. Both these filters use the same multilayer configuration with identical substrate characteristics. The simulated and measured scattering parameters of the two filters are shown in Figures 4.13 and 4.14. Although both filters exhibit a steep rejection in the vicinity of the pass band edges, filter II exhibits better overall out-of-band rejection as expected. The bandwidth and location of the transmission zeros are well predicted. The measured return loss level is better than 10 dB and the measured bandwidth is 5.2% for filter I and 5.7% for filter II. The measured insertion loss is around 5 dB, while the simulated loss is 3 dB. Additional loss could have resulted from any misalignment between different layers during fabrication (changing the coupling coefficients) together with additional radiation loss. The overall size of the filter is 6.5 X 6.5 mm^2. This multilayer realization is expected to offer a better than 50% size reduction over a 2-D implementation, as the dual mode resonators have to be placed side by side with additional NRNs and coupling inverters in a uniplanar implementation. Illustration of a typical 2-D implementation of a fourth order filter that uses dual-mode resonators is shown in Figure 4.15.

4.3 Chapter summary

In this chapter, the design principles discussed in Chapter 3 were extended to develop multilayer band-pass filters on LCP technology. The development of these type of filters is critical to create compact structures on LCP, whose low dielectric constant property puts it at a disadvantage compared to LTCC and other high dielectric constant substrates.

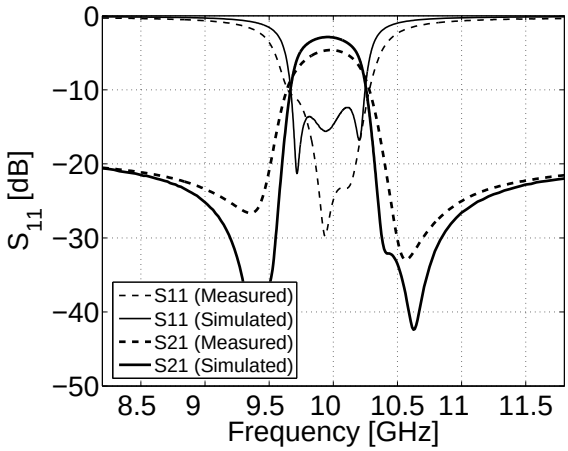

Figure 4.13: Scattering parameters of the first filter.

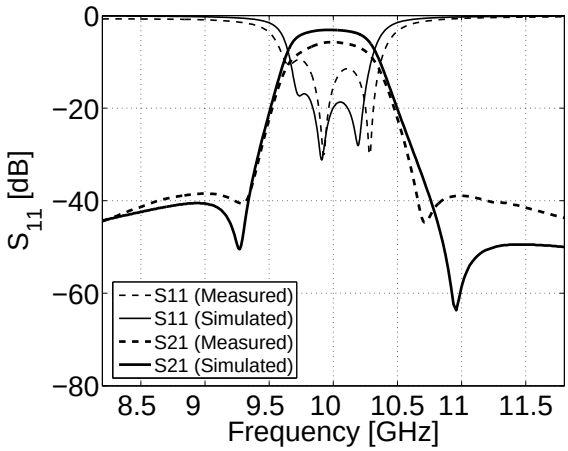

Figure 4.14: Scattering parameters of the second filter.

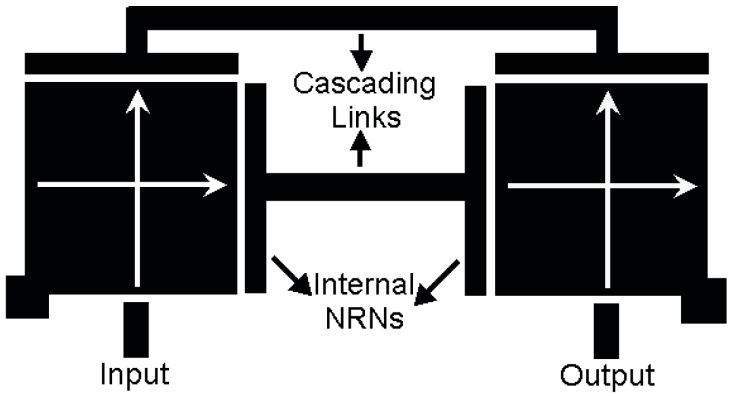

Figure 4.15: Typical uniplanar implementation of the coupling scheme in Figure 4.8.

Furthermore, the use of multilayer structures to implement filters having complex coupling topologies was also explored. Two filter prototypes, both operating in the X-band, have been developed.

The first prototype uses single-mode resonators printed on different dielectric surfaces and coupled through slots etched in a sandwiched ground plane. The use of NRNs to achieve modularity was explored. Multilayer coupling between NRNs was employed for the first time. Filters of lower order were cascaded to realize a higher order filter with modular properties. Measurements confirm the modular nature of the filter, achieved by minimizing the impact of subsections of the filter on one another.

In the second prototype, a similar mutlilayer architecture was used together with dual-mode resonaotors. Slotted patch resonators, operating in the dual-mode, have been employed to realize a fourth order multilayer filter. Two different resonator arrangements, implementing the same coupling topology, were researched. Modified perturbation arrangements were introduced to compensate for the asymmetric splitting characteristics of coupled dual-mode resonators. The devloped prototypes offer a better than 50% size reduction over a comparable single-layer implementation.

CHAPTER V

INTEGRATION OF PASSIVE CIRCUITS

In Chapter 2, we presented the development of patch antenna arrays on multilayer LCP technology for a dual-frequency/dual-polarization application. Results on two different configurations were reported. A MEMS-integrated array to achieve real-time polarization reconfigurability was also developed and characterized. Chapters 3 and 4 focused on the design and development of low-pass and band-pass filters both on single-layer and multilayer LCP technology. Synthesis and design techniques were presented, together with characterization of filter prototypes operating in frequencies ranging from C-band to V-band. In this chapter, we report on the integration of filters, matching networks, and radiating elements on LCP technology. These are the key passive components in the front-end module of a transceiver. A transceiver is a device that has two sub-devices - a transmitter and a receiver, and contains some circuit elements that are common between the transmit and receive functions. Typically, the antenna, which is the radiating element, is shared between the transmitter and the receiver. This sharing is achieved with the help of a duplexer, which also provides the necessary isolation between the transmitter and the receiver. The duplexer itself is formed by integration of a set of band-pass filters (one/more filter for each channel) and matching networks. The integration of all these individual passive elements is considered in this section of research. Specifically two integration examples, one operating in the X-band and the other operating in the V-band, are presented. The X-band system involves open-loop resonators, wide-slot antennas, and a 3-D stack-up with emphasis on compactness. The V-band system involves open-loop resonators, and patch antennas, implemented on a single-layer technology, with emphasis on electrical performance.

5.1 V-band example

5.1.1 Background

High frequencies and short wavelengths of electromagnetic energy provide several advantages for microwave applications. For instance, wider bandwidths can be realized at higher frequencies and hence higher transmission rates can be achieved in a wireless communication system. Moreover, the gain of an antenna is usually proportional to the electrical size of the antenna. Overall, high operating frequencies provide significant advantages in realizing miniaturized microwave systems. On the flip side, the complexities in the investigation, design, and implementation of high-frequency systems also increase.

The frequency band of concern, the 60 GHz V-band, is of special interest for dense, local wireless communication applications because of its specific attenuation characteristic due to atmospheric oxygen of 10-15 dB/Km. This attenuation characteristic makes the 60 GHz band unsuitable for long-range communications and, hence, it can be dedicated entirely to short-range communications. A plethora of multimedia applications exists that require wireless transmission over short distances. A detailed list of such applications, together with estimates of data rates and cost requirements, can be found in [91]. A few example applications are listed in Table 5.1. The high data rate requirement of these applications calls for increased spectral efficiency and higher spectral room. Higher-frequency bands such as the V-band have to be considered to increase the spectral room.

Table 5.1: Applications that could utilize the V-Band. (taken from [91])

Application	**Capacity/ User [Mb/s]**	**Low Cost Requirement**
Wireless (high-quality) video-conferencing	$10 - 100$	yes
Wireless Internet download of lengthy files	$10 - 100$	yes
Wireless TV high-resolution recording camera	$150 - 270$	no
Wireless interactive design	$20 - 40$	yes
Wireless billing	0.1	yes

Another key requirement for such applications, as can be identified from Table 5.1, is a low-cost technology. The SoP approach is critical in achieving low cost and dense

integration leading to the development of high-performance and compact 60 GHz transceiver modules. Many examples of transceiver modules realized using a SOC approach have been reported [38, 72]. Transmitter/receiver modules on multilayer high-temperature co-fired ceramic (HTCC) technology have also been pursued [70]. LCP, for reasons described in Chapter 1, is a preferred technology for developing transceiver modules operating in the V-band.

The goal here is to develop a compact, low-profile, and high-gain antenna array covering the frequency band of 59-64 GHz, and a duplexer covering the frequency ranges of 59-61 GHz for the receive band and 62-64 GHz for the transmit band. The integration of the duplexer and the antenna array is also explored.

5.1.2 Duplexer development

The major requirement for the filter elements of the duplexer is the sharp cut off response outside the passband. An elliptical filter, with finite transmission zero characteristics, is required for this purpose. The isolation requirements of the transceiver and the adjacent location of the two channels warrant that the transmission zeroes of the filters lie close to the passband edges. The filtering circuits employ half-wavelength folded open-loop resonators in a microstrip configuration and make use of coupling structures similar to those reported in Section 3.3.

The duplexer developed in this work was designed to meet the performance specifications outlined in Table 5.2. Based on numerical simulations, fourth order filtering sections were found to be suitable for both the channels. For the filtering sections of a duplexer, a stringent cut off response is generally required only on one side of the passband. Hence, a coupling topology capable of producing an asymmetric response is employed for the filtering sections.

Figure 5.1 shows the coupling structure of the proposed V-band duplexer. The filtering section for channel 1 is composed of resonators a, b, c, and d while the filtering section for channel 2 is composed of resonators e, f, g, and h. A matching network is typically required to combine the two individual filtering sections into a single duplexer.

Table 5.2: Performance specifications for the V-band duplexer.

Parameter	**Channel 1**	**Channel 2**
Center Frequency	60 GHz	63 GHz
Bandwidth	2 GHz	2 GHz
Selectivity (Opposite channel)	> 25 dB	> 25 dB
Return Loss (Passband)	< -10 dB	< -10 dB
Transmission Zero	62 GHz	61 GHz

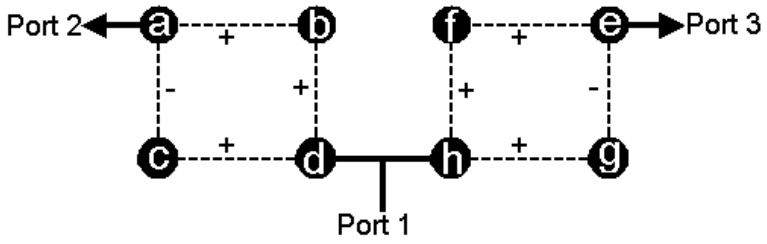

Figure 5.1: Coupling structure of the V-band duplexer.

The design of the individual filtering sections follow the same principles outlined in Section 3.3.2. A coupling matrix was generated that satisfies the given filter specifications. Then similarity transformations were used to determine the coupling matrix that corresponds to the coupling topology chosen for the implementation of the filter. Numerical simulations were then performed to determine the physical dimensions of the filter. Equations (3.3), (3.4), and (3.6) were utilized for this purpose. The coupling matrix synthesized for channel 1 is

$$M = \begin{bmatrix} 0.0042 & 0.0399 & -0.0223 & 0 \\ 0.0399 & 0.0217 & 0 & 0.0399 \\ -0.0223 & 0 & -0.0390 & 0.0223 \\ 0 & 0.0399 & 0.0223 & 0.0042 \end{bmatrix} \quad Q_e = 15.68 \tag{5.1}$$

The coupling matrix synthesized for channel 2 is

$$M = \begin{bmatrix} -0.0040 & 0.0380 & -0.0213 & 0 \\ 0.0380 & -0.0207 & 0 & 0.0380 \\ -0.0213 & 0 & 0.0372 & 0.0213 \\ 0 & 0.0380 & 0.0213 & -0.0040 \end{bmatrix} \quad Q_e = 16.47 \tag{5.2}$$

After completing the design of the individual filtering sections, the matching network that combines the filtering sections was designed to realize the duplexer. A T-junction with impedance transformers is used as the matching network. The width and length of the impedance transformers were optimized for good matching characteristics at Ports 2 and 3 of the duplexer in their respective passbands, while maintaining good isolation characteristics between Ports 2 and 3 across the entire frequency range of interest.

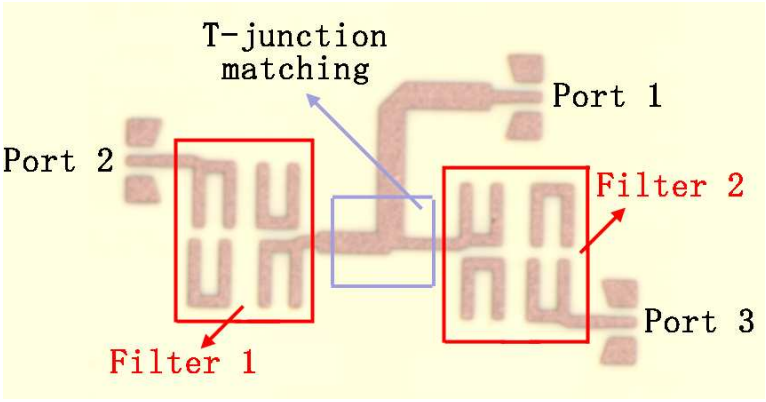

Figure 5.2: Photo of the fabricated V-band duplexer.

Figure 5.2 shows a photo of the fabricated V-band duplexer. The individual filtering sections, the matching T-junction and the location of the Ports are clearly marked. The 90° bent transmission line connected to Port 1 is used only for measurement purposes. The LCP substrate chosen for the design and fabrication of the V-band duplexer is characterized by $\epsilon_r = 3.15$, $tan\delta = 0.004$, a conductor thickness of 18 μm, and a substrate thickness of 203 μm.

Figure 5.3 shows the simulated and measured return loss plots of the developed V-band duplexer. A very good agreement can be observed. The worst return loss measured is -9 dB for channel 1 and -8.5 dB for channel 2. These values are close to the predicted values

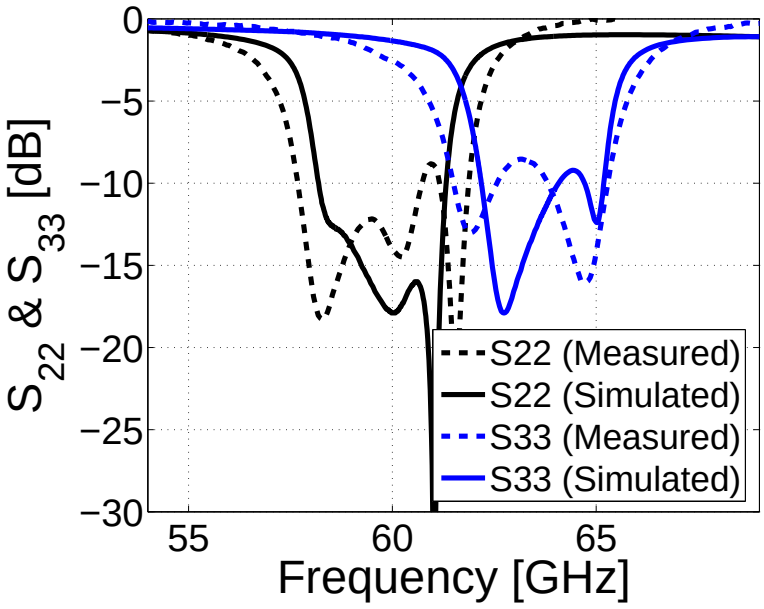

Figure 5.3: Return loss of the V-band duplexer.

and the matching remains satisfactory across the passbands of both the channels.

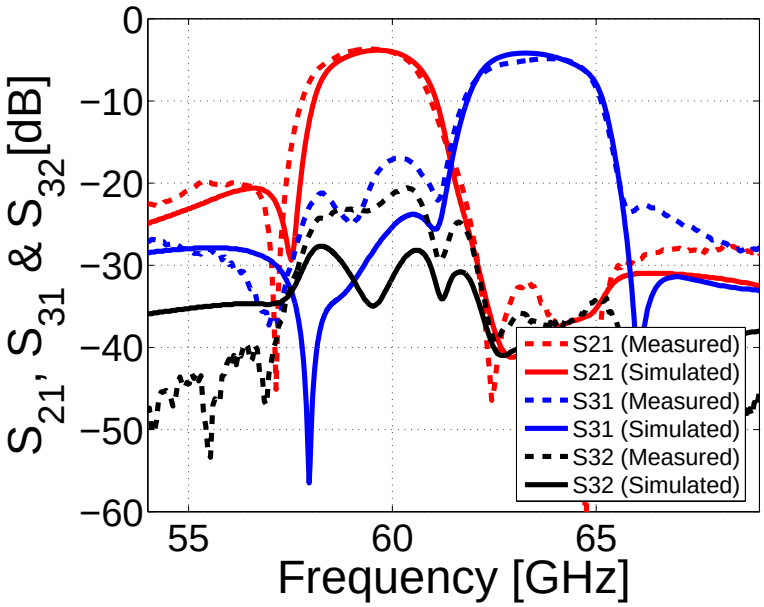

Figure 5.4: Insertion loss and isolation of the V-band duplexer.

Figure 5.4 shows the simulated and measured transmission properties of the duplexer. Again, a good agreement with the simulations can be observed. The measured isolation between the channels is better than 20 dB across the whole band of interest. The measured

selectivity is better than 25 dB for channel 1 and is better than 20 dB for channel 2. For channel 1, a measured insertion loss of -3.7 dB at 59.6 GHz has been achieved. For channel 2, a measured insertion loss of 4.3 dB at 63.5 GHz has been achieved. In our opinion, these results are satisfactory, considering the narrow bandwidth of the channels. Slight discrepancies can be observed as far as the bandwidth is concerned. This could be a result of fabrication inaccuracies. A tighter tolerance is required for a perfect match between simulations and measurements.

The insertion loss is mainly due to the conductor and radiation loss. While a thicker substrate will reduce the conductor loss, it is likely to increase the radiation loss. A stripline configuration may be used to reduce the radiation loss while allowing for a marginal increase in the conductor loss. In such a configuration, care must also be taken to avoid unwanted parallel-plate modes. This is a serious problem at high frequencies such as the frequency of interest. Additionally, the substrate configuration used for the duplexer will also have an impact on the choice of the radiating element. For a microstrip configuration, patch antennas are suitable radiating elements. A slot antenna is appropriate for stripline implementations, but it suffers from a lower directivity compared to a patch antenna. Other multilayer configurations can be tried at the cost of increased design and fabrication complexity. It must be remembered that most of the applications listed in Table 5.1 favored a low-cost implementation. To this end, we believe that a single-layer microstrip implementation is suitable.

5.1.3 Antenna development

As mentioned in the previous section, patch antennas are suitable for integration with microstrip circuits. Patch elements can be easily expanded into an array to improve directivity and gain. Different types of polarizations can be realized by employing different feed arrangements. Patch antennas are relatively compact radiating elements also.

In this section, the design and the development of V-band patch antennas are described. To minimize integration complexities, a 203 μm thick LCP substrate, identical to the one used for the development of the duplexer, is used for the antennas. Figure 5.5 shows the

developed V-band patch antenna. An inset feed has been used to enhance input matching. Physical dimensions of the patch shown in Figure 5.5 are listed in Table 5.3.

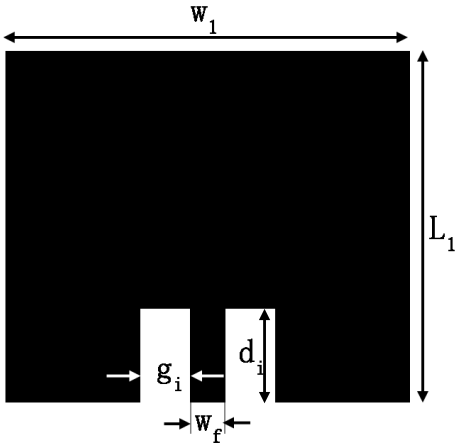

Figure 5.5: V-band patch antenna.

Table 5.3: Physical dimensions of the V-band patch antenna.

Parameter	**Value (μm)**
L_1	1304
w_1	1500
w_f	130
g_i	185
d_i	350

Because the thickness of the substrate is fixed, the design challenge here is to achieve the specified impedance bandwidth of the proposed V-band transceiver. The antenna is required to cover the frequency range of 59 – 64 GHz. This translates into a fractional bandwidth of 8.13%. The physical dimensions of the patch were optimized to maximize its impedance bandwidth. Ansoft-Designer [8], a 2.5-D MOM solver, was used to optimize the antenna's parameters.

Figure 5.6 shows the simulated return loss of the developed V-band patch antenna. The simulations show a better than -10 dB return loss between 60.2 GHz and 62.8 GHz. Bandwidth enhancement is necessary to enable the antenna cover the entire band between 59 GHz and 64 GHz. Typically parasitic radiating elements, either vertically stacked or

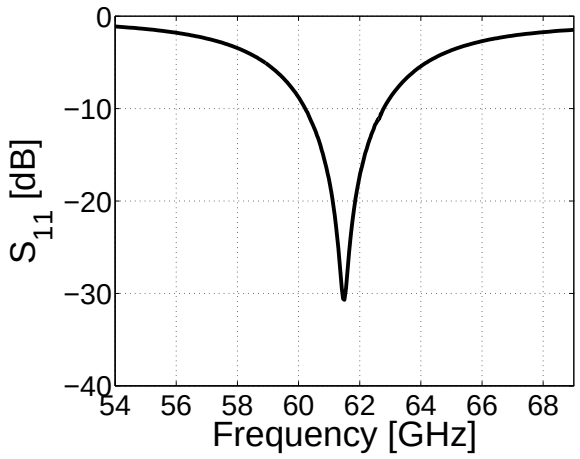

Figure 5.6: Simulated return loss of the V-band patch antenna.

placed laterally, are employed to enhance the bandwidth [60]. However, these methods will necessitate additional conductor layers and, hence, will increase the cost and complexity. Loaded patch antennas can be used to enhance the bandwidth while keeping the compact single-layer profile, but this will reduce the efficiency and gain of the antenna [49]. Another alternative is to employ slotted patch antennas. Irrespective of the technique, the key is to make the antenna support more than one resonant mode and, by keeping the resonant frequencies closer to each other, the bandwidth can be enhanced.

A patch antenna loaded with two L-shaped slots has been developed in this work. Apart from the standard TM_{01} mode, this antenna also supports a $TM_{0\delta}$ mode with 'δ' taking a value between one and two ($1 < \delta < 2$). By carefully optimizing the design parameters, the resonant frequencies of these two modes can be made close enough that a broadband antenna is realized. In this work, a slotted patch antenna has been developed that operates in TM_{01} and $TM_{0\delta}$ modes with a resonant frequency ratio $f_{0\delta}/f_{01} = 1.042$. The design principles employed here are similar to the ones outlined in [103, 92]. However, this author is not aware of any report of an antenna achieving such a small frequency ratio between the said resonant modes. Also, millimeter-wave slotted patch antennas have not been reported before.

Figure 5.7 shows the developed slotted V-band patch antenna. The physical dimensions of the slotted patch shown in Figure 5.7 are listed in Table 5.4.

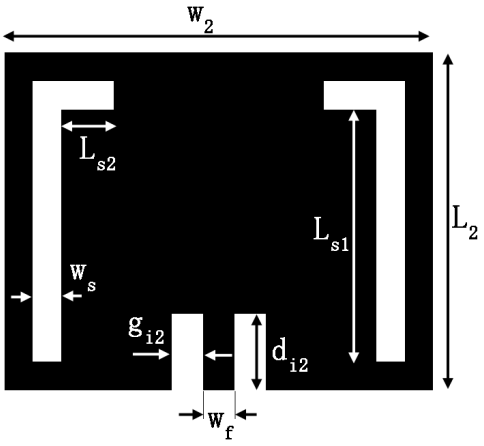

Figure 5.7: V-band slotted patch antenna.

Table 5.4: Physical dimensions of the V-band slotted patch antenna.

Parameter	**Value (μm)**
L_2	1300
w_2	1650
w_f	130
g_{i2}	120
d_{i2}	295
w_s	110
L_{s1}	970
L_{s2}	200

Figure 5.8 shows the simulated return loss of the developed slotted V-band patch antenna. The simulations show a better than -10 dB return loss between 59.3 GHz and 63.7 GHz. This bandwidth is closer to the required bandwidth of the proposed transceiver.

Figures 5.9a and 5.9b show the simulated and measured return loss of the developed regular and the slotted V-band patch antennas, respectively. A reasonable agreement can be observed. Apart from the calibration issues that caused the ripples, the measurement setup itself might have impacted the performance of the antennas.

The measurements show a better than -10 dB return loss between 59.2 GHz and 63.8 GHz for the regular patch and a better than -10 dB return loss between 58.4 GHz and 64.4 GHz for the slotted patch antenna. Although the simulated bandwidth of the slotted patch antenna is closer to the specified bandwidth, measurements show that the regular patch

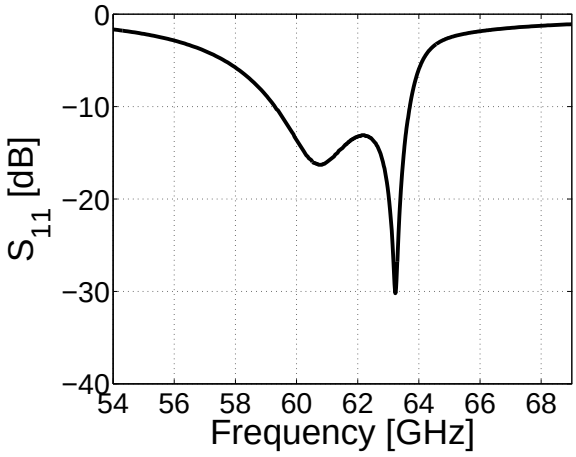

Figure 5.8: Simulated return loss of the slotted V-band patch antenna.

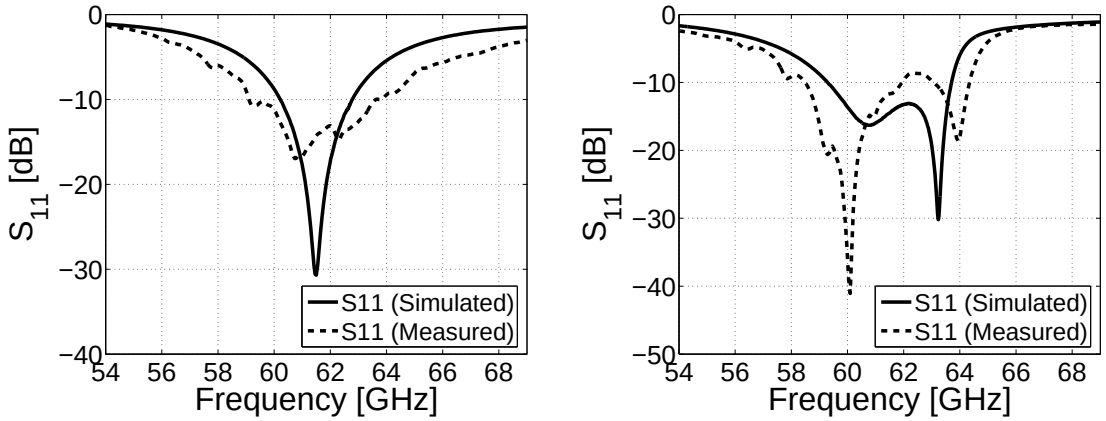

(a) Regular patch.

(b) Slotted Patch.

Figure 5.9: Simulated and measured return loss of the developed V-band patch antennas.

antenna itself has the appropriate bandwidth required for the proposed system.

5.1.4 Duplexer/Antenna integration

Before integrating the duplexer and the radiating element(s), the single radiating elements developed in the previous section were expanded into 2×2 arrays to increase the directivity and gain of the system. Figure 5.10 shows the developed V-band antenna arrays. The elements along the Y-axis are fed in opposite radiating edges and a 180° compensating phase shifter is used as a part of the feed network, so that the elements are always fed with in-phase currents. A corporate feed network, with impedance transformers and T-junctions, is used to expand the arrays along the X-axis. These 2×2 arrays can be considered as basic

sub-arrays for expansion into more general planar $N \times N$ arrays. To minimize parasitic radiation from the feed lines, narrow high-impedance lines are used. Each antenna element and the 2×2 arrays are matched to 100 Ω instead of the standard 50 Ω. The duplexer developed before was also designed with a 100 Ω reference impedance to minimize the need for any impedance transformers while integrating the duplexer with the antenna array(s).

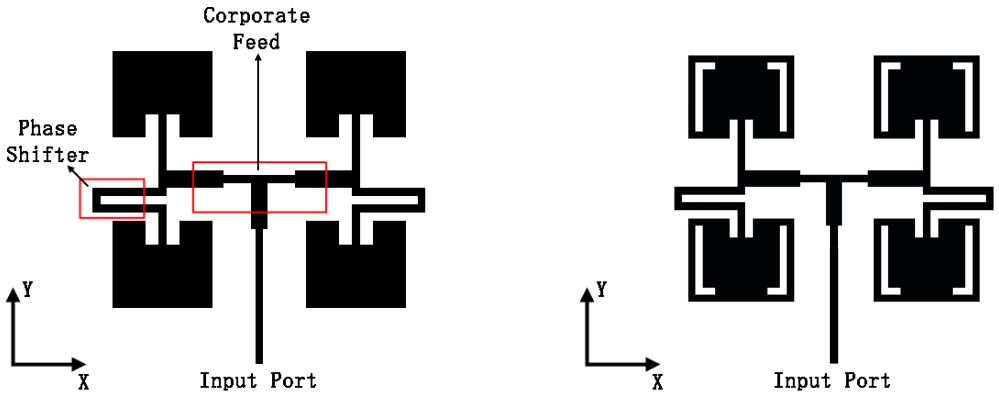

(a) 2×2 array with regular patches

(b) 2×2 array with slotted patches

Figure 5.10: V-band antenna array.

The integration of the array and the duplexer is achieved by connecting Port 1 of the duplexer (Figure 5.2) to the input port of the antenna array (Figure 5.10). When the three-port duplexer is loaded with the antenna array at Port 1, the integrated device becomes a two-port circuit. The duplexer, thus, enables the antenna to be shared between the transmitter and receiver modules of the transceiver. It also provides the necessary isolation between the transmitter and receiver.

Figure 5.11 shows a photo of the fabricated duplexer/antenna (regular patch) integrated module. The module occupies a compact area of 4.9×7 mm^2. A considerable amount of space is occupied by the antenna array. The duplexer elements use folded resonators that are much smaller than the patch antenna elements. The low dielectric constant of LCP results in a bigger wavelength and, hence, a larger area is required for the array . However, as discussed in Chapter 2, the low dielectric constant offers other advantages such as reduced diffraction, higher efficiency, etc. Although both arrays were integrated with the duplexer, only the results for the module with the regular patch antenna array are included here.

From the results, it can be observed that even the regular patch provides the necessary bandwidth. The regular patch is also expected to have a higher radiation efficiency and, hence, it is preferable compared to the slotted patch, as long as the bandwidth specification is met.

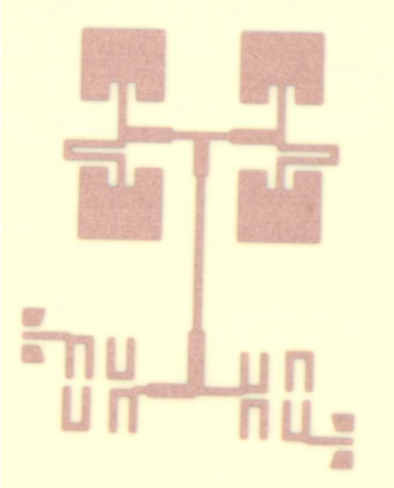

Figure 5.11: Photo of the fabricated V-band duplexer/antenna integrated module.

The simulated and measured scattering parameters of the two-port integrated module are shown in Figure 5.12. The measured isolation is better than 23 dB across the frequency range of interest. The measured return loss is better than -9 dB for both channels. Overall, a good agreement between the simulations and measurements can be observed.

Compact high-performance passive building blocks for a V-band transceiver system have been realized on low-cost LCP technology. The performance of these devices confirm the low-loss characteristics of LCP at millimeter-wave frequencies.

5.2 X-band example

At millimeter-wave frequencies, the wavelengths are smaller. Hence, even the single-layer implementation considered for the V-band module resulted in a compact solution, despite the low dielectric constant of LCP. For the X-band system, where wavelengths are much bigger, we explore a 3-D implementation to achieve a compact size. A multilayer implementation also provides more options for the design of individual components. Figure 5.13

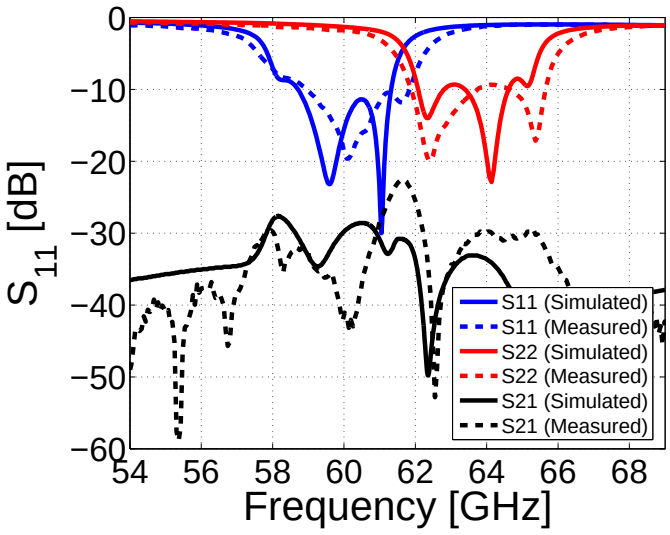

Figure 5.12: Scattering parameters of the V-band duplexer/antenna integrated module.

shows the multilayer stack-up explored for implementing the X-band system.

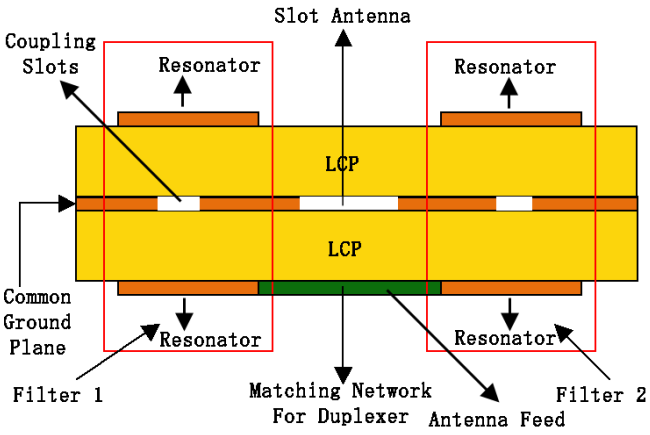

Figure 5.13: Multilayer stack-up used for implementing the X-band system.

5.2.1 Duplexer development

The duplexer developed in this work was designed to meet the performance specifications outlined in Table 5.5. The locations of the transmission zeros were chosen to provide maximum selectivity for the two channels and also to ensure good isolation between them. For the filtering circuits of a duplexer, a stringent cut off response is generally required only on one side of the passband. However, a coupling topology that produces a symmetric

response was employed. Topologies that generate a symmetric response are generally easier to implement than those that result in an asymmetric response. As a result, each filtering circuit was designed to produce four finite frequency transmission zeros, two on either side of the passband. Fourth order filters with direct source-load coupling were employed for this purpose. These filters, which have equal number of poles and zeros, are known as fully canonical filters.

Table 5.5: Performance specifications for the X-band duplexer.

Parameter	**Channel 1**	**Channel 2**
Center Frequency	9.5 GHz	10.5 GHz
Bandwidth	0.5 GHz	0.5 GHz
Selectivity (Opposite channel)	> 25 dB	> 25 dB
Return Loss (Passband)	< -10 dB	< -10 dB
Transmission Zeros	10 & 10.5 GHz	9.5 & 10 GHz

Figure 5.14 shows the coupling structure used for the X-band duplexer. The filtering section for channel 1 is composed of resonators a, b, c, and d while the filtering section for channel 2 is composed of resonators e, f, g, and h. The empty circles represent NRNs. The NRNs w and x represent the source and load nodes for the filtering section of channel 1, while the NRNs y and z represent the corresponding nodes for channel 2. Coupling between these nodes is necessary to achieve the desired transmission zeros. A fourth order filter can realize four transmission zeros either through internal NRNs or through direct source-load coupling. In this case, we use direct source-load coupling for each filtering section. It is worth remembering that we had employed internal NRNs to achieve fully canonical filtering for the filter discussed in Section 4.1.

The filtering circuits of the X-band duplexer employ half-wavelength folded open-loop resonators and use a multilayer configuration. The configuration consists of two LCP substrates ($\epsilon_r = 3.1$, $\tan\delta = 0.003$), each 102 μm thick, stacked together. For channel 1, the resonators a, and c and the NRN w are placed on the top surface, while the resonators b, and d and the NRN x are placed on the bottom surface. For channel 2, the resonators e,

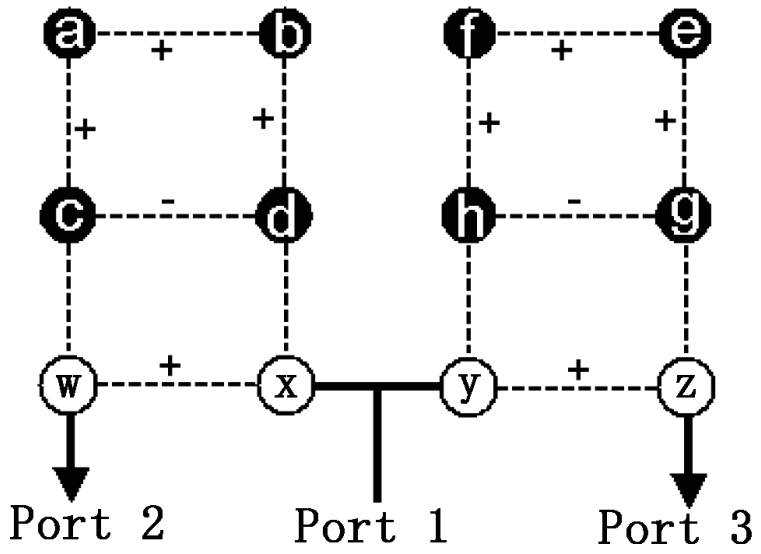

Figure 5.14: Coupling structure of the X-band duplexer. The filled circles represent resonators and the empty circles represent NRNs.

and g and the NRN z are placed on the top surface, while the resonators f, and h and the NRN y are placed on the bottom surface. Table 5.6 summarizes the coupling method and coupling type employed between different resonating and non-resonating nodes for both the channels.

Table 5.6: Coupling type and method utilized to realize the X-band duplexer.

Attribute	**Coupling method**	**Coupling type**	**Coupling sign**
$m_{a,c}$, $m_{b,d}$, $m_{f,h}$, $m_{e,g}$	Proximity	Mixed (type-1)	positive
$m_{a,b}$, $m_{e,f}$	slot	Mixed (type-2)	positive
$m_{c,d}$, $m_{h,g}$	slot	Electric	negative
$m_{w,x}$, $m_{y,z}$	slot	Magnetic	positive
$m_{w,c}$, $m_{x,d}$, $m_{y,h}$, $m_{z,g}$	Tapping	–	–

The design of the individual filtering sections follow the same principles outlined in Section 3.3.2. A coupling matrix was generated that satisfies the given filter specifications.

Then similarity transformations were used to determine the coupling matrix that corresponds to the coupling topology chosen for the implementation of the filter. Numerical simulations were then performed to determine the physical dimensions of the filter. Equations (3.3) and (3.6) were utilized for this purpose. The coupling matrix synthesized for channel 1 is

$$M = \begin{bmatrix} 0 & -0.0595 & 0 & 0 & 0 & 0.0012 \\ -0.0595 & 0 & 0.0511 & 0 & -0.0149 & 0 \\ 0 & 0.0511 & 0 & 0.0450 & 0 & 0 \\ 0 & 0 & 0.0450 & 0 & 0.0511 & 0 \\ 0 & -0.0149 & 0 & 0.0511 & 0 & -0.0595 \\ 0.0012 & 0 & 0 & 0 & -0.0595 & 0 \end{bmatrix} \tag{5.3}$$

The coupling matrix synthesized for channel 2 is

$$M = \begin{bmatrix} 0 & -0.0539 & 0 & 0 & 0 & 0.0010 \\ -0.0539 & 0 & 0.0462 & 0 & -0.0133 & 0 \\ 0 & 0.0462 & 0 & 0.0407 & 0 & 0 \\ 0 & 0 & 0.0407 & 0 & 0.0462 & 0 \\ 0 & -0.0133 & 0 & 0.0462 & 0 & -0.0539 \\ 0.0010 & 0 & 0 & 0 & -0.0539 & 0 \end{bmatrix} \tag{5.4}$$

Although the filtering sections are of order four, a 6×6 coupling matrix is used here, because of the introduction of direct source-load coupling.

The next step is to design the matching network that combines the filtering sections to realize the duplexer. A T-junction with impedance transformers is used as the matching network. The width and length of the impedance transformers were optimized for good matching characteristics at Ports 2 and 3 of the duplexer in their respective passbands, while maintaining good isolation characteristics between Ports 2 and 3 across the entire frequency range of interest.

Figure 5.15 shows photos of the measurement setup used for measuring the fabricated X-band duplexer. Only the resonators on the top surface are visible. The matching network

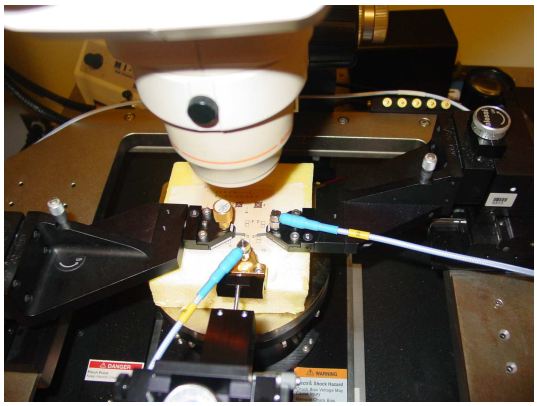

(a) Measurement setup.

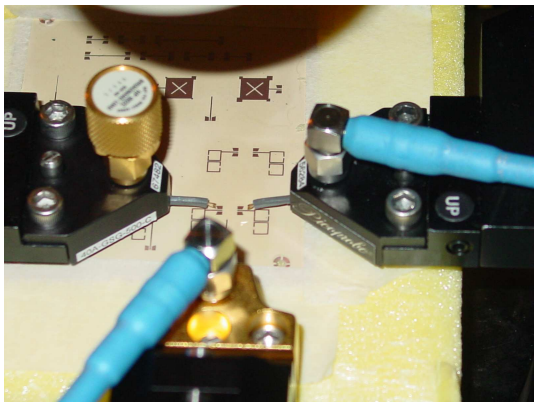

(b) Zoomed in picture showing the standard load used for terminating one of the three ports.

Figure 5.15: Setup for measuring the X-band duplexer.

that includes the impedance transformers and the T-junction are on the bottom surface. To calculate the scattering parameters of the three-port duplexer, standard two-port measurements were made, while terminating the third port with a broadband 50Ω calibration load. This measurement is repeated for every pair of ports and redundant measurements were discarded. The duplexer occupied a compact area of $14.8 \times 5.9\ mm^2$. The matching network used occupied a significant portion of the total area. The impedance transformers of the matching network can be folded to further reduce the size. A comparable 2-D implementation will occupy an area of $25.6 \times 5.9\ mm^2$. In addition, fully canonical filtering may not be possible in such a 2-D implementation. In the multilayer implementation, coupling slots etched in the ground plane are used for coupling between NRNs. This is a compact, effective way of achieving coupling between different nodes of a filter and is not possible in a single-layer implementation. The difference in size between the two implementations will be further enhanced for higher order filters and/or for a multilayer implementation with more than two resonator layers.

Figure 5.16 shows the simulated and measured return loss plots of the developed X-band duplexer. A very good agreement can be observed. The worst return loss measured is -10 dB for channel 1 and -11 dB for channel 2. The matching remains satisfactory across the passbands of both the channels.

Figure 5.17 shows the simulated and measured transmission properties of the duplexer.

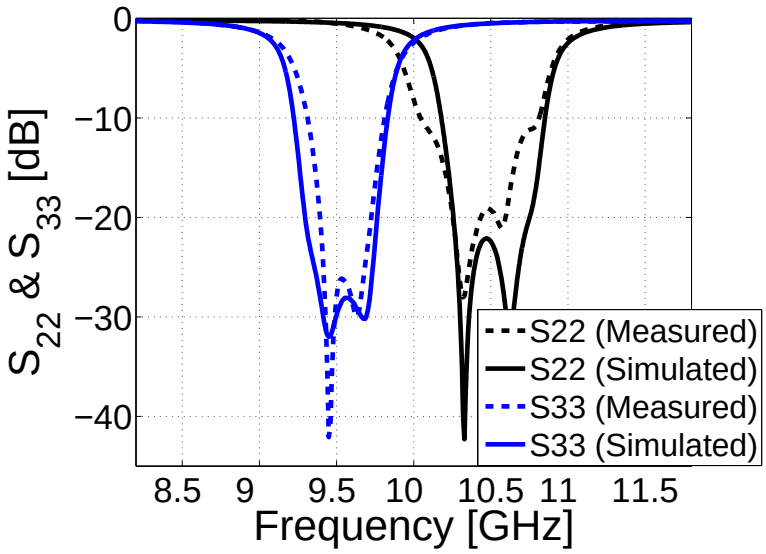

Figure 5.16: Return loss of the X-band duplexer.

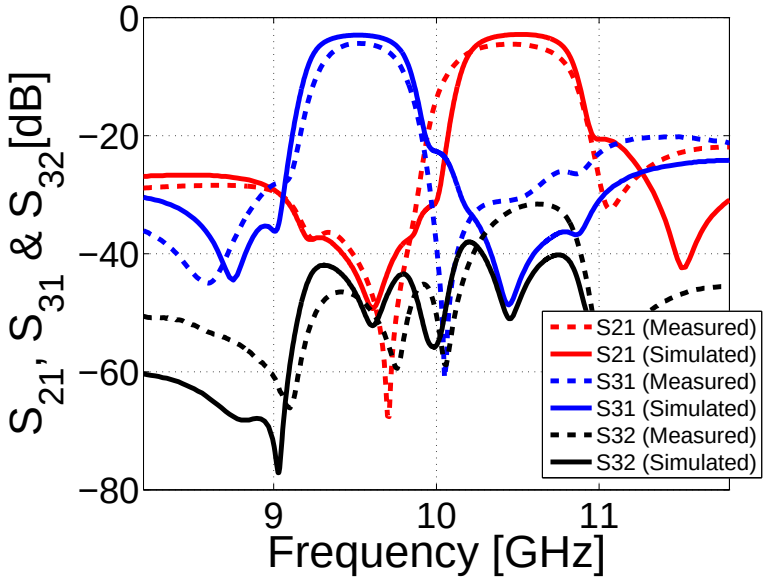

Figure 5.17: Insertion loss and isolation of the X-band duplexer.

Again, a good agreement with the simulations can be observed. The measured isolation between the channels is better than 31 dB across the whole band of interest. The measured selectivity is better than 25 dB for channel 1 and is better than 30 dB for channel 2. For channel 1, a measured insertion loss of -3.9 dB at 9.5 GHz has been achieved. For channel 2, a measured insertion loss of 4.0 dB at 10.5 GHz has been achieved. Slight discrepancies can be observed as far as the bandwidth is concerned. This could be a result of fabrication

inaccuracies. A tighter tolerance is required for a perfect match between simulations and measurements.

5.2.2 Antenna development

Many choices are available for developing the antenna to be integrated with the duplexer presented in Section 5.2.1. Patch antennas can be used either on the top or bottom surface, sharing the ground plane with the filter elements of the duplexer. Slot antennas can be etched on the ground plane and fed either by a coplanar waveguide on the same plane or by a microstrip line that is printed on the top or bottom surface. Irrespective of the type of the radiating element, it is advantageous to employ a simple and low-loss interconnect between the antenna and the duplexer. In addition, the antenna should be able to achieve the required impedance bandwidth. In this case, the antenna is required have a better than -10 dB return loss between 9.25 GHz and 10.75 GHz, which are the far-side edges of the passbands of the two channels. A wide-slot antenna was identified as a suitable radiating element to meet the goals of the proposed X-band transceiver.

Figure 5.18 shows the top and side view of the developed wide-slot antenna. The stack-up is identical to the one used for the duplexer. The microstrip feed for the slot antenna is placed on the bottom surface. This enables a direct transmission-line connection between Port 1 of the duplexer and the feed for the antenna.

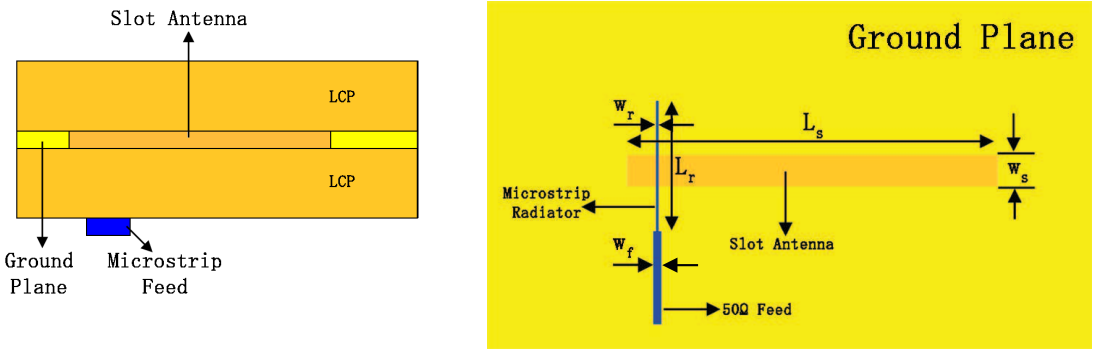

(a) Side view showing the stack-up for the slot antenna.

(b) Top view of the wide-slot antenna (all layers interlaced)

Figure 5.18: X-band wide-slot antenna.

The physical dimensions of the wide-slot antenna shown in Figure 5.18b are listed in Table 5.7.

Table 5.7: Physical dimensions of the X-band wide-slot antenna.

Parameter	**Value (mm)**
L_s	12.00
w_s	1.00
L_r	4.25
w_r	0.10
w_f	0.25

Because of the thin dielectric substrates used, a conventional slot antenna cannot meet the bandwidth requirements of the proposed transceiver. To enhance the bandwidth, a wide-slot antenna together with a quarter-wavelength microstrip resonator is employed. By carefully adjusting the resonant frequencies of the microstrip resonator and the wide-slot antenna, a broadband radiating element can be realized [107]. Figure 5.19 shows the simulated and measured return loss plots of the developed X-band wide-slot antenna.

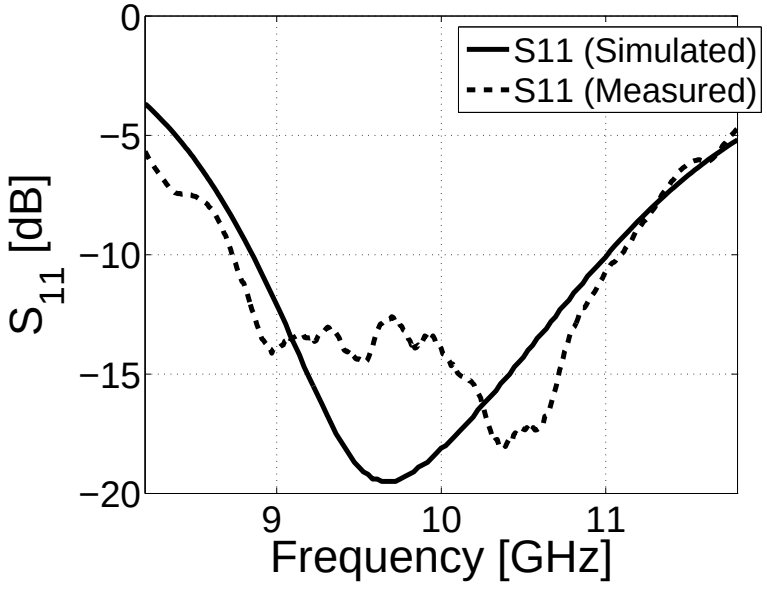

Figure 5.19: Simulated and measured return loss of the X-band wide-slot antenna.

A good agreement between the simulations and measurements has been achieved. The measured antenna showed a better than -10 dB return loss between 8.75 GHz and 11.1 GHz,

comfortably covering the required frequency range.

5.2.3 Duplexer/Antenna integration

The integration of the radiating element and the duplexer is carried out in a way similar to the one described in Section 5.1.4. The duplexer enables the antenna to be shared between the transmitter and receiver modules of the transceiver, besides providing the necessary isolation between the modules. Figure 5.20 shows a 3-D view of the multilayer stack-up used for the integrated X-band module. The module occupies a compact size of $18 \times 11\ mm^2$. The use of thin dielectric sheets enabled a compact 3-D module with the module thickness only being 0.26 mm.

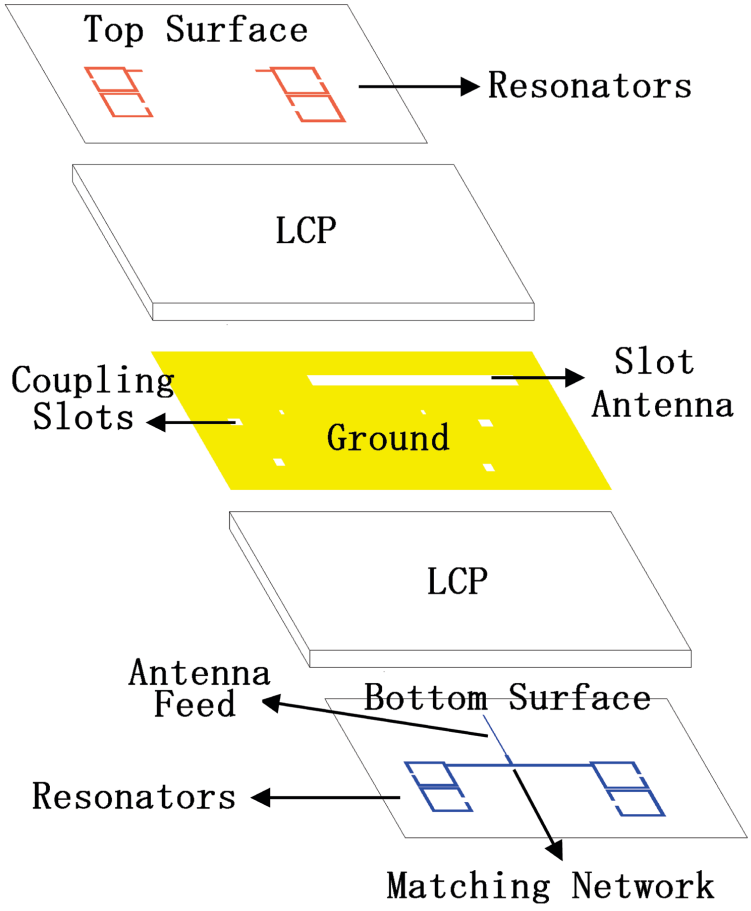

Figure 5.20: 3-D view of the multilayer stack-up of the X-band integrated module.

The simulated and measured scattering parameters of the two-port integrated module

are shown in Figure 5.21. The measured isolation is better than 26 dB across the frequency range of interest. The measured return loss is better than -10 dB for both channels. Overall, a good agreement between the simulations and measurements can be observed.

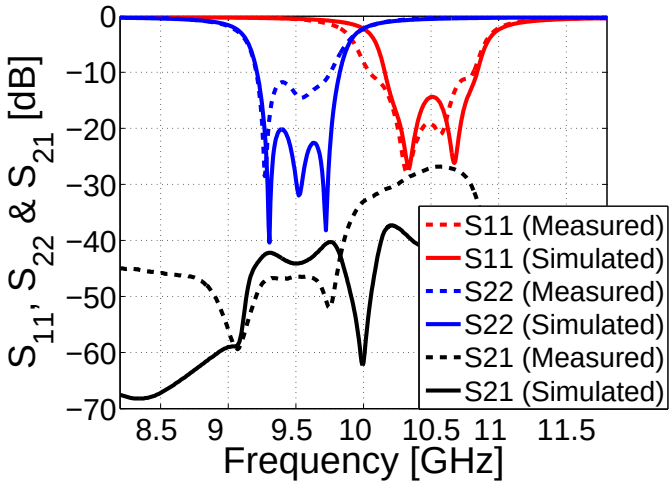

Figure 5.21: Scattering parameters of the X-band duplexer/antenna integrated module.

An integrated passive module for a X-band transceiver system has been developed demonstrating the multilayer lamination capabilities of LCP.

5.3 Chapter summary

In this chapter, we presented the integration of passive building blocks such as filters, matching networks, and radiating elements on LCP technology. Two prototype modules were developed - one operating in the V-band to cater for short-range wireless applications providing high capacities, and the other operating in the X-band.

The V-band module utilized folded open-loop resonators for the filtering sections of the duplexer, and patch antennas as radiating elements. A single-layer implementation is considered to minimize design and fabrication complexity, and to achieve a low-cost module. Measurements agree well with the simulations, validating the employed design techniques.

The X-band module utilized a multilayer stack-up to achieve a compact size. Direct source-load coupling in a multilayer filter configuration has been employed for the first time. Both proximity coupling and slot coupling were utilized to achieve the necessary couplings between different resonators and NRNs. A wide-slot antenna along with a microstrip

resonator was employed to realize the necessary bandwidth for the radiating element. The integrated module occupied a compact size and showed good matching and isolation characteristics.

CHAPTER VI

CONCLUSIONS

The investigation of LCP technology to function as a low-cost next-generation organic platform for designs up to millimeter-wave frequencies has been performed. Prior to this research, the electrical performance of LCP had been characterized only with the implementation of standard transmission lines and resonators. In this research, a wide variety of passive functions, on multilayer LCP technology, have been developed and characterized for the first time.

Dual-frequency/dual-polarization antenna arrays have been developed utilizing LCP's multilayer lamination capabilities. Return loss and radiation pattern measurements were provided along with efficiency calculations, stressing the advantages of using LCP for antenna applications. The suitability of these structures for use in conformal applications has been demonstrated. The integration of these arrays with MEMS switches was pursued to achieve real-time polarization reconfigurability. This is the first such illustration. The results achieved demonstrate the applicability of LCP for the development of low-cost, light-weight, and conformal antennas for future communication and remote sensing systems operating up to millimeter-wave frequency ranges.

Compact, planar low-pass and band-pass filter prototypes have been developed on both single-layer and multilayer LCP technology. These prototypes operated in a wide range of frequencies and the characterization of these devices helped understand LCP's electrical performance in those frequency ranges. Synthesis and design techniques to design coupled-resonator band-pass filters have been explored. Unloaded quality factor of resonators, fabricated on LCP and operating in microwave and millimeter-wave frequencies, were calculated and reported for the first time. Novel filter prototypes that can make use of LCP's multilayer lamination capabilities have been designed. The contributions of this section of research are not just limited to characterization of LCP's performance. This

research has also resulted in a broad understanding of filtering techniques available with the said implementation methods.

Examples of integrated passive modules for use in transceiver systems have been presented. Filters, matching networks, and radiating elements have been integrated to realize the final passive modules. A V-band module that uses folded open-loop resonators and patch antenna arrays has been implemented on LCP and characterized. Measurement results for the individual components and for the integrated module were provided. A multilayer implementation was considered for the X-band module. Direct source-load coupling in a multilayer filter configuration was employed for the first time to meet the stringent demands set forth in the specifications of the transceiver system. The integrated X-band module occupied a compact size and showed good matching, selectivity, and isolation characteristics.

To summarize, a wide variety of passive functions operating in a broad range of frequencies have been developed on multilayer LCP technology. LCP's lamination capabilities to generate homogenous multilayer architectures have been researched. Novel prototype components that can make use of such capabilities have been explored. Antenna arrays, matching networks, filters, duplexers, and integrated modules have been designed, implemented and characterized. The performance of these passive functions provides insight into the electrical characteristics of LCP at RF, microwave, and millimeter-wave frequencies and confirms the potential of LCP to function as an organic platform for SoP-based wireless applications.

APPENDIX A

DUAL-BAND FILTERS

This section includes the implementation and measurement of several dual-band filters for WLAN applications. These dual-band filters were designed by researchers at the Brest University. This author's contribution is only to implement them on LCP technology and to characterize their performance. These dual-band filters have been designed based on the concept of dual-behavior resonators [82]. A dual-behavior resonator (DBR) consists of two stopband elements connected in parallel. Each stopband element creates a transmission zero while the passband response is controlled by constructive recombination of the frequency responses of the stopband elements. Fig A.1 shows an example of a DBR with its frequency response. The single-band DBR can be extended to a dual-band DBR by adding another stopband element in parallel. Fig A.2 shows a schematic of a dual-band DBR with its frequency response. The advantage of these DBRs is that the stopband and passband response of these structures can be independently controlled. Quarter-wavelength open-ended stubs have been used as the stopband resonators together with a stepped impedance approach to control the center frequencies of the passbands.

Three dual-band filters meeting the specifications of 802.11 b,g (2.412-2.484 GHz) for the lower band and the specifications of 802.11 a-L (5.180-5.320 GHz), 802.11 a-H (5.745-5.805 GHz) and 802.11 a-L&H (5.180-5.805 GHz) for the upper band are presented.

These filters were fabricated on LCP substrate characterized by $\epsilon_r = 2.9$, $tan\delta = 0.003$, substrate thickness = 330 μm, and conductor thickness = 18 μm. The fabrication process is the same as explained in Section 2.3.2. Although all these filters are essentially single-layer designs, bonding is still required to realize the desired substrate thickness, as LCP sheets from Rogers Corporation are available only in certain discrete thickness. In this case, a 102 μm core LCP layer was bonded with an 203 μm core LCP layer using a 25 μm bonding layer to give a total thickness of 330 μm. The designed filters were then patterned and

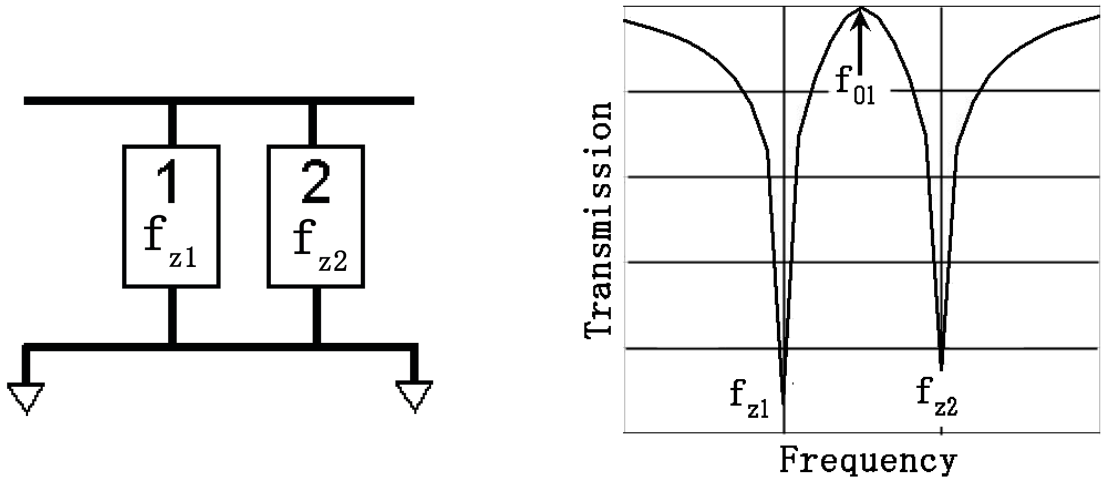

(a) Schematic (b) Frequency response

Figure A.1: DBR.

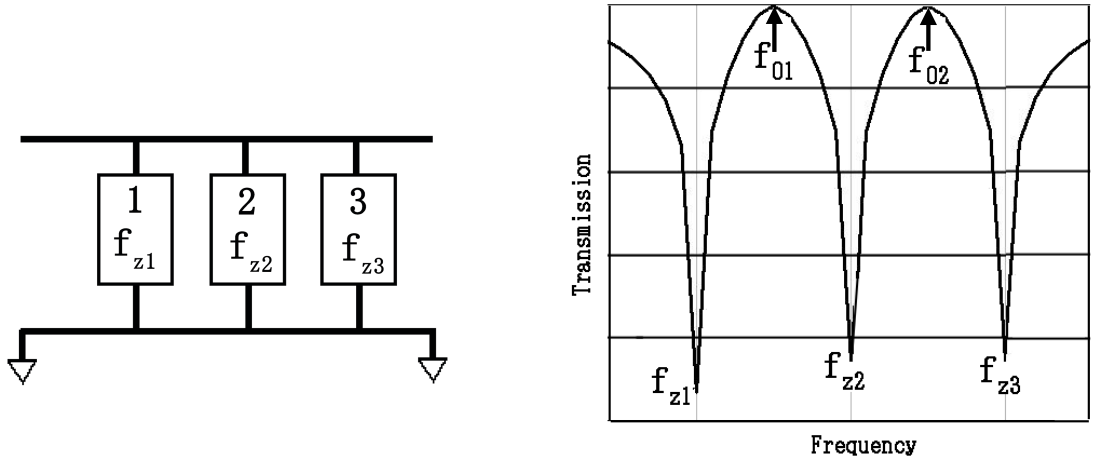

(a) Schematic (b) Frequency response

Figure A.2: Dual-band DBR.

measured.

Figures A.3a, A.4a, and A.5a show photos of the fabricated dual-band filters and Figures A.3b, A.4b and A.5b show the simulated and measured scattering parameters of the filters, respectively. A very good agreement, in general, can be observed. The insertion loss and bandwidth characteristics of the filters are summarized in Table A.1. From the photos, it can be observed that the three filters share some common sections and simple modifications in one filter can result in the realization of another filter. This demonstrates

the inherent flexibility of the DBR design methodology. These filters occupied a compact area of $27 \times 19\ mm^2$ (excluding the size of pads for co-axial connections).

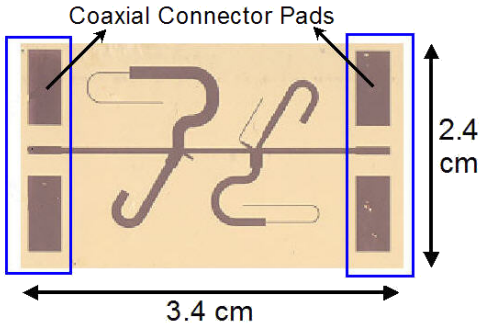

(a) Photo of the fabricated filter

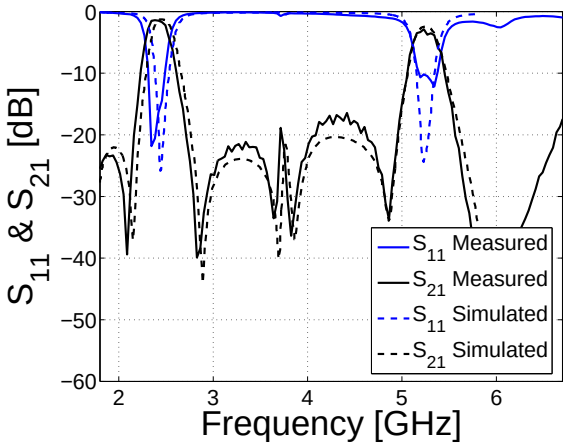

(b) Simulated and measured S-parameter results

Figure A.3: Dual band filter - 802.11 b,g,a-L.

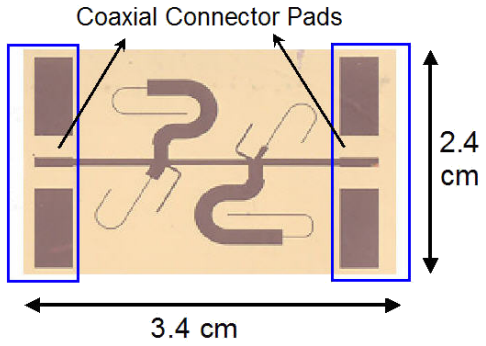

(a) Photo of the fabricated filter

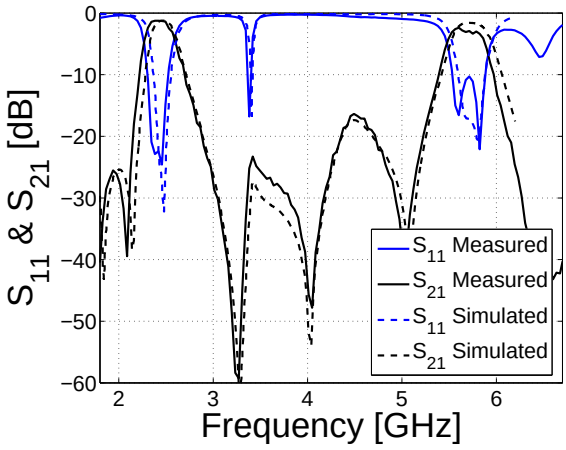

(b) Simulated and measured S-parameter results

Figure A.4: Dual band filter - 802.11 b,g,a-H.

The measured bandwidth for both bands agrees well with the predicted ones. The insertion loss for the lower band is satisfactory. The measured loss for the upper band is more than the predicted loss. It can be observed from the figures that this is directly related to the deterioration in the return loss. This, in conjunction with the ripples in the measurement, could have resulted from an unsteady solder connection of the co-axial connectors during measurements. The unsteady solder connection is because of the flexible nature of the LCP substrate. For the filters reported in Chapters 3 and 4, we used an

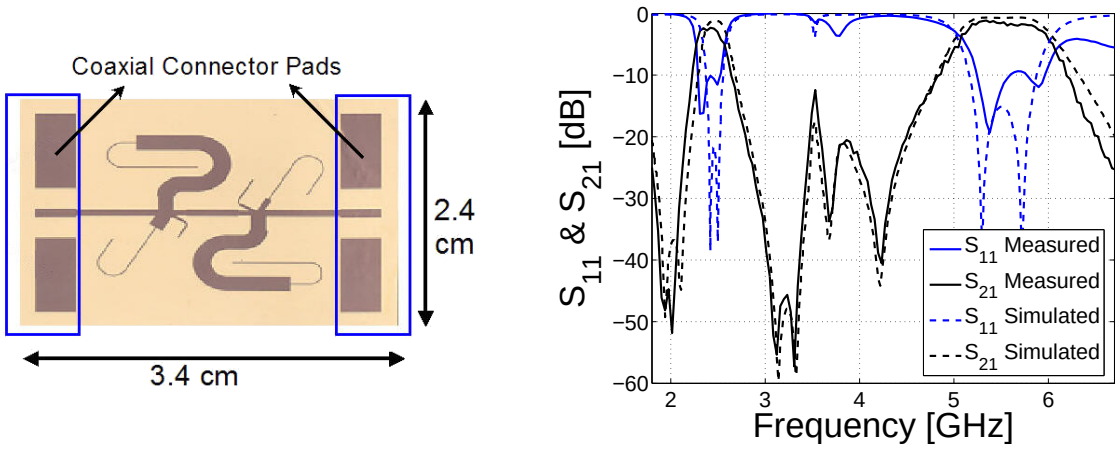

(a) Photo of the fabricated filter

(b) Simulated and measured S-parameter results

Figure A.5: Dual band filter - 802.11 b,g,a-L&H.

Table A.1: Comparison of full-wave simulation and measurement results for the dual-band filters.

Attribute		**Lower Band**		**Upper Band**	
		Insertion Loss (dB)	Bandwidth (GHz)	Insertion Loss (dB)	Bandwidth (GHz)
Filter 1	Simulated	-1.27	0.24	-2.45	0.27
	Measured	**-1.4**	**0.25**	**-2.9**	**0.28**
Filter 2	Simulated	-1.23	0.28	-1.6	0.43
	Measured	**-1.25**	**0.31**	**-2.4**	**0.42**
Filter 3	Simulated	-1.3	0.26	-0.7	1.1
	Measured	**-2.3**	**0.3**	**-1.21**	**0.94**

on-wafer measurement setup with CB-CPW probes and, hence, we were able to obtain stable and repeatable measurements. However, that measurement setup and associated calibration lines are not suitable for low-frequency measurements (below 3 GHz), such as the ones required here. As a result, we used co-axial connectors and the measurement setup is partly responsible for the discrepancies observed between measurements and simulations.

Table A.2 compares the results achieved for the WLAN filters in this research with other works reported in the literature. As seen from the table, the results achieved in this work strike a good balance between insertion loss, rejection and overall size.

Table A.2: Performance comparison of the dual-band WLAN filters implemented in this research with other published works.

Technology	**Insertion loss**		**Rejection between the bands**	**Area**
	2.4 GHz	**5 GHz**		
Duroid [97]	N/A	N/A	$> 20\ dB$	$120 \times 20\ mm^2$
Rogers RO3003 [96]	2.8 dB	3.3 dB	$> 30\ dB$	$54 \times 60\ mm^2$
LCP [23]	1.8 dB	1.5 dB	$> 4\ dB$	$5.1 \times 5.3\ mm^2$
This work	**1.25 dB**	**2.4 dB**	**> 17 dB**	$\mathbf{27 \times 19\ mm^2}$

APPENDIX B

ASYMMETRIC MODULAR FILTERS

Chapters 3 and 4 presented work on band-pass filters of varying order using different kinds of resonators developed on both single and multilayer LCP technology. Most of these filters were designed to have finite frequency transmission zeros on either side of the passband. Specifically, the coupling topologies used resulted in a symmetric frequency response. Pointers were provided in Section 3.3.2 to alter the skirt properties of the open-loop filters by modifying the input/output tap combinations, but largely the focus was on synthesizing symmetric filters. The synthesis framework, which was used to design these filters, is not restricted to designing symmetric filters.

In this section of research, the design and implementation of microstrip asymmetric filters with one or more transmission zeros (TZs) on the low side of the passband will be presented. Although both direct [25, 83] and iterative synthesis techniques [13] are available, higher order filters designed using such methods tend to be highly sensitive to manufacturing tolerances. If the filters are designed using coupled resonator topology, for example, the filter response could be too sensitive to small variations in coupling coefficients. Hence, there is a strong interest in developing modular filters that can reduce the effect of fabrication errors on filter performance [12]. For the filters developed here, modularity was achieved by cascading basic building blocks with NRNs. The building blocks are realized using a coupling scheme that is suitable for a microstrip implementation. In particular, the building block is realized with only one type of coupling.

As seen with the other prototype filters developed in this work, more than one coupling path between the input and output is necessary to generate finite frequency TZs. The objective is to synthesize a lower order filter, with a single TZ, that can act as a basic building block and can be cascaded in a systematic way to generate modular higher order filters. Figure B.1a shows the coupling scheme used to realize asymmetric filters described

in this section. The filled dots represent the resonators and the empty dots represent the ports or the non-resonating nodes. A negative coupling between the resonators will realize a TZ on the low side of the passband while a positive coupling will shift the TZ to the high side. It is different from the coupling scheme employed in past research [10] referred to as the 'box section' or the 'doublet' and shown in Figure B.1b. The schemes shown are the only configurations that can realize a 2-pole, 1-zero filter. Traditionally the box-section is preferred because it does not require any diagonal coupling. However, the scheme used in this work is more suitable for microstrip implementations, because all source-to-resonator and load-to-resonator couplings (S-1, L-1 and L-2 in Fig. 1) can have the same sign irrespective of TZ location. This allows the filter to be realized with only one type of coupling. It can be shown, with the aid of similarity transformations [25], that the box section will always require coupling coefficients of both signs.

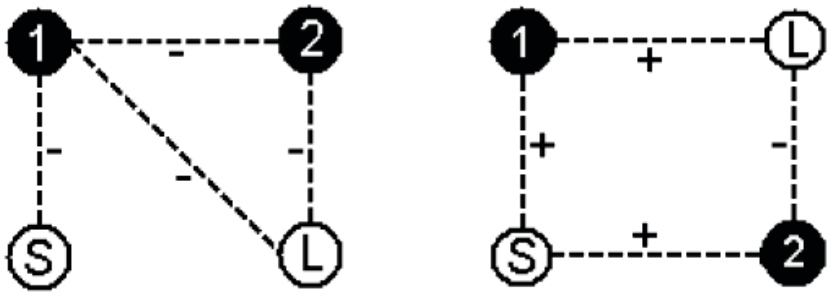

(a) Coupling scheme used in this work. (b) Box section.

Figure B.1: Second order coupling scheme with source-load multiresonator coupling.

Based on the synthesis technique described in Section 3.3.2, two asymmetric filters each with one TZ located on the low side have been designed and implemented. Both filters have the same center frequency (f_0 = 10.1 GHz) but their characteristics differ in the location of TZ. The location of the TZs are f_z = 9.0 GHz and f_z = 8.4 GHz, respectively, for the two filters. The coupling matrices for these filters are nearly identical except for 'm_{L-1}'. Microstrip, half-wavelength, folded open-loop resonators are used to realize these filters. Figure B.2 shows the layout of the asymmetric filter designed and implemented on LCP. ADS-Momentum was used to extract the coupling coefficients and to obtain the physical

dimensions of the filters. The coupling matrix contains two types of coupling coefficients - (1) coupling between a resonating and non-resonating node (source/ load); (2) coupling between two resonating nodes. The former coupling is related to the external quality factor of the resonator and is determined by (3.6). The latter coupling is deduced based on (3.4), since the resonators are asynchronously tuned.

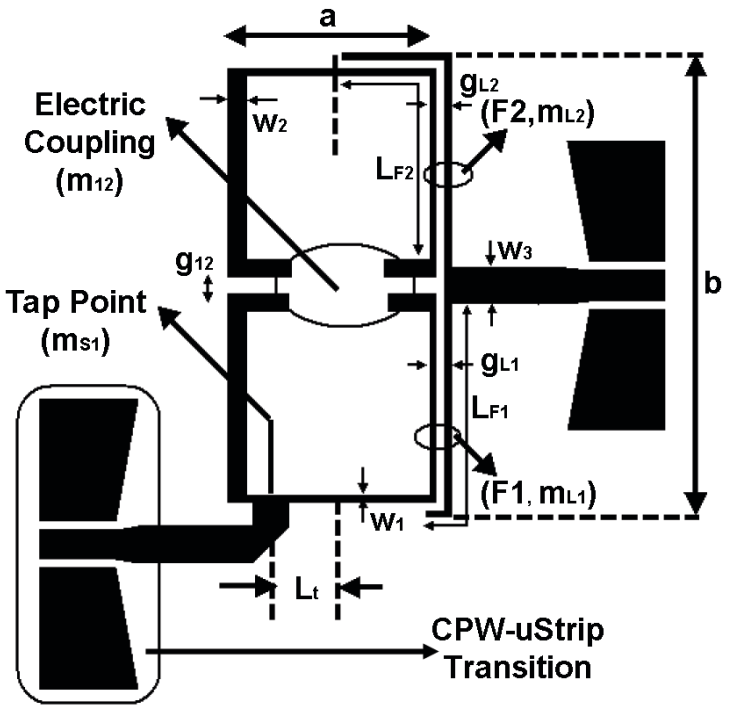

Figure B.2: Layout of the second order asymmetric filter, with one TZ, implemented on LCP.

The coupling scheme requires that the load node be coupled to both resonators 1 and 2. To achieve this, two feeding arms (F_1 and F_2) are gap coupled to the resonators and then a T-junction is used to combine them to form the load node. The external quality factor and hence the coupling strength depends on a number of factors such as the gaps (g_{L-1} and g_{L-2}), the coupled length (L_{F1} and L_{F2}) and the width of the coupled arms (w_1). Figure B.3 shows the plot of coupling strength (m_{L-1} and m_{L-2}) versus gaps (g_{L-1} and g_{L-2}) for a fixed set of other parameters. The coupling between the source node and resonator 1 is realized by tapping the resonator at an appropriate location. Gap coupling could also be used for the source node. Tapping is used just to demonstrate the flexibility

available with such resonators. The relationship between the coupling strength and the tapping location is given by (3.5).

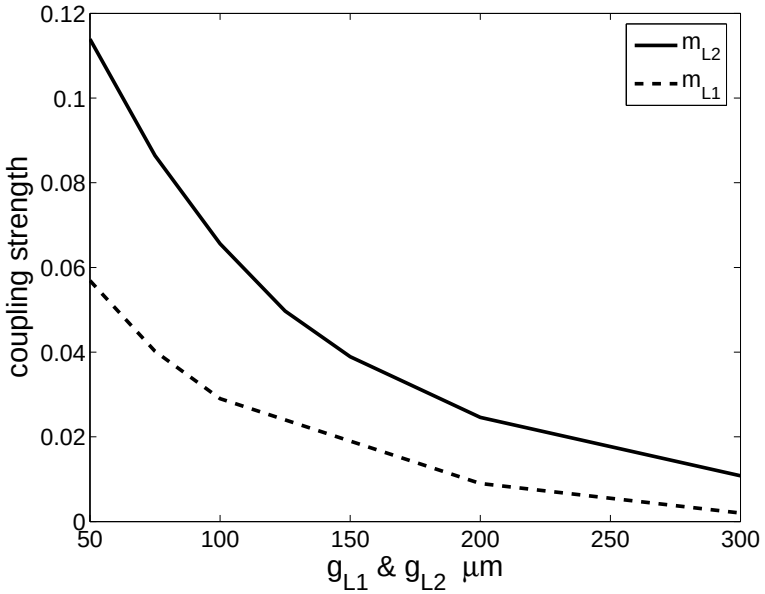

Figure B.3: Coupling strength (m_{L-1} and m_{L-2}) Vs gaps (g_{L-1} and g_{L-2}). $w_1 = 100$ μm ; $L_{F1} = 2975$ μm ; $L_{F2} = 4075$ μm.

The required negative coupling between the resonators is realized by placing them side-by-side along the open edge of the resonators, where the electric fields have maximum strength. The coupling strength depends on the spacing between the resonators, the width of the coupled arms (w_2) and the length of the coupled arms (a). Figure B.4 shows the plot of coupling strength (m_{1-2}) versus the spacing between the resonators (g_{1-2}) for a fixed 'a' and 'w_2'.

Table B.1 summarizes the physical parameters of the designed filters. It can be noted from Table B.1 that the main difference between the two filters is 'g_{L-1}', which corresponds to 'm_{L-1}', as expected.

The simulated and measured results for the filter with TZ at 9 GHz are shown in Figure B.5. The measured results agree well with the predicted values. The location of the TZ is accurately predicted and the filter exhibited a low in-band insertion loss of 1 dB at 10.2 GHz. The simulated and measured results for the filter with TZ located at 8.4 GHz are shown in Figure B.5. Again, a very good agreement can be observed.

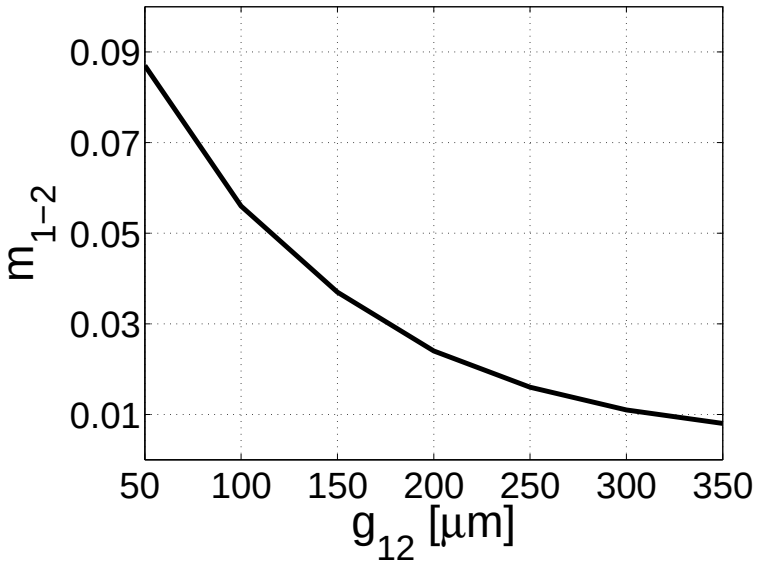

Figure B.4: Coupling strength m_{1-2} Vs gap g_{1-2}. $w_2 = 250$ μm ; $a = 2750$ μm.

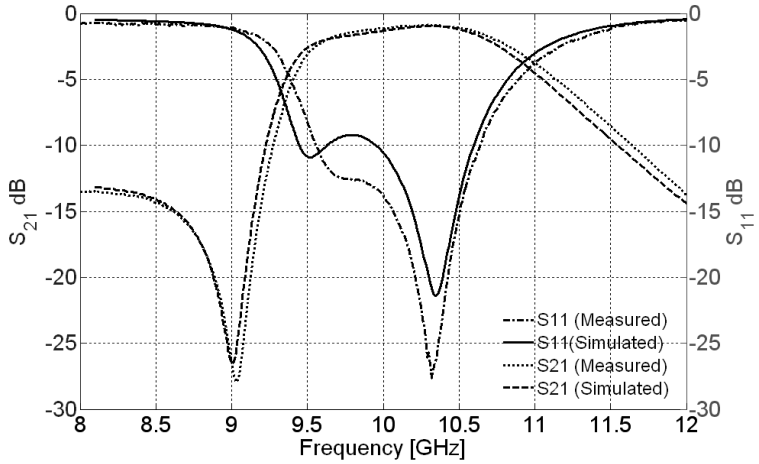

Figure B.5: Simulated and measured scattering parameters for filter with TZ at 9 GHz.

The two asymmetric filters, each with one TZ, developed before are cascaded to realize a fourth order filter with two TZs. The coupling scheme used to implement this filter is shown in Figure B.7. In this scheme, the nodes X and Y are NRNs (as are the source and load nodes) and an inverter is used as a link between the two individual building blocks. It is the presence of these NRNs that makes the filter modular. The susceptances of the NRNs and the coupling between them can be adjusted in the final implementation of the higher order filter. Many solutions are possible. In this case, we used the simplest

Table B.1: Physical parameters of the designed second order filters with reference to Figure B.2.

Parameter μ**m**	**Filter I** $\mathbf{f_z = 9}$ **GHz**	**Filter II** $\mathbf{f_z = 8.4}$ **GHz**
$\mathbf{a}$	2750	2750
$\mathbf{b}$	6100	6100
$\mathbf{w_1}$	100	100
$\mathbf{w_2}$	250	250
$\mathbf{w_3}$	490	490
$\mathbf{g_{1-2}}$	100	75
$\mathbf{g_{L-1}}$	100	275
$\mathbf{g_{L-2}}$	100	75
$\mathbf{L_{F1}}$	2975	2750
$\mathbf{L_{F2}}$	4075	4075
$\mathbf{L_t}$	880	880

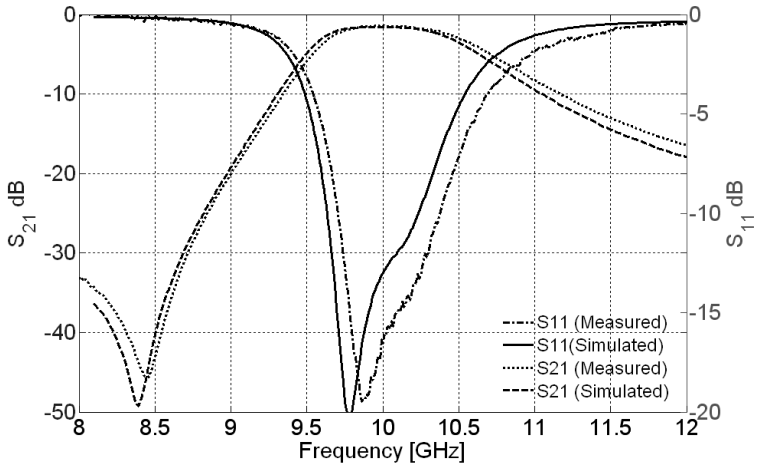

Figure B.6: Simulated and measured scattering parameters for filter with TZ at 8.4 GHz.

solution, wherein the NRN susceptances are made zero and a unit inverter is used as a link. This unit inverter can be easily implemented as a quarter wave transformer in microstrip form. The filter is modular because each filtering section controls the location of the TZ independently and, hence, is less sensitive to manufacturing tolerances. The generation of both TZs is preserved, although resonators in different building blocks are not directly coupled. The reduced sensitivity of the filter performance can be illustrated using the method outlined in [11]. It must be mentioned here that a four-pole two-zero asymmetric filter can be directly computed using the synthesis techniques outlined in Section 3.3.2

without the use of source-load multi-resonator couplings. However, such a filter will require diagonal coupling between two resonating nodes and can be hard to realize in microstrip form. Furthermore, it may be too sensitive to coupling coefficient variations. The sensitivity is especially more pronounced in asymmetric filters.

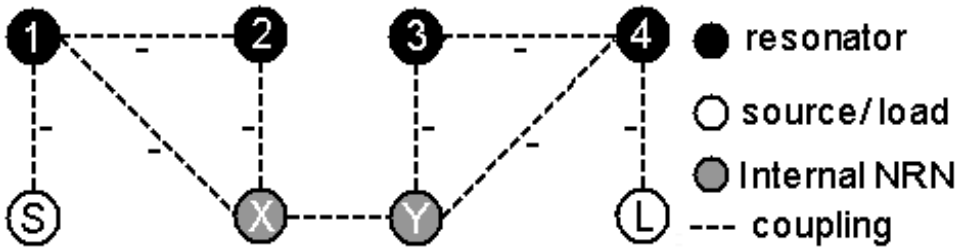

Figure B.7: Coupling scheme for the modular fourth order filter.

The layout of the developed fourth order filter is shown in Figure B.8. The measured and simulated results are shown in Figure B.9. The measured insertion loss is less than 3 dB at 10.4 GHz. An attenuation of as high as 50 dB has been achieved at 9 GHz, very close to the pass band of the filter.

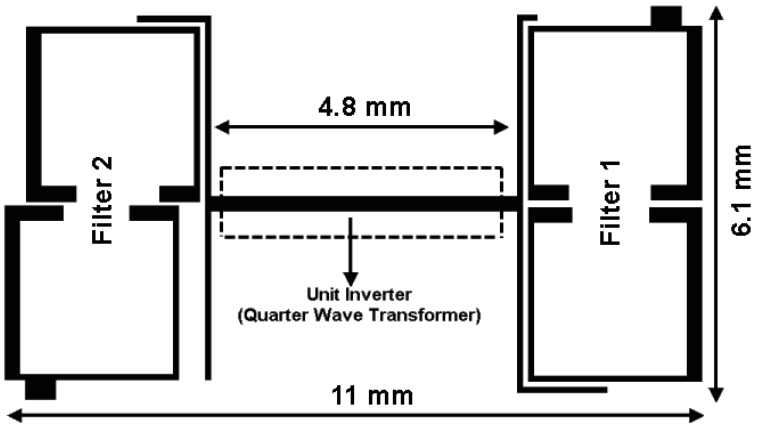

Figure B.8: Layout of the designed modular filter.

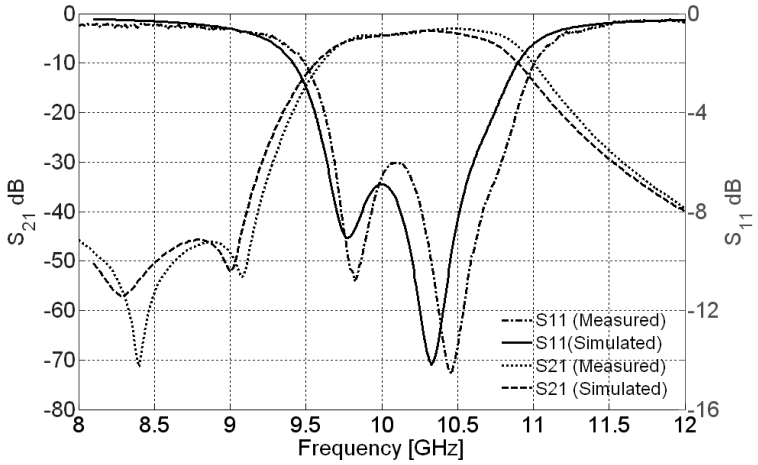

Figure B.9: Simulated and measured results for the modular filter with TZs at 9 GHz and 8.4 GHz.

REFERENCES

[1] Rogers Corporation advanced circuit materials website. [Online]. Date accessed: Dec. 2003. Available: http://www.rogerscorporation.com/acm/index.htm.

[2] Taconic microwave materials website. Various materials data sheets. [Online]. Date accessed: Jul. 2005. Available: http://www.taconic-add.com/.

[3] PMTEC LCP Materials Symp., Huntsville, AL, Oct. 29, 2002.

[4] C. Murphy, Rogers Corporation, private communication. Jan. 2004.

[5] *EM*-Picasso, Electromagnetic Design and Simulation Tool, http://www.emagware.com/empicasso.html.

[6] IE3D, Electromagnetic Design and Full-wave Simulation Tool, http://www.zeland.com.

[7] ADS-Momentum, Electromagnetic Design and Simulation Tool, http://eesof.tm.agilent.com/products/momentum-main.html.

[8] Ansoft-Designer, Electromagnetic Design and Simulation Tool, http://www.ansoft.com/ansoftdesigner.

[9] Amari, S., "Synthesis of cross-coupled resonator filters using an analytical gradient-based optimization technique," *IEEE Trans. Microwave Theory Tech.*, vol. 48, pp. 1559–1564, Sep 2000.

[10] Amari, S. and Rosenberg, U., "The doublet: A new building block for the modular design of elliptic filters," in *Eur. Microwave Conf.*, vol. 2, (Milan, Italy), pp. 123–125, 2002.

[11] Amari, S. and Rosenberg, U., "On the sensitivity of coupled resonator filters without some direct couplings," *IEEE Trans. Microwave Theory Tech.*, vol. 51, pp. 1767–1773, Jun 2003.

[12] Amari, S. and Rosenberg, U., "New building blocks for modular design of elliptic and self-equalized filters," *IEEE Trans. Microwave Theory Tech.*, vol. 52, pp. 721–736, Aug 2004.

[13] Amari, S., Rosenberg, U., and Bornemann, J., "Adaptive synthesis and design of resonator filters with source/load-multiresonator coupling," *IEEE Trans. Microwave Theory Tech.*, vol. 50, pp. 1969–1978, Aug 2002.

[14] Anagnostou, D. E., Bairavasubramanian, R., DeJean, G. E., Wang, G., Kingsley, N., Tentzeris, M. M., and Papapolymerou, J., "Development of a dual-frequency, dual-polarization, flexible and deployable antenna array for weather applications," in *15th IST Mobile and Wireless Communication Summit.*, (Myconos, Greece), Jun 2006.

[15] Anagnostou, D. E., Zheng, G., Chryssomallis, M. T., Lyke, J. C., Ponchak, G. E., Papapolymerou, J., and Christodoulou, C. G., "Design, fabrication, and measurements of an RF-MEMS-based self-similar reconfigurable antenna," *IEEE Trans. Antennas Propagat.*, vol. 54, pp. 422–432, Feb 2006.

[16] Bairavasubramanian, R., Kingsley, N., DeJean, G. E., Wang, G., Anagnostou, D. E., Tentzeris, M. M., and Papapolymerou, J., "Recent developments on lightweight, flexible, dual polarization/frequency phased arrays using RF MEMS switches on LCP multilayer substrates for remote sensing of precipitation," in *6th Earth Science and Technology Conference*, (Adelphi, MD), Jun 2006.

[17] Bairavasubramanian, R. and Papapolymerou, J., "Fully canonical pseudo-elliptic bandpass filters on multilayer liquid crystal polymer technology." accepted for future publication in *IEEE Microwave Wireless Compon. Lett.*

[18] Bairavasubramanian, R. and Papapolymerou, J., "Modular asymmetric quasi-elliptic filters using non-resonating nodes (NRNs) on liquid crystal polymer technology." submitted for publication in *IEE Proc. on Microwave, Antennas, and Propagation*.

[19] Bairavasubramanian, R. and Papapolymerou, J., "Multilayer quasi-elliptic filters using dual mode resonators on liquid crystal polymer technology," in *IEEE MTT-S Int. Microwave Symp. Dig.*, Jun 2007.

[20] Bairavasubramanian, R., Pinel, S., Laskar, J., and Papapolymerou, J., "Compact 60-ghz bandpass filters and duplexers on liquid crystal polymer technology," *IEEE Microwave Wireless Compon. Lett.*, vol. 16, pp. 237–239, May 2006.

[21] Bairavasubramanian, R., Pinel, S., Papapolymerou, J., Laskar, J., Quendo, C., Rius, E., Manchec, A., and Person, C., "Dual-band filters for WLAN applications on liquid crystal polymer technology," in *IEEE MTT-S Int. Microwave Symp. Dig.*, Jun 2005.

[22] Bairavasubramanian, R., Thompson, D., DeJean, G., Ponchak, G. E., Tentzeris, M. M., and Papapolymerou, J., "Development of mm-wave dual-frequency multilayer antenna arrays on liquid crystal polymer (LCP) substrate," in *IEEE AP Symp.*, pp. 393–396, Jul 2005.

[23] Bavisi, A., *Integrated Multi-Mode Oscillators And Filters For Multi-Band Radios Using Liquid Crystalline Polymer Based Packaging Technology.* PhD thesis, Georgia Institute of Technology, 2006.

[24] Burghatz, J. N., Edelstein, D. C., Jenkins, K. A., and Kwark, Y. H., "Spiral inductors and transmission lines in silicon technology using copper damascene interconnects and low loss substrates," *IEEE Trans. Microwave Theory Tech.*, vol. 45, pp. 1961–1968, Oct 1997.

[25] Cameron, R. J., "Advanced coupling matrix synthesis techniques for microwave filters," *IEEE Trans. Microwave Theory Tech.*, vol. 51, pp. 1–10, Jan 2003.

[26] Cameron, R., "General coupling matrix synthesis methods for chebyshev filtering functions," *IEEE Trans. Microwave Theory Tech.*, vol. 47, pp. 433–442, Apr 1999.

[27] Carver, K. R. and Mink, J. W., "Microstrip antenna technology," *IEEE Trans. Antennas Propagat.*, vol. 29, pp. 2–24, Jan. 1981.

[28] Cetiner, B. A., Qian, J. Y., Chang, H. P., Bachman, M., Li, G. P., and Flaviis, F. D., "Monolithic integration of RF MEMS switches with a diversity antenna on PCB substrate," *IEEE Trans. Microwave Theory Tech.*, vol. 51, pp. 332–335, Jan 2003.

[29] Chang, H.-C., Yeh, C.-C., Ku, W.-C., and Tao, K.-C., "A multilayer bandpass filter integrated into RF module board," in *IEEE MTT-S Int. Microwave Symp. Dig.*, pp. 619–622, 1996.

[30] Chen, L., Crnic, M., Zonghe, L., and Liu, J., "Process development and adhesion behavior of electroless copper on liquid crystal polymer (LCP) for electronic packaging application," *IEEE Trans. Comp., Packag., Manufact. Technol. B*, vol. 25, pp. 273–278, Oct. 2002.

[31] Cho, C. and Gupta, K. C., "Design methodology for multilayer coupled line filters," in *IEEE MTT-S Int. Microwave Symp. Dig.*, pp. 785–788, 1997.

[32] Culbertson, E. C., "A new laminate material for high performance PCBs: Liquid crystal polymer copper clad films," in *IEEE Electronic Components and Technology Conf.*, pp. 520–523, May 1995.

[33] Curtis, J. A. and Fiedziuszko, S. J., "Miniature dual mode microstrip filters," in *IEEE MTT-S Int. Microwave Symp. Dig.*, pp. 443–462, Jun 1991.

[34] Davis, M. F., Yoon, S.-W., Pinel, S., Lim, K., and Laskar, J., "Surface mountable liquid crystal polymer package with vertical via transition compensating wire inductance up to v -band," in *IEEE MTT-S Int. Microwave Symp. Dig.*, vol. 2, pp. 1155–1158, June 2003.

[35] Degen, C. and Keusgen, W., "Performance evaluation of MIMO systems using dual-polarized antennas," in *10th Int. Conf. on Telecommunications*, pp. 1520–1525, Feb. 2003.

[36] DeJean, G., Bairavasubramanian, R., Thompson, D., Ponchak, G. E., Tentzeris, M. M., and Papapolymeou, J., "Liquid crystal polymer (LCP): a new organic material for the development of multilayer dual-frequency/dual-polarization flexible antenna arrays," *IEEE Antennas Wireless Propagat. Lett.*, vol. 4, pp. 22–26, 2005.

[37] Farrell, B. and Lawrence, M. S., "The processing of liquid crystalline polymer printed circuits," in *IEEE Electronic Components and Technology Conf.*, pp. 667–671, May 2002.

[38] Floyd, B. A., Reynolds, S. K., Pfeiffer, U. R., Zwick, T., Beukema, T., and Gaucher, B., "Sige bipolar transceiver circuits operating at 60 GHz," *IEEE J. Solid-State Circuits*, vol. 40, pp. 156–167, Jan. 2005.

[39] Garg, R., Bhartia, P., Bahl, I., and Ittipiboon, A., *Microstrip Antenna Design Handbook*. Norwood, MA: Artech House, 2000.

[40] Granholm, J. and Skou, N., "Dual-frequency, dual-polarization microstrip antenna array development for high-resolution, airborne SAR," in *IEEE Asia Pacific Microwave Symp.*, pp. 17–20, Dec. 2000.

[41] Gupta, K. C., Garg, R., Bahl, I., and Bhartia, P., *Microstrip Lines and Slotlines*. Norwood, MA: Artech House, 2 ed., 1996.

[42] Higgins-III, L. M., "Hermetic and optoelectronic packaging concepts using multilayer and active polymer systems," *Advancing Microelectronics*, vol. 30, pp. 6–13, July 2003.

[43] Hong, J. S., "Couplings of asynchronously tuned coupled microwave resonators," *IEE Proc. Microwaves, Antennas and Propagation*, pp. 347–348, Oct 2000.

[44] Hong, J. S. and Lancaster, M. J., "Canonical microstrip filter using square open-loop resonators," *Electronics Lett.*, vol. 31, pp. 2020–2022, Nov 1985.

[45] Hong, J. S. and Lancaster, M. J., "Back-to-back microstrip open-loop resonator filters with aperture couplings," in *IEEE MTT-S Int. Microwave Symp. Dig.*, pp. 1239–1242, 1999.

[46] Hong, J. S. and Lancaster, M. J., *Microstrip filters for RF/Microwave appliations*. New York, NY: Wiley Interscience, 2001.

[47] Hsieh, L.-H. and Chang, K., "Compact elliptic-function low-pass filters using microstrip stepped-impedance hairpin resonators," *IEEE Trans. Microwave Theory Tech.*, vol. 51, pp. 193–199, Jan 2003.

[48] Huang, J., "The finite ground plane effect on the microstrip antenna radiation patterns," *IEEE Trans. Antennas Propagat.*, vol. 31, pp. 649–653, July 1983.

[49] Hum, S. V., Chu, J. Z., Johnston, R. H., and Okoniewski, M., "Efficiency of a resistively loaded microstrip patch antenna," *IEEE Antennas Wireless Propagat. Lett.*, vol. 2, pp. 22–25, 2003.

[50] Hunt, B. and Devlin, L., "LTCC for rf modules." IEE Seminar on Packaging and Interconnects at Microwave and mm-Wave Frequencies, June 2000.

[51] Huynh, T., Lee, K. F., and Lee, R. Q., "Cross-polarisation characteristics of rectangular patch antennas," *Electronics Lett.*, vol. 24, pp. 463–464, Apr. 1998.

[52] James, J. R., Hall, P. S., and Wood, C., *Microstrip Antenna Theory and Design*. London, U.K.: Peter Peregrinus,, 1981.

[53] Javor, R., Wu, X., and Chang, K., "Beam steering of a microstrip flat reflectarray antenna," in *IEEE AP Symp.*, pp. 956–959, June 1994.

[54] Jayaraj, K., Noll, T. E., and Singh, D. R., "A low cost multichip packaging technology for monolithic microwave integrated circuits," *IEEE Trans. Antennas Propagat.*, vol. 43, pp. 992–997, Sept. 1995.

[55] Jung, C. W., Lee, M.-J., Lee, G. P., and Flaviis, F. D., "Reconfigurable scan-beam single-arm spiral antenna integrated with RF-MEMS switches," *IEEE Trans. Antennas Propagat.*, vol. 54, pp. 455–453, Feb 2006.

[56] Kamagowa, K., Tokumitsu, T., and Aikawa, M., "Multifrequency microstrip antennas using alumina- ceramic/polyimide multilayer dielectric substrate," *IEEE Trans. Microwave Theory Tech.*, vol. 44, pp. 2431–2437, Dec 1996.

[57] Khoo, C., Brox, B., Norrhede, R., and Maurer, F., "Effect of copper lamination on the rheological and copper adhesion properties of a thermotropic liquid crystalline polymer used in PCB applications," *IEEE Trans. Comp., Packag., Manufact. Technol. A*, vol. 20, pp. 219–226, July 1997.

[58] Kulke, R., Rittweger, M., Uhlig, P., and Gunner, C., "LTCC - multilayer ceramic for wireless and sensor applications." english translation from Produktion von Leiterplatten und Systemen (PLUS), IMST GmbH, Dec 2001.

[59] Kwok, R. S. and Liang, J.-F., "Characterization of high-Q resonators for microwave-filter applications," *IEEE Trans. Microwave Theory Tech.*, vol. 47, pp. 111–114, Jan 1999.

[60] Lee, R. Q., Lee, K. F., and Bobnchak, J., "Characteristics of a two layer electromagnetically coupled rectangular patch antenna," *Electron. Lett.*, vol. 23, pp. 1070–1072, 1987.

[61] Levine, E., Malamud, G., Shtrikman, S., and Treves, D., "A study of the microstrip array antennas with feed network," *IEEE Trans. Antennas Propagat.*, vol. 37, pp. 426–434, July 1989.

[62] Levy, R. and Matthaei, G., "Design of microwave filters," *IEEE Trans. Microwave Theory Tech.*, vol. 50, pp. 783–793, Mar. 2002.

[63] Li, R. and Kim, D. I., "A new compact low-pass filter with broad stopband and sharp skirt characteristics," in *IEEE Asia Pacific Microwave Symp.*, vol. 3, Dec. 2005.

[64] Li, R. L., DeJean, G., Papapolymerou, J., Laskar, J., and Tentzeris, M. M., "Radiation-pattern improvement of patch antennas on a large-size substrate using a compact soft surface structure and its realization on LTCC multilayer technology," *IEEE Trans. Antennas Propagat.*, vol. 53, pp. 200–208, Jan. 2005.

[65] Lim, K., Pinel, S., Davis, M., Sutono, A., Lee, C., Heo, D., Obatoynbo, A., Laskar, J., Tantzeris, M. M., and Tummala, R. R., "RF-System-on-Package (SOP) for wireless communications," *IEEE Microwave*, pp. 88–99, Mar. 2002.

[66] Mandal, M. K., Mondal, P., Sanyal, S., and Chakrabarty, A., "Low insertion-loss, sharp-rejection and compact microstrip low-pass filters," *IEEE Microwave Wireless Compon. Lett.*, vol. 16, pp. 600–602, Nov 2006.

[67] Martins, R. N. and Abdalla, H., "Design of low-pass microstrip filters with equal-ripple passband and finite attenuation poles," in *IEEE MTT-S Int. Microwave and Optoelectronics Conf. Dig.*, vol. 1, pp. 71–74, Aug. 2001.

[68] Matsuzawa, A., "RF-SoC - expectations and required conditions," *IEEE Trans. Microwave Theory Tech.*, vol. 50, pp. 245–253, Jan 2002.

[69] Matthaei, G., Young, L., and Jones, E. M. T., *Microwave filters, impedance-matching networks, and coupling structures*. Dedham, MA: Artech House, 1980.

[70] Mizoe, J., "Miniature 60 GHz transmitter/ receiver modules on AIN multi-layer high temperature co-fired ceramic," in *IEEE MTT-S Dig.*, pp. 475–478, 1999.

[71] Navarro, E. A., Luximon, A., Craddock, I. J., Paul, D. L., and Dean, M., "Multilayer and conformal antennas using synthetic dielectric substrates," *IEEE Trans. Antennas Propagat.*, vol. 51, pp. 905–908, Apr 2003.

[72] Nishikawa, K., Piernas, B., Nakagawa, T., Araki, K., and Cho, K., "V-band fully-integrated TX/RX single-chip 3-D MMICs using commercial GaAs pHEMT technology for high-speed wireless applications," in *IEEE GaAs IC Symp. Dig.*, pp. 97–100, 2003.

[73] Papapolymerou, I., Drayton, R. F., and Katehi, L. P. B., "Micromachined patch antennas," *IEEE Trans. Antennas Propagat.*, vol. 46, pp. 275–283, Feb. 1998.

[74] Peroulis, D., Sarabandi, K., and Katehi, L. P. B., "Design of reconfigurable slot antennas," *IEEE Trans. Antennas Propagat.*, vol. 53, pp. 645–654, Feb 2005.

[75] Person, C., Sheta, A., Coupez, J. P., and Toutain, S., "Design of high performance band-pass filters by utilizing multi-layer thick-film technology," in *Proc. 24th Eur. Microwave Conf.*, (Cannes, France), pp. 466–471, 1994.

[76] Pinel, S., Bairavasubramanian, R., Laskar, J., and Papapolymerou, J., "Compact planar and vialess composite low-pass filters using folded stepped-impedance resonator on liquid-crystal-polymer substrate," *IEEE Trans. Microwave Theory Tech.*, vol. 53, pp. 1707–1712, May 2005.

[77] Porter, B. G., Rauth, L. L., Mura, J. R., and Gearhart, S. S., "Dual-polarized slot-coupled patch antennas on duroid with teflon lenses for 76.5-GHz automotive radar systems," *IEEE Trans. Antennas Propagat.*, vol. 47, pp. 1836–1842, Dec. 1999.

[78] Pozar, D. M., "Microstrip antenna aperture-coupled to a microstripline," *Electronics Lett.*, vol. 21, pp. 49–50, Jan. 1985.

[79] Pozar, D. M., *Microwave Engineering.* New York, NY: John Wiley & Sons, 2003.

[80] Pozar, D. M. and Duffy, S. M., "A dual band circularly polarized aperture-coupled stacked microstrip antenna for global positioning satellite," *IEEE Trans. Antennas Propagat.*, vol. 45, Nov. 1997.

[81] Pozar, D. M. and Metzler, T. A., "Analysis of a reflectarray antenna using microstrip patches of variable size," *Electronics Lett.*, vol. 29, pp. 657–658, Apr. 1993.

[82] Quendo, C., Rius, E., and Person, C., "Narrow bandpass filters using dual behavior resonators," *IEEE Trans. Microwave Theory Tech.*, vol. 51, pp. 734–742, Mar. 2003.

[83] Rhodes, J. D. and Cameron, R. J., "General extracted pole synthesis technique with application to low-loss TE_{011} mode filters," *IEEE Trans. Microwave Theory Tech.*, vol. 28, pp. 1018–1028, Sep 1980.

[84] Rose, C. A. and Cook, J. H., "High-accuracy cross-polarization measurements using a single-reflector compact range," *IEEE Antennas Propagat. Mag.*, vol. 41, Apr 1999.

[85] Row, J., "A dual-frequency dual-polarization microstrip antenna fed by an inclined slot," *Microwave and Optical Technology Lett.*, vol. 41, pp. 426–434, June 2004.

[86] Schaubert, D. H. and Yngvesson, K. S., "Experimental study of a microstrip array on high permittivity substrate," *IEEE Trans. Antennas Propagat.*, vol. 34, pp. 92–97, Jan. 1986.

[87] Schwab, W., Boegelsack, F., and Menzel, W., "Multilayer suspended stripline and coplanar line filters," *IEEE Trans. Microwave Theory Tech.*, vol. 42, pp. 1403–1406, Jul 1994.

[88] Scrantom, C. Q. and Lawson, J. C., "LTCC technology where we are and where were going-II," in *Technologies for wireless applications, IEEE MTT-S Symp.*, pp. 193–200, Feb. 1999.

[89] Shafaiv, L. L., Chamma, W. A., Barakat, M., Strickland, P. C., and Seguin, G., "Dual-band dual-polarized perforated microstrip antennas for SAR applications," *IEEE Trans. Antennas Propagat.*, vol. 48, pp. 58–66, Jan. 2000.

[90] Sheen, J.-W., "A compact semi-lumped low-pass filter for harmonics and spurious suppression," *IEEE Microwave Wireless Compon. Lett.*, vol. 10, pp. 92–93, Mar 2000.

[91] Smulders, P., "Exploiting the 60 GHz band for local wireless multimedia access: Prospects and future directions," *IEEE Commun. Mag.*, vol. 40, pp. 140–147, Jan. 2002.

[92] Sze, J.-Y. and Wong, K.-L., "Dual-frequency slotted rectangular microstrip antenna," *IEEE Trans. Antennas Propagat.*, vol. 48, pp. 1149–1152, Aug 2000.

[93] Thompson, D., *Characterization and design of liquid crystal polymer (LCP) based multilayer RF components and packages.* PhD thesis, Georgia Institute of Technology, 2006.

[94] Thompson, D. C., Papapolymerou, J., and Tentzeris, M. M., "High temperature dielectric stability of liquid crystal polymer at mm-wave frequencies," *IEEE Microwave Wireless Compon. Lett.*, vol. 15, pp. 561–563, Sept. 2005.

[95] Thompson, D. C., Tantot, O., Jallageas, H., Ponchak, G. E., Tentzeris, M. M., and Papapolymerou, J., "Characterization of liquid crystal polymer (LCP) material and transmission lines on LCP substrates from 30-110 GHz," *IEEE Trans. Microwave Theory Tech.*, vol. 52, pp. 1343–1352, Apr. 2004.

[96] Tsai, C.-M., Lee, H.-M., and Tsai, C.-C., "Planar filter design with fully controllable second passband," *IEEE Trans. Microwave Theory Tech.*, vol. 53, pp. 3429–3439, Nov 2005.

[97] Tsai, L.-C. and Hsue, C.-W., "Dual-band bandpass filters using equal-length coupled serial-shunted lines and Z-transform technique," *IEEE Trans. Microwave Theory Tech.*, vol. 52, pp. 1111–1117, Apr 2004.

[98] Tummala, R. R., "SOP: What is it and why? A new microsystem-integration technology paradigm - Moores law for system integration of miniaturized convergent systems of the next decade," *IEEE Trans. Adv. Packag.*, vol. 27, pp. 241–249, May 2004.

[99] Tummala, R. R. and Laskar, J., "Gigabit wireless: System-on-a-Package technology," *Proc. IEEE*, vol. 92, pp. 376–387, Feb. 2004.

[100] Wheeler, H. A., "The radiansphere around a small antenna," *Proc. IRE*, pp. 1325–1331, Aug 1959.

[101] Wolff, I., "Microstrip bandpass filter using degenerate modes of a microstrip ring resonator," *Electron. Lett.*, vol. 8, pp. 302–303, Jun 1972.

[102] Wong, J. S., "Microstrip tapped-line filter design," *IEEE Trans. Microwave Theory Tech.*, vol. 27, pp. 44–50, Jan 1979.

[103] Wong, K.-L. and Sze, J.-Y., "Dual-frequency slotted rectangular microstrip antenna," *Electron. Lett.*, vol. 34, pp. 1368–1370, Jul 1998.

[104] Wu, R. and Amari, S., "New triangular microstrip loop resonators for bandpass dual-mode filter applications," in *IEEE MTT-S Int. Microwave Symp. Dig.*, pp. 941–944, Jun 2005.

[105] Yao, S. J., Bonetti, R. R., and Williams, A. E., "Generalized dual-plane multicoupled line filters," *IEEE Trans. Microwave Theory Tech.*, vol. 41, pp. 2182–2189, Dec 1993.

[106] Zheng, G., Papapolymerou, J., and Tentzeris, M. M., "Wideband coplanar waveguide RF probe pad to microstrip transitions without via holes," *IEEE Microwave Wireless Compon. Lett.*, vol. 13, pp. 544–546, Dec. 2003.

[107] Zhu, L., Fu, R., and Wu, K.-L., "A novel broadband microstrip-fed wide slot antenna with double rejection zeros," *IEEE Antennas Wireless Propagat. Lett.*, vol. 2, pp. 194–196, 2003.

[108] Zhu, L., Wecowski, P., , and Wu, K., "New planar dual-mode filter using cross-slotted patch resonator for simultaneous size and loss reduction," *IEEE Trans. Microwave Theory Tech.*, vol. 47, pp. 650–654, May 1999.

[109] Z.Wei and Pham, A., "Liquid crystal polymer (LCP) for microwave/millimeter wave multi-layer packaging," in *IEEE MTT-S Int. Microwave Symp. Dig.*, pp. 2273–2276, June 2003.